CMR EFFECT AND RELATED PROPERTIES OF Mo-BASED OXIDES WITH DOUBLE-PEROVSKITE STRUCTURE

YUAN CAILEI

(*M. Sc, ISSP*)

A THESIS SUBMITTED

FOR THE DEGREE OF DOCTOR OF PHILOSOPHY

DEPARTMENT OF PHYSICS

NATIONAL UNIVERSITY OF SINGAPORE

2003

DEDICATIONS:

To mentors for their guidance

To family for their love

Acknowledgements

A journey is easier when you travel together. Interdependence is certainly more valuable than independence. This thesis is the result of three years of work whereby I have been accompanied and supported by many people. It is a pleasant journey that I have now the opportunity to express my gratitude to all of them.

First of all, I would like to extend my wholehearted thanks to my supervisor Prof. Ong Phee Poh. He is a great supervisor as well as a respected mentor. He creates ladders of hope and mobility that a toddler like me can ascend, rising as far as abilities permit. He taught me to overcome fresh obstacles, be definite in aims, unshaken by failure, utterly honest with people, and almost every aspect of life and research that educated me not only to be a knowledgeable scholar but to be an intellectual of great personality as well. I will always remember the happy time we worked and enjoyed together.

I am also deeply indebted to my mentor Dr. Zhu Yong who's consistent and patient assistance, stimulating suggestions and encouragement helped me throughout the time of my study and research in NUS.

Many, many people have helped me out when I came across difficulties during the development of this thesis. I would like to give special thanks to Prof. Ong Chong Kim, Dr. Li Jie and Dr. Huang Qiang at the Center for Superconducting and Magnetic Materials (CSMM) for their assistance in magnetic transport measurements. My sincere thanks are due to Associate Professor Shen Zexiang and Dr. Yu Ting of the

Physics Department for their help in Raman spectra measurements. I also especially thank my friends Prof. Zeng Zhaoyang of Physics Department, Jiangxi Normal University and Mr. Yu Ting of Microelectronics Division, Nanyang Technological University for their useful discussions and helps in magnetic transport measurements. I thank all my colleagues at the department for their friendship and daily assistance.

This research has been supported and funded by National University of Singapore. Thanks for providing all the facilities and financial support that enable me to complete this thesis.

I also want to thank my parents, who taught me the value of hard work by their own example. I would like to share this moment of happiness with them. They rendered me enormous support during the whole tenure of my research. Without them, I will be nothing.

Lastly, I am grateful to my wife for the inspiration and moral support she provided throughout my research work and her patience was tested to the utmost by a long period of separation. Without her loving support and understanding I would never have completed my present work.

Finally, I would like to thank all whose direct and indirect support helped me complete my thesis in time.

PUBLICATIONS BASED ON THE PH.D RESEARCH

1. Temperature Dependence of Resistivity of $Sr_2CoMoO_{6-\delta}$ Films
   C. L. Yuan, Z. Y. Zeng, Y. Zhu, P. P. Ong, Z. X. Shen, C. K. Ong
   Phys. Rev. B (Submitted)

2. Influence of preparation method on $SrMoO_4$ impurity content and magnetotransport properties of double perovskite Sr_2FeMoO_6 polycrystals
   C. L. Yuan, Y. Zhu, P. P. Ong, Z. X. Shen, C. K. Ong
   Solid. State. Commu. **129**, 551 (2004)

3. Grain boundary effects on the magneto-transport properties of Sr_2FeMoO_6 induced by variation of the ambient H_2-Ar mixture ratio during annealing
   C. L. Yuan, Y. Zhu, P. P. Ong, C. K. Ong, T. Yu, Z. X. Shen
   Physica B: Condensed Matter **334**, 408 (2003)

4. Enhancement of room-temperature magnetoresistance in Sr_2FeMoO_6 by reducing its grain size and adjusting its tunnel-barrier thickness
   C. L. Yuan, Y. Zhu, P. P. Ong
   Appl. Phys. Lett. **82**, 934 (2003)

5. Effect of Cu doping on the magnetoresistive behavior of double perovskite Sr_2FeMoO_6 polycrystals
   C. L. Yuan, Y. Zhu, P. P. Ong
   J. Appl. Phys. **91**, 4421 (2002)

6. The effects of Cu doping on the magnetoresistive behavior of perovskites $La_{0.7}Ca_{0.3}MnO_y$
   C. L. Yuan, Y. Zhu, P. P. Ong
   Solid. State. Commu. **120**, 495 (2001)

7. Enhancement of photoluminescence in Ge nanoparticles by neighboring amorphous C in composite Ge/C thin films
   Y. Zhu, **C. L. Yuan**, P. P. Ong
   J. Appl. Phys. **93**, 6029 (2003)

8. Suppression of uv photoluminescence in sandwich-structured Si/C composite films
   Y. Zhu, **C. L. Yuan**, R. Liu, P. P. Ong
   Europhys. Lett. **60**, 323 (2002)

9. Room-temperature visible photoluminescence from undoped ZnS nanoparticles embedded in SiO_2 matrices
   Y. Zhu, **<u>C. L. Yuan</u>**, P. P. Ong
   J. Appl. Phys. **92**, 6828 (2002)

10. Co-existing photoluminescence of Si and Ge nanocrystals in Ge/Si thin film without cross-interference
    Y. Zhu, **<u>C. L. Yuan</u>**, S. L. Quek, S. S. Chan, P. P. Ong, Q. T. Li
    J. Appl. Phys. **90**, 5318 (2001)

11. Formation of double-perovskite Sr_2FeMoO_6 nanoparticles by mechanical activation
    T. Yu, Z. X. Shen, W. S. Toh, **<u>C. L. Yuan</u>**, P. P. Ong, J. Wang
    ICMAT 2003

LIST OF FIGURES

Chapter 1

Chapter 2

Chapter 3

Chapter 4

Chapter 5

Chapter 6

LIST OF TABLES

Summary

Magnetoresistive manganese perovskites have proven to be useful for the development of field-sensitive magnetic sensors operable at room temperature. In fact, some devices based on screen-printed oxides of polycrystalline materials have been built showing that there are some possible niches for applications. However, the fast decay of the low-field magnetoresistance (LFMR) with temperature and the fact that the Curie temperature remains critically low represent serious drawbacks for applications requiring operation temperatures up to 150–180 $^{\circ}$C.

In any event, half-metallic ferromagnets of higher Curie temperature are needed. Progress on crystallochemistry of double perovskites, such as Sr_2FeMoO_6, has been impressive and nowadays oxides of almost-ideal bulk properties can be prepared. However, detailed understanding of the LFMR in these oxides and the nature of grain boundaries remain elusive. Shaping of materials suitable for some applications is also starting, and in addition to tremendous progress in thin film preparation, thick films are already available. However, much effort on microstructural and structural analysis is required in order to understand and progress towards the control of the low-field magnetoresistance. Recent results on possible ways to further raise the Curie temperature in double perovskites are encouraging and there is room for new ideas and progress.

We have aimed to improve the present understanding on the intergrain tunneling magnetoresistance of the double perovskite materials in physics and technology, especially at a relatively low magnetic field and room temperature.

Firstly, Grain boundary modification studies of Sr_2FeMoO_6 polycrystals are presented. The relationship between the magnetoresistance and the $SrMoO_4$ impurities

are investigated, which improve the present understanding on the intergrain tunneling magnetoresistance of the double perovskite materials in physics and technology, especially at a relatively low magnetic field and room temperature. We studied the magnetic and electric properties of the Sr_2FeMoO_6 compound under different preparation conditions. Depending on preparation condition, we found a strong variation in nonmagnetic $SrMoO_4$ impurity, resulting in metallic or semiconducting behavior of resistivity of the sample. In particular, high-energy ball milling process suppresses the formation of the nonmagnetic $SrMoO_4$ impurity in the grain boundaries region. Also, the mixture ratio of the stream of gaseous H_2-Ar mixture strongly affects the eventual nonmagnetic $SrMoO_4$ impurity level in the annealed material. This $SrMoO_4$ impurity level, in turn, plays a crucial role in determining the low magnetic field intergrain tunneling magnetoresistance. The presence of the impurity leads to an enhancement of the intergrain tunneling barrier, with a consequential increase in the resistivity and the low-field magnetoresistance. This property opens up the possibility of implementing refined control of the magnetotransport properties of high-temperature half-metallic ferromagnetic materials. Our works also provide a simple method to prepare the single phase Sr_2FeMoO_6 polycrystals.

Secondly, temperature dependence of resistivity of $Sr_2CoMoO_{6-\delta}$ film was investigated. We investigated the temperature dependence of the resistivity and magnetoresistance of a polycrystalline $Sr_2CoMoO_{6-\delta}$ film deposited on (100)-$SrTiO_3$ substrate prepared by the pulsed laser deposition method. X-ray diffraction, Raman and magnetoresistance results demonstrate clearly the coexistence of a ferromagnetic metallic and an antiferromagnetic (or paramagnetic) insulating domain. Percolative transition between these two phases as the temperature varies, which is believed to induce a metal-insulator transition at around T_C, has been directly observed in our

measurements of the temperature dependence of the sample resistivity. Thus we have provided new direct evidence that a phase separation scenario also exists in the ordered double-perovskite structures materials.

Thirdly, the electrical, magnetic, and transport properties of Cu-doped polycrystalline samples $Sr_2Fe_{1-x}Cu_xMoO_6$ with ordered double perovskite structure are investigated. The electrical, magnetic, and transport properties of Cu-doped polycrystalline samples $Sr_2Fe_{1-x}Cu_xMoO_6$ with ordered double perovskite structure were investigated systematically. Analysis of the X-ray powder diffraction pattern based on the Rietveld analysis indicates that the substitution of Fe^{3+} ions by Cu^{2+} ions enhances the site location order of Fe, Cu and Mo on the B-site for the high-doping-level samples (x=0.20, 0.25, 0.30). With increasing doping level, a transition from semiconductor to metal behavior was also found to occur. Furthermore, the transition temperature was found to decrease either by the application of a magnetic field or by increasing the doping level. It can be concluded that the existence of Cu^{2+} ions induces the occurrence of $Fe^{3+\delta}$ ions and the double exchange (DE) interaction in $Fe^{3+} - O - Mo - O - Fe^{3+\delta}$. The transport mechanism in these samples can be attributed to the competition between the metal phase and the semiconductor phase arising from the doping of Cu^{2+} ions. Both the semiconductor-to-metal transition and the magnetoresistive behavior can be explained by the percolation threshold model.

Finally, for comparison with the works in Chapter five, we focus on a subject: the effects of Cu doping on the magnetoresistive behavior of perovskites $La_{0.7}Ca_{0.3}MnO_{y}$. The electronic and magnetic properties of Cu-doped perovskite $La_{0.7}Ca_{0.3}Mn_{1-x}Cu_xO_y$ obtained by doping Cu on its Mn sites were studied. The perovskite structure was found to remain intact up to the highest doping level of x=0.20. At low Cu concentration (x=0.05) the temperature-dependence of resistivity of the material

exhibited up to two peaks corresponding to the magnetic transitions from the PM to the

FM phase, and from the FM to the AFM phase. In general, the doping level was found

to suppress the ferromagnetic ordering of the material, increase its resistivity, and

produce large values of MR (magnetoresistance) near the resistivity peak. These results

were explained as due to the formation of the AF (antiferromagnetic) phase.

Table of Contents

Chapter 1

Introduction

In this chapter, we review the development of manganese perovskites and double perovskites. Firstly, we start with a general description of various magnetoresistance (MR) phenomena, and then we give an overview of the double perovskite family.

1.1. Magnetoresistance

Magnetoresistance occurs in all metals, where the resistance of the material changes with applied magnetic field. Classically, the MR effect depends on both the strength of the magnetic field and relative direction of the magnetic field with respect to the current.

Magnetic related applications have played an essential role in many aspects of modern technologies [1]. These applications range from the generation of electrical power to the processing of information. Previously, research focused mainly on the magnetic properties, especially their static or dynamic response to an external magnetic field. With the advent of the information era, more attention has been paid to the magnetic coupling effect such as MR effect because of its importance in information storage and retrieval. Based on the MR effect, the prototypes and even products of various kinds of sensors, actuators and data-storage devices have been fabricated. Today, the MR effect has demonstrated an amazing capability and a great potential for the next generation of electronic devices [2-5].

Thus far, several different kinds of MR effect have been found, such as Ordinary

MR (OMR), Anisotropic MR (AMR), Giant MR (GMR) and Colossal MR (CMR). The materials and mechanisms for these four types of magnetoresistance are distinctly different, which are also illustrated in Fig. 1.1, Fig. 1.2, Fig.1.3 and Fig.1.4, respectively.

1.2. Ordinary Magnetoresistance

The ordinary MR (OMR) exists for all metals, which was argued by E. H. Hall in 1879 [6]. OMR originates from the fact that the external field exerts a Lorentz force on the conducting electrons, forces the electron to rotate along a circle, resulting in an increase in the resistance of the material, that is, a positive MR.

OMR value can be defined as

$$MR = \frac{\rho_H - \rho_0}{\rho_0}$$

Where ρ_0 and ρ_H represent the resistivity under zero-field and H, respectively. OMR is roughly proportional to the square of the magnetic inductance B, OMR$\sim$B^2. When B=300 KOe, the OMR of Cu is about 40% [6]. Therefore, OMR of Cu at 1 KOe is estimated to be about 4×10^{-4}% [6]. This value is too small to be of significance. OMR is anisotropic in the sense that the field must be perpendicular to the current direction to observe the effect.
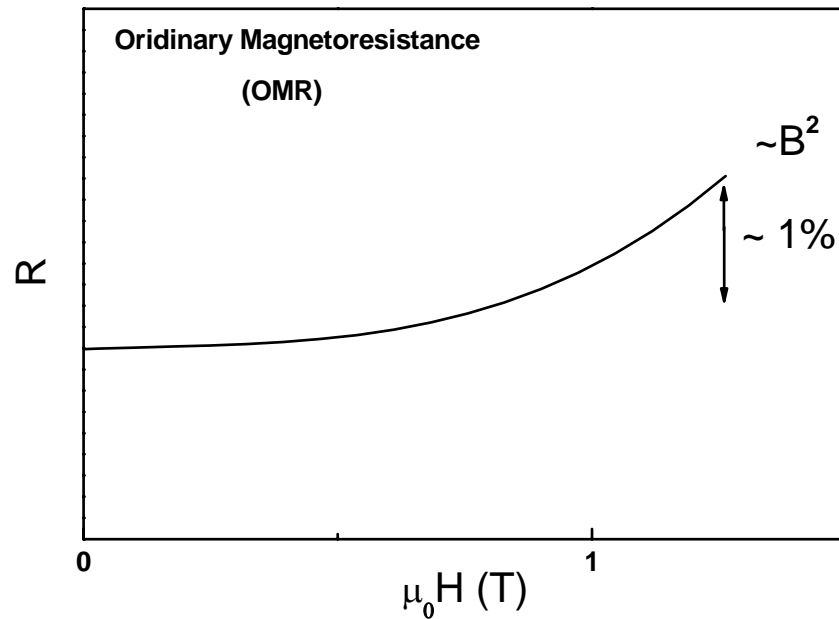
Fig.1.1. Ordinary magnetoresistance (OMR) (J. M. D. Coey, [7])

1.3. Anisotropic Magnetoresistance

AMR was firstly discovered in ferromagnetic polycrystalline metals in 1857 [6]. AMR can be an intrinsic property related to the orbital moment of the atomic charge distribution or an extrinsic property related to grain boundaries (GB) [8]. It changes sign with the relative orientation of the current (I) and the magnetization (M). The value of AMR value is normally defined as

$$MR = \frac{2(\rho_{//} - \rho_{\perp})}{\rho_{//} + \rho_{\perp}}$$

where $\rho_{//}$ and $\rho_{\perp}$ correspond to the situation that $M // I$ and $M \perp I$, respectively. For most materials, $\rho_{//} > \rho_{\perp}$ is satisfied. This is distinctively different from the fact $\rho_{//} < \rho_{\perp}$ for the OMR effect. The magnitude of AMR is usually in the order of 1%, however, the magnetization in thin films may be easily switched to produce the

resistance change, and thus AMR thin films have been successfully utilized in the

magnetic read head.
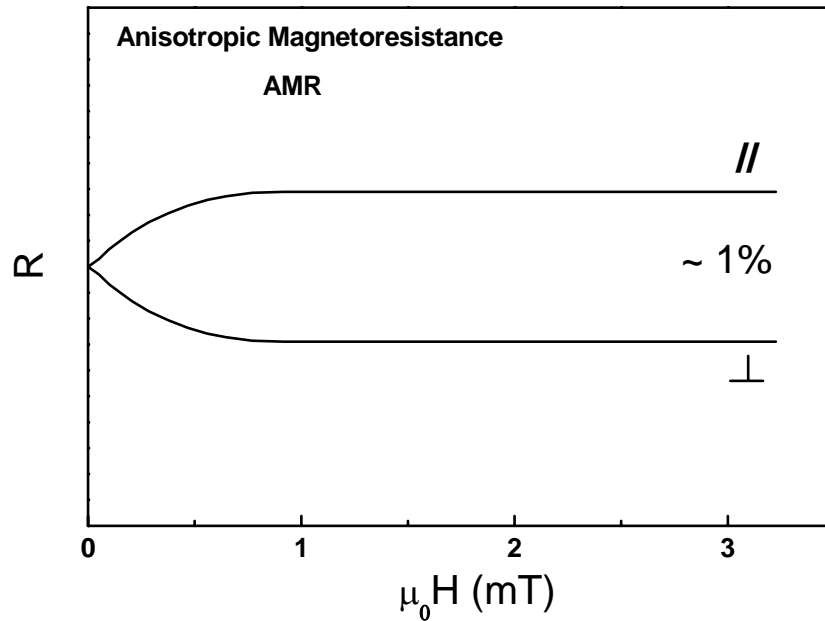
Fig.1.2. Anisotropic magnetoresistance (AMR) (J. M. D. Coey, [7])

1.4. Giant Magnetoresistance

Giant Magnetoresistance (GMR) is an extrinsic property related to the thin-film

multilayers of magnetic and normal metals. GMR was discovered in 1988 by Baibich

et al., in antiferromagnetically coupled multilayers of Fe/Cr, which is much larger than

the normal AMR [6, 7]. In this structure, thin layers of ferromagnetic (FM) layers are

separated by layers of nonmagnetic metals. The magnetic layers are coupled through

the non-magnetic layers in either a ferromagnetic or an antiferromagnetic

configuration depending on the thickness of the non-magnetic layers. The effect is

conventionally explained in terms of spin dependent scattering. Here the spin diffusion

length in the normal metal must be at least compatible to the spacing of the FM regions

[7]. By adjusting the thickness of the nonmagnetic metal layer, the FM layers can be set antiferromagnetically coupled in zero-field. A small switching field can modify the relative orientation of the FM layers to parallel, thus decreasing the scattering resistance [9]. Different from AMR, GMR is independent of the direction of the magnetic field, but the effect is greater in the current-perpendicular-to-plane (CPP) mode.

GMR value can be defined as [6]

$$GMR = \frac{\rho_{AF} - \rho_F}{\rho_F}$$

where ρ_{AF} and ρ_F denote the resistivity as the configuration of FM layers in the antiparallel and parallel directions, respectively. It has been found that the GMR value for the Co/Cu multilayer can be as high as 60-80% at room temperature [9]. This represents a milestone in magnetic recording technology.
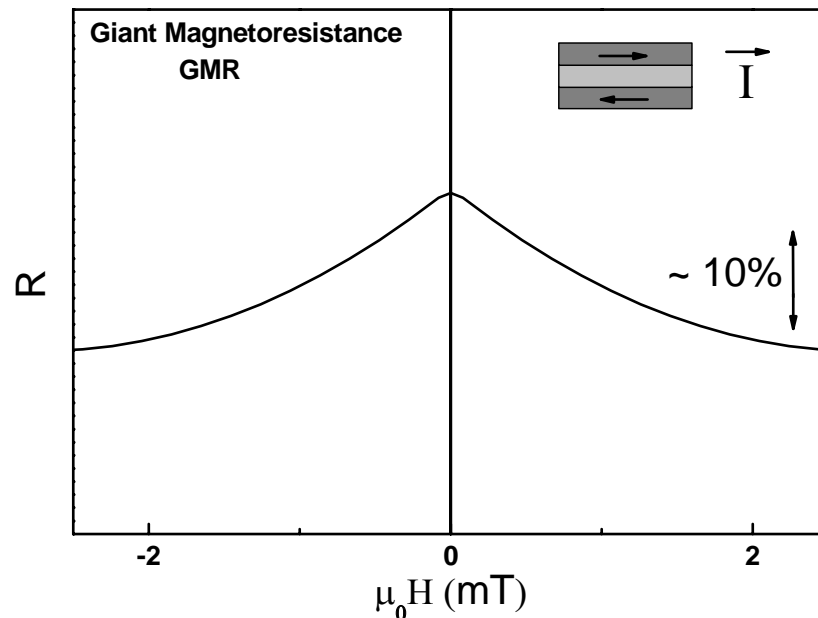
Fig.1.3. Giant magnetoresistance (GMR) (J. M. D. Coey, [7])

1.5. Colossal Magnetoresistance (CMR)

In recent years, it has become recognized that some materials, specifically 3d transition-metal oxides, possess large magnetoresistance, which was called colossal "magnetoresistance" (CMR) [10], mainly to distinguish it as a phenomenon distinct from GMR.
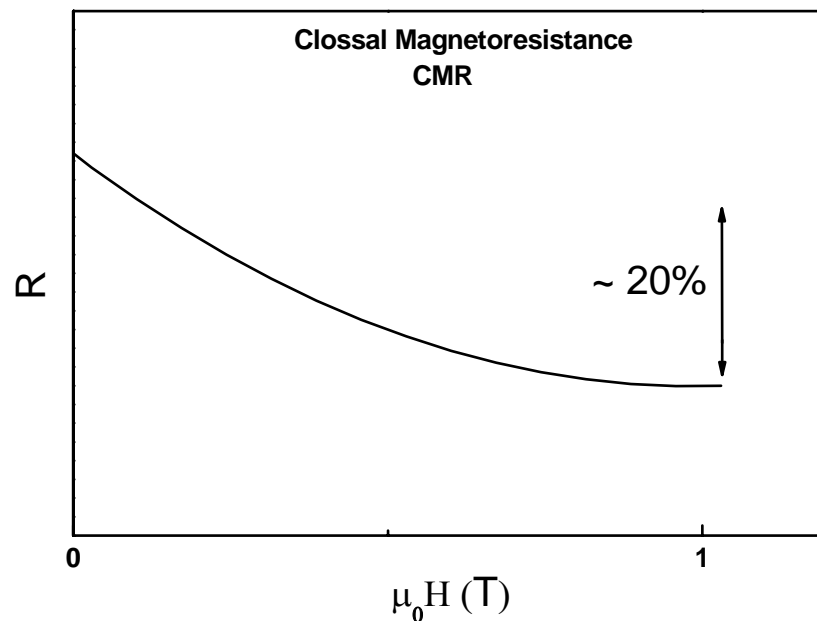
Fig.1.4. Colossal magnetoresistance (CMR) (J. M. D. Coey, [7])

The intrinsic CMR was discovered in 1994 in ferromagnetic oxides (typically $La_{2/3}Ca_{1/3}MnO_3$) by Jin *et al* [10, 11]. Later, a similar effect was found in other perovskite maganites in the form of $Re_{1-x}A_xMnO_3$ (Re stands for a rare earth ion such as La, Nd, Pr or Gd and A denotes a divalent ion such as Ca, Sr or Ba) and two other compound families: the pyrochlores, e.g. $Tl_2Mn_2O_7$ [12], and the spinels ACr_2Ch_4, where A (which denotes Fe, Cu, Cd for example) is a tetrahedrally coordinated cation and Ch is a chalcogen (S, Se, Te) [13]. Crystal structures of the most important oxides

discussed in this part are shown in Fig. 1.5.

(a) **(b)**

(c)
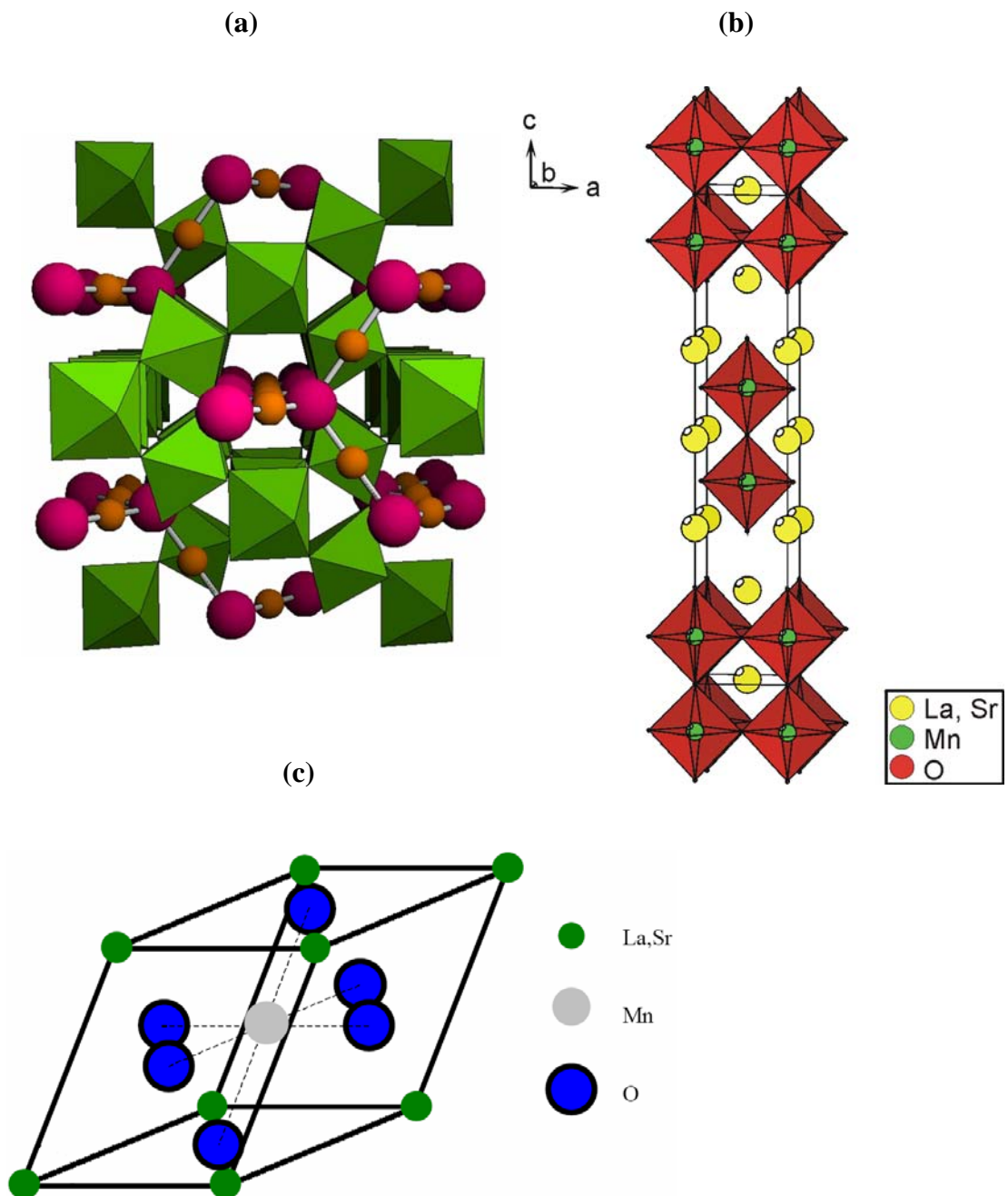
Fig.1.5. Crystal structures of the most important oxides discussed in this review: (a) pyrochlore structure ($Tl_2Mn_2O_7$) showing the tetrahedral manganese array. The Mn^{4+} ions are octahedrally coordinated by oxygen, and they form a corner-sharing tetrahedral array. (M. Venkatesan *et al.* [14]) (b) *n*=2 Ruddlesden-Popper phase ($La_{1.2}Sr_{1.8}Mn_2O_7$) (Y. Moritomo *et al.* [15]) (c) perovskite structure ($La_{0.7}Sr_{0.3}MnO_3$) (J. M. D. Coey [10]).

Depending on doping, these compounds show a complex magnetic phase diagram. These materials undergo a metal-insulator transition accompanied by the transition from paramagnetism (PM) to FM at the Curie temperature T_C, which is modeled as Double Exchange (DE) Interaction [16-18] between heterovalent (Mn^{3+}, Mn^{4+}) neighbors). The double exchange (DE) picture was first proposed by Zener [16] to explain the concurrent occurrence of the electrical and magnetic phase transitions. CMR can be qualitatively understood within the double-exchange model. An applied magnetic field leads to a better alignment of the core spins and, therefore, to a decrease in resistivity. This effect is strongest near the Curie temperature, where both spin disorder and the susceptibility are large. Accordingly, a maximum in the magnetoresistance appears near T_C. This argument applies to spin-disorder scattering in ferromagnets in general and does not explain the extraordinary magnitude of the magnetoresistance in the manganites. Today the DE picture still represents a fundamental understanding to explain the CMR effect. However, more recent research also revealed that a strong interplay among the spin, charge and lattice systems exists in CMR materials and the interplay is of significant relevance to the CMR effect. Therefore, it is now generally accepted that the real mechanism for CMR is much more complicated than the simplest DE scheme.
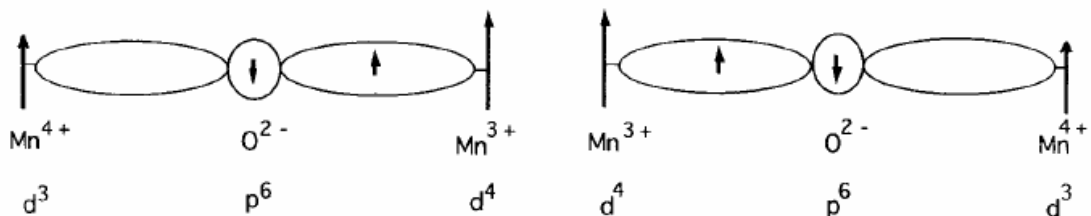
Fig.1.6. Schematic diagram of the double-exchange mechanism (C. Zener, [16]). The two states Mn^{3+}-Mn^{4+} and Mn^{4+}-Mn^{3+} are degenerate if the manganese spins are parallel.

The prototypical CMR compound is derived from the parent compound, perovskite $LaMnO_3$ [19]. Most of the recent work has focused on Ca and Sr substituted compounds ($La_{1-x}Sr_xMnO_3$ [20-23] and $La_{1-x}Ca_xMnO_3$ [24-26]). There are some differences in the phase diagrams for the two cases, owing mainly to the size difference between Ca and Sr ions. Less work has been done on Ba-substituted phases. Some research work about thin films of $La_{0.67}Ba_{0.33}MnO_3$ [27] and $La_{(2-x)/3}Ba_{(1+x)/3}Mn_{1-x}Cu_xO_3$ [28] were studied by von Helmolt *et al.* The layered perovskite structure ($La_{1-x}Sr_{1+x}MnO_4$ [29, 30], $La_{2-2x}Sr_{1+2x}Mn_2O_7$ [15] and $La_{2-2x}Ca_{1+2x}Mn_2O_7$ [31]), which is one in a Ruddlesden–Popper series $(Re_{1-x}A_x)_{n+1}Mn_nO_{3n+1}$ of layered compounds has also been studied, systematically. All the large resistance and the associated MR are now thought to be related to the formation of small lattice polarons in the paramagnetic state. Typical resistivity versus temperature curves for $La_{0.7}(Ca_{1-y}Sr_y)_{0.3}MnO_3$ single crystals is shown in Fig. 1.7 [32]. The magnetoresistance is maximal near the metal-insulator transition leading to a peak in the magnetoresistance ratio:

$$MR = [\Delta\rho / \rho(0)] = [\rho(H) - \rho(0)] / \rho(0)$$

The height of this magnetoresistance peak is seen to decrease with increasing Curie temperature. This is a general trend in the manganites and magnetoresistance values of nearly 100% can be found in compounds with low Curie temperatures.

Recently, much attention has been also given to another type of collective state, charge order (CO), typically observed for $x > 0.3$ ($Re_{1-x}A_xMnO_3$). At these doping levels CO can compete with the FM ground state, leading to complex electronic phase behavior as their chemical formula is varied [33-35]. Perhaps the biggest intellectual advance in understanding these disparate effects is the realization of the importance of electron–phonon (e-ph) coupling. Several theories have elucidated the role of e-ph

coupling in producing CMR [36, 37]. It is also widely held that this e-ph coupling is necessary to explain not only CMR, but also (1) the polaron signatures in transport studies, (2) the large isotope effect on the FM Curie temperature [38], (3) the large Debye-Waller factors [39] and (4) the CO state and its large sound velocity anomalies [35]. The microscopic origin of strong e-ph coupling is the large Jahn-Teller effect which occurs for d^4 ions in an octahedral ligand environment [40]. For the undoped material ($x=0$, $Re_{1-x}A_xMnO_3$) this results in a large static structural distortion [41]. The question of how this e-ph coupling manifests itself in the CMR range ($\chi \approx 0.2$ - 0.4, ($Re_{1-x}A_xMnO_3$) is one of the central questions to be addressed by theory.
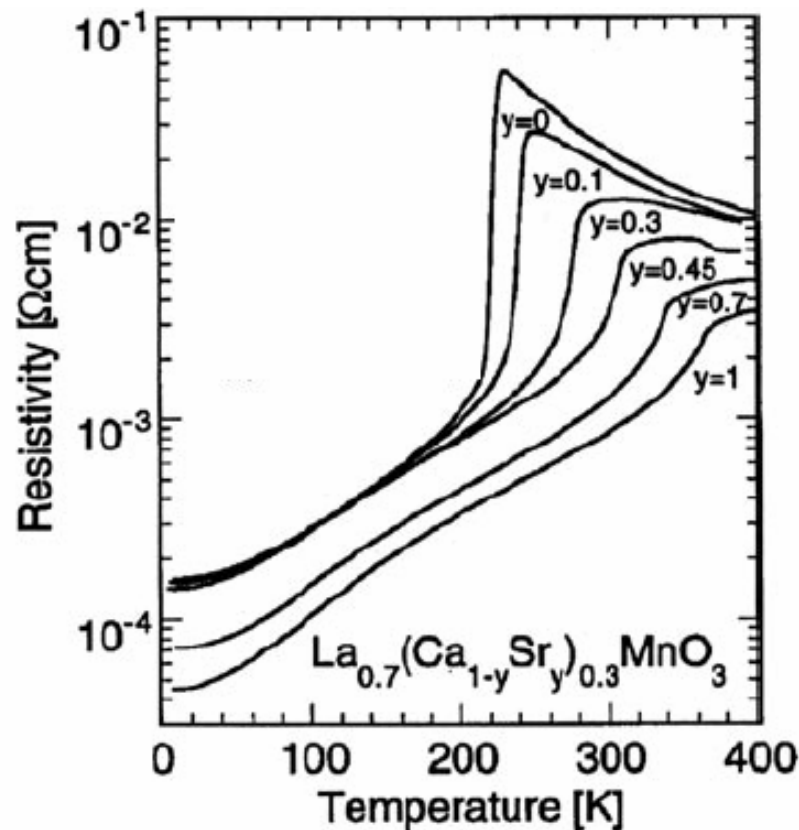
Fig.1.7. Typical resistivity versus temperature curves of $La_{0.7}(Ca_{1-y}Sr_y)_{0.3}MnO_3$ single crystals (Y. Tomioka *et al.* [32]). The anomaly at a temperature of 370 K for the $y = 0.45$ doping is due to a structural transition from a low-temperature orthorhombic to a high-temperature rhombohedra phase.

The understanding developed to explain CMR in the manganite perovskites does not carry over easily to two other CMR compound families-the pyrochlores, e.g. $Tl_2Mn_2O_7$ [12], and the spinels ACr_2Ch_4 where A (denoting Fe, Cu, Cd for example) is a tetrahedrally coordinated cation and Ch is a chalcogen (S, Se, Te) [13]. Like the manganese perovskites, these compounds exhibit large drops in resistivity at their FM T_C values. However, unlike the perovskites, they possess (1) no mixed valency (and as a result, have low carrier density), (2) an A-site cation (Tl or A) capable of contributing states at the Fermi level, and (3) large deviations of the metal-anion-metal bond angle from 180°.

Experimental and theoretical efforts have now established a strong coupling of electronic, magnetic and structural degrees of freedom as being responsible for the CMR properties in the manganites [42-49]. Subtle interplay of these interactions gives rise to a wide spectrum of interesting physical properties in terms of charge and orbital ordering in addition to CMR properties in doped manganites [50-52].

1.6. The limitation of CMR materials and the need for novel materials

While the study of such doped manganites has been most rewarding in terms of various fundamental issues, there are two main factors that undermine its widespread technological use. Technological exploitation of the CMR property of manganites is primarily limited by the requirements of low temperature and high-applied magnetic field for obtaining appreciable negative magnetoresistance effect in these compounds. Accordingly, many studies focused on the investigation of room temperature and low magnetic field magnetoresistance effects found in some magnetic oxides. To a large extent this research was driven by the rapid increase of data storage density in magnetic storage devices. Since read heads for hard disks employ magnetoresistive

read-out techniques, progressive miniaturization of sensors requires materials or heterostructures with increasing magnetoresistive effect. The development of hard disk storage media is currently very rapid with a doubling of storage density about every nine months. Therefore, the need for more efficient magnetoresistive sensors will persist in the future. It has to be clear that room-temperature performance is the most vital criterion in judging new magnetoresistive materials.

Since the CMR effect is most significant close to the magnetic ordering temperatures, there has been an intense search for compounds with magnetic ordering temperatures substantially higher than the *Tc* (~ 200-350 K) in manganites. Recently, it has been reported [53] that Sr_2FeMoO_6, an ordered double perovskite of the general formula $A_2B'B''O_6$ and containing no manganese, exhibits a pronounced negative CMR at lower magnetic fields and higher temperatures compared to the doped manganites. The reason for this improved MR property in this compound at a relatively higher temperature arises primarily from the fact that Sr_2FeMoO_6 has a surprisingly high magnetic ordering temperature (~420 K) [54, 55] compared to manganites, since the largest MR response is expected close to the magnetic T_C. There are also some fundamental aspects which distinguishes Sr_2FeMoO_6 from the group of perovskite manganites. The most important differences are: (1) the CMR property is present in the undoped parent compound, Sr_2FeMoO_6, unlike manganites, (2) electron-phonon coupling does not appear to be crucial for the observed properties of this compound, and finally (3) the conventional double exchange mechanism [16, 17], universally accepted in the case of doped manganites, is absent in Sr_2FeMoO_6. Thus, a *Tc* of about 420 K in Sr_2FeMoO_6, which is higher than even that in the manganites, suggests a novel origin of magnetism in this compound.

1.7. Double perovskite family

In this part, we review in depth the physical properties of the double perovskite materials and the present understanding. Sr_2FeMoO_6 belongs to the class of ordered double perovskites, having the general formula $A_2B'B''O_6$, where A is a divalent alkaline earth cation (Ca, Sr Ba), and B' and B'' are small metal ions located on octahedrally coordinated interstices of the closed-packed lattice having a simple cubic configuration [56, 57, 54, 58]. For the ordered double perovskites, a resembles rock-salt structure is observed. There is a rapidly increasing bulk of research work on double perovskites; recent research focused mainly on Sr_2FeMoO_6 with a Curie temperature of about 420 K [53]. Ca and Ba substitution was found to decrease the Curie temperature to 345 K (Ca_2FeMoO_6) and 367 K (Ba_2FeMoO_6) [59]. The highest Curie temperature was reported for Ca_2FeReO_6 with $T_C \sim 538$ K [56]. It is also to be noted that there are several other examples of both ferromagnetic and antiferromagnetic compounds within the $A_2B'B''O_6$, double perovskite oxide series; for example, Sr_2CrMoO_6 and Sr_2FeReO_6 are ferromagnetic, while Sr_2FeWO_6, Sr_2MnMoO_6 and Sr_2CoMoO_6 are anti-ferromagnetic [60-63]. Thus, an explanation of the magnetic structure of Sr_2FeMoO_6 must also be consistent with such diverse properties observed within the same double perovskite family.

1.7.1. Crystal structure and band structure calculation results

As shown in table 1, at room temperature and below the compound is cubic, tetragonal and monoclinic for Ba_2FeMoO_6, Sr_2FeMoO_6 and Ca_2FeMoO_6, respectively [59, 64-66]. Sr_2FeMoO_6 shows a crystallographic transition from cubic to tetragonal on cooling through the Curie temperature [65]. Band-structure calculations for Sr_2FeMoO_6 and Sr_2FeReO_6 using the full-potential augmented plane-wave (FLAPW)

method based on the generalized gradient approximation (GGA) yielded a half-metallic band structure [53, 61]. In the majority band an energy gap of about 1 eV was seen at the Fermi level between the occupied Fe e_g and the unoccupied Re or Mo t_{2g} levels. The minority density of states is finite at the Fermi level with carriers of hybridized Fe(3d) and Mo(4d) or Re(5d) character, respectively. It can be easily seen from the Fig.1.8 that there is a substantial gap in the spin-up DOS across the Fermi energy, E_F, while the spin-down channel shows finite and continuous DOS across the E_F, in agreement with the metallic state of the system. The most important consequence of this is that the mobile charge carriers in this system are fully spin-polarized.

		Ca_2FeMoO_6	Sr_2FeMoO_6	Ba_2FeMoO_6
Crystal structure		Monoclinic $P2_l/n$	Tetragonal P_4/mmm	cubic $Fm3m$
Lattice parameters	a(pm)	541.6	557.3	806.2
	b(pm)	552.7		
	c(pm)	769.8	790.5	

Table 1.1. Structure characteristics of A_2FeMoO_6 (A=Sr, Ca, Ba) [59, 64-66]
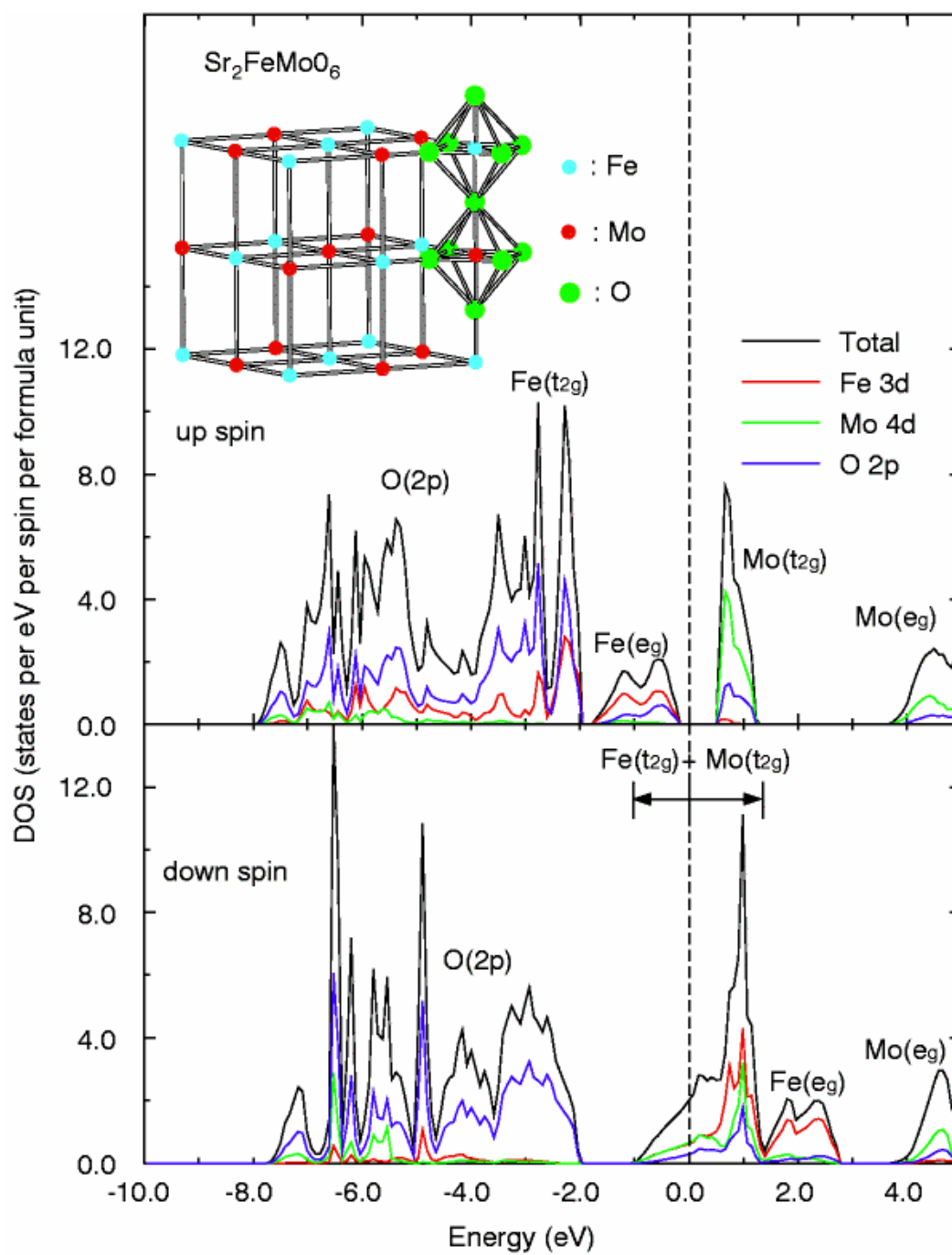
Fig.1.8. Crystal structure and the density of states (DOS) of Sr_2FeMoO_6. (K-I. Kobayashi *et al.* [53])

1.7.2 Magnetic structure

Based on band structure results, shown in Fig.1.8, it has been suggested [53] that Sr_2FeMoO_6 consists of Fe^{3+} $3d^5$ S=5/2 and Mo^{5+} $4d^1$ S=1/2 ions alternating on the perovskite B-sites. The Fe and Mo sublattices are ferromagnetically coupled within each sublattice, while the two sublattices are supposed to be antiferromagnetically coupled to give rise to an S=2 state. Within an ionic model, A_2FeMoO_6 is a ferrimagnet with Fe and Mo sublattices. Recent neutron-powder diffraction, Mössbauer spectroscopy and x-ray diffraction studies yield the following consistent picture regarding magnetic structure. Chmaissem *at al.* [65] investigated the magnetic structures of Sr_2FeMoO_6 by using neutron powder diffraction and Mössbauer spectroscopy at temperatures between 10 and 460 K. Fe and Mo atoms are found to order on alternate sites, as expected, giving rise to a double-perovskite-type unit cell. Upon cooling, a structural phase transition from cubic $Fm\bar{3}m$ to tetragonal $I4/m$ occurs at ~400 K. First Mössbauer investigations on Ca_2MoFeO_6 showed a formal Fe^{3+}/Mo^{5+} charge configuration. The Fe^{3+} $(3d^5)$ ion is in a high-spin state with $\mu_{Fe} = 5\mu_B$ and the Mo^{5+} $(4d^1)$ ion has a magnetic moment $\mu_{Mo} = 1.0\mu_B$, such that a net moment of $4\mu_B$ results [67]. Neutron diffraction data, however, indicate reduced magnetic moments between 0 and 0.5 μ_B on the Mo site coupled antiferromagnetically to Fe moments of magnitude $\mu_{Fe} = 3.7 \ldots 4.3 \mu_B$ [65, 66, 68]. In contrast to some previous suggestions, Ray *et al.* [69] found that in this compound, Fe is in the formal trivalent state and the moment at the Mo sites is below the limit of detection ($<0.25 \mu_B$). The presence of mis-site disorder between the Fe and Mo sites even in the so-called ordered samples is responsible for the observed drop in the magnetic moment from the expected value of $4 \mu_B / f.u.$ to an experimentally

observed value of about $3\,\mu_B\,/\,f.u.$ The measured isomer shift is rather large and indicates a mixed valence state of the Fe ion in A_2FeMoO$_6$ (A=Ca,Sr,Ba) compounds [64]. The electronic structure of the iron is not exactly $3d^5$ because of the partial $3d$(Fe) character of the $\downarrow$ electrons in the π^* band made up of $3d$(Fe) t_{2g} and $4d$(Mo) t_{2g} electrons. The electronic configuration of iron in the Sr and Ca compounds is close to $3d^{5.2}$, whereas that in the Ba compound is approximately $3d^5$. Now, this is in agreement with the reduced magnetic moment on the Mo site. The low-temperature magnetic moment as determined from global magnetization is often found to be considerably reduced from the ideal value of $4\,\mu_B$ to about 3-3.5 μ_B [68, 59, 70-72]. This is attributed to cation disorder on the Fe/Mo sites [73]. The drop in the magnetic moment is nearly linear with the increase in the mis-site defect concentration for the case of randomly created defects. Balcells *et al.* [72] observed a decrease of the saturation magnetization proportional to the anti-site concentration. The magnetization is reduced by $8\,\mu_B$ per anti-site in agreement with a simple ionic model. This is also consistent with the data of Tomioka *et al* [71]. From the analysis of Mössbauer spectra in A_2FeMoO$_6$ (A = Ca,Sr,Ba), Greneche *et al* [64] concluded that antisite defects predominate in comparison with antiphase boundaries. Martínez *et al.* [74] found that in Sr$_2$FeMoO$_6$, the magnetization fully saturates at low temperatures at a value of 3.75 μ_B. In the paramagnetic regime, above the Curie temperature ($T_C \approx 420\,K$), the magnetic susceptibility can be well described by a Curie-Weiss law. It is found that the experimental effective moment μ^*_{eff} is gradually reduced under a field, an effect that can be attributed to some non-intrinsic behaviour. By means of detailed data analysis, it is shown that the paramagnetic effective moment μ_{eff} is close to that expected for a $3d^6 : 4d^0$ atomic configuration. This result was interpreted as due to some electronic

charge transfer from the itinerant $4d^0$(Mo) towards the $3d^5$(Fe) orbitals in the paramagnetic phase. The Re-compounds A_2FeReO_6 are less well studied: measurements of isomer shifts, however, also indicate the mixed valence nature of Fe in these materials; Ca_2FeReO_6 and Ba_2FeReO_6, respectively, appears consistent with the Mössbauer data which show almost exclusively a high spin Fe^{3+} state for the Ca compound and a mixed high spin Fe^{2+}/Fe^{3+} state for the Ba compound [75]. In conclusion, these data indicate that the double perovskites are itinerant ferromagnets with a mixed valence of the Fe ions; the itinerant carriers are mainly of Mo(4d) and Re(5d) character.

1.7.3. Electro-transport properties

The resistivity depends sensitively on the preparation conditions, presumably due to cation disorder, grain-boundary scattering and oxygen content. In Sr_2FeMoO_6 both semiconducting and metallic behaviour have been observed [71, 76, 77, 70, 65]. Judging from measurements on a single crystal grown by the floating zone method, the stoichiometric compound has a metallic resistivity below and above the Curie temperature [71]. Niebieskikwiat *et al.* [78] found that Sr_2FeMoO_6 is very sensitive to oxidation and the resistivity is strongly dominated by the carrier scattering at the grain boundaries. When the oxygen atoms placed at the grain boundaries are removed, two metal-insulator transitions were observed, being clearly metallic below $T_C=T_{MI,1}$=405 K and above $T_{MI,2}$=590 K. For intermediate temperatures, the system presents a possible Anderson localization of the carriers with semiconducting behavior. It was also found that the residual resistivity is quite high at $200-300\mu\Omega cm$ presumably due to cation disorder scattering [71, 76]. The nature of carriers is electron-like with a density of about $1.1\times10^{28}m^{-3}$ corresponding to one electron per Fe/Mo pair [71]. The

optical conductivity in the ferromagnetic phase shows a Drude component and two excitation maxima at 0.5 and 4 eV, respectively. These have been interpreted as charge-transfer transitions from the up spin $Fe(e_{g\uparrow})$ to $Mo(t_{2g})$ band (0.5 eV) and O(2p) to $Mo/Fe(t_{2g\downarrow})$ down spin band (4 eV), respectively [71]. The insulating and metallic behavior of Ca_2FeReO_6 and Ba_2FeReO_6, respectively, appears consistent with the Mössbauer data which show almost exclusively a high spin Fe^{3+} state for the Ca compound and a mixed high spin Fe^{2+}/Fe^{3+} state for the Ba compound [79].

1.7.4. Magnetoresistance Properties

A considerable low-field magnetoresistance often appearing in magnetotransport measurements that is likely to be of extrinsic origin arising from grain-boundary or cation disorder scattering. As shown in Fig.1.9, Yuan *et al.* [80] found that the intergrain tunnelling magnetoresistance (IMR) can be enhanced significantly over a wide temperature range at low magnetic field by decreasing the grain size to nanometer scale, which makes Sr_2FeMoO_6 a promising candidate for magnetic recording materials operating at room temperature. The extrinsic magnetoresistance of polycrystalline material of Sr_2FeMoO_6 was also studied by Kim *et al.* [81]. Alonso *et al.* [82] report a magnetoresistance increasing with temperature in Ca_2FeMoO_6. A smooth decrease of MR was observed between 10 and 250 K, characterized by an abrupt drop of MR at low field, which was attributed to grain boundary effects. From 280 to 350 K, an increase in MR was found, showing a maximum close to T_C (330 K), which was attributed to intrinsic (intragrain) effects. These investigations usually show a large low-field magnetoresistance at room temperature. This is consistent with spin-polarized tunneling between half-metallic ferromagnets. Fig.1.10 compared the normalized low-field magnetoresistance as a function of the reduced temperature, T/T_C,

for half-metallic ferromagnets CrO_2, $La_{2/3}Sr_{1/3}MnO_3$, $Tl_2Mn_2O_7$ and Sr_2FeMoO_6. A clear trend emerges: the decay of the tunnelling magnetoresistance with temperature becomes smaller along this series. This was corroborated by Lee *et al.* [83]. For Sr_2FeMoO_6 the magnetoresistance is proportional to M^2 as expected for spin-polarized tunnelling. The interpretation of these data is not fully clear. The different temperature dependences seem to be related to both the interfacial magnetism and the tunnelling barrier properties. One might speculate that Sr_2FeMoO_6 has the most robust interfacial magnetization of the four compounds compared. At the same time the tunnelling barrier might contain less magnetically active localized states. On a microscopic scale the distinction between grains and barrier might not be suitable, since the transition between those is supposed to be gradual. The spin structure of the itinerant and super-exchange ferromagnets Sr_2FeMoO_6 might be less sensitive to structural disorder than in the double-exchange systems $La_{2/3}Sr_{1/3}MnO_3$ and CrO_2, since the latter show a competition between ferromagnetic double exchange and antiferromagnetic super-exchange. The double exchange mechanism is supposed to be weakened near an interface due to the reduced carrier mobility.

Although most studies suggest that the grain boundaries are responsible for the low-field MR in Sr_2FeMoO_6, there are also reports suggesting that the low-field MR is connected to the cationic disorder in double perovskites. García-Hernández *et al.* [84] observed that the magnitude of the low-field MR decreases linearly as the disorder increases. On the other hand, Navarro *et al.* [85] claim that the MR increases with an increase in antisite disorder. In their studies, the polycrystalline Sr_2FeMoO_6 samples having higher-antisite disorder showed larger MR than those with less disorder. The different observations and explanations reported in the literature indicate that the precise mechanism responsible for the MR in Sr_2FeMoO_6 is still a controversial issue.

(a)

(b)
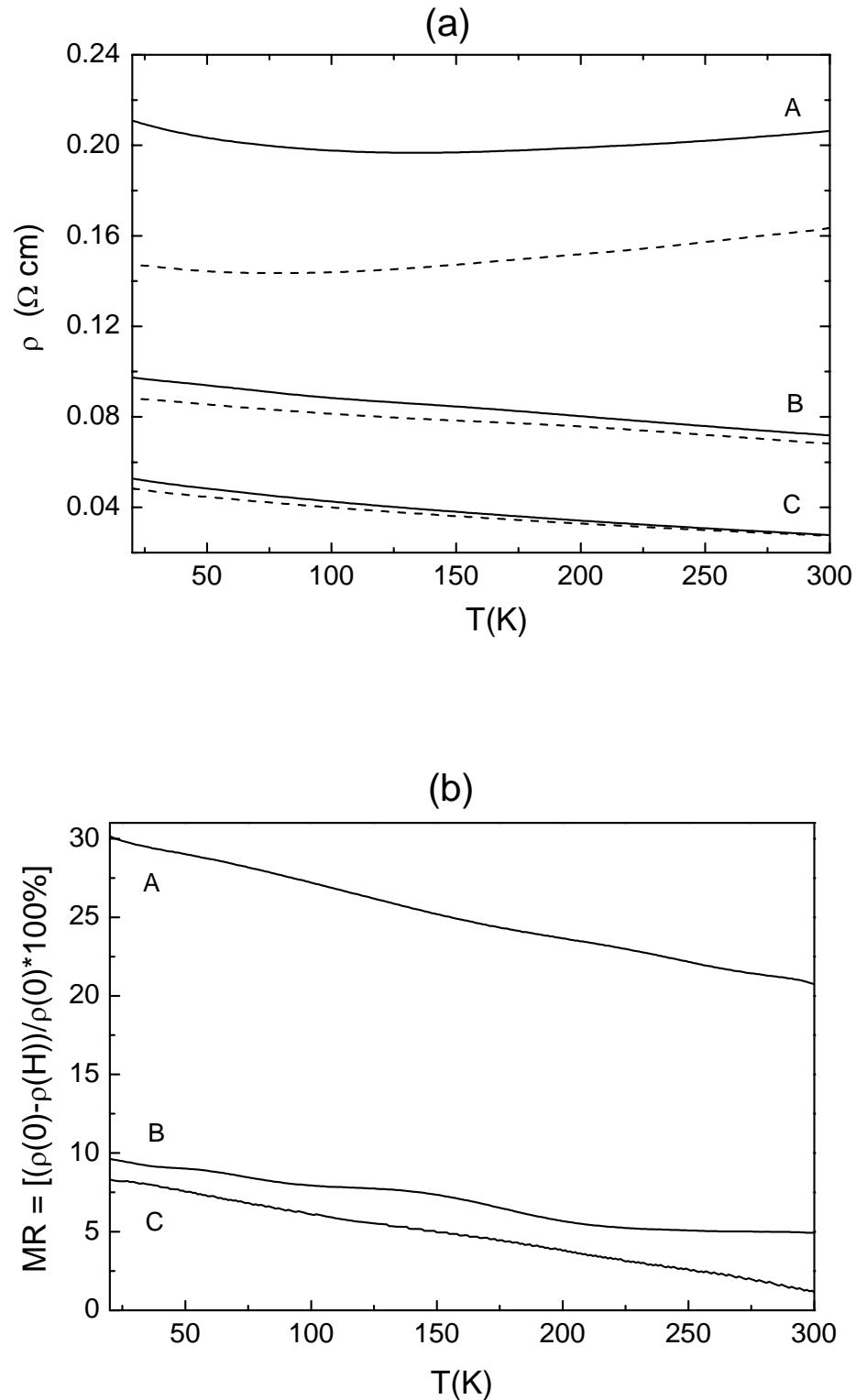
Fig.1.9. (a) Temperature dependence of the resistivity for different grain-size Sr_2FeMoO_6: samples A (29 nm), B (35 nm), C (45 nm) at zero field (solid line) and 4 kG (dash line). (b) Temperature dependence of the magnetoresistance ratio $MR = [\rho(0) - \rho(H)]/\rho(0)$ for Sr_2FeMoO_6 at 4 kG. (Yuan *et al.* [80])
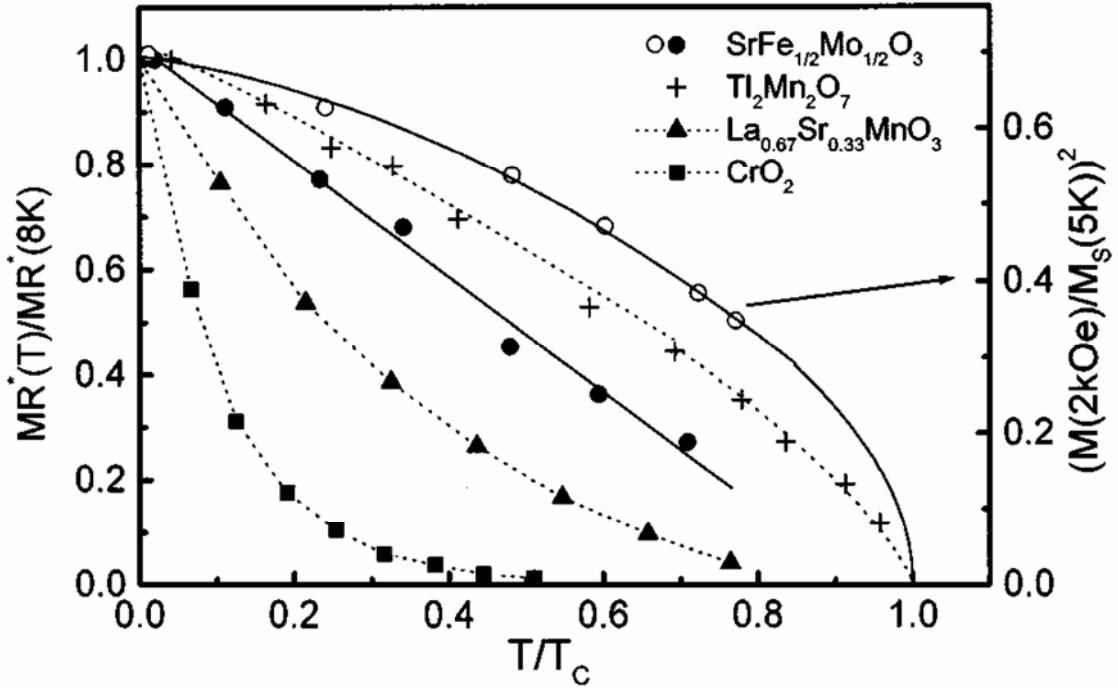
Fig.1.10. The normalized low-field magnetoresistance of Sr_2FeMoO_6, defined as $MR^* = [\rho(0) - \rho(2\,kOe)]/\rho(0)$, plotted as a function of the reduced temperature T/T_C with those of $Tl_2Mn_2O_3$, CrO_2 and $La_{0.67}Sr_{0.33}MnO_3$ (Kim *et al* [81]).

1.8. Motivation and outline of the thesis

Magnetoresistive manganese perovskites have proved to be useful for the development of field-sensitive magnetic sensors operable at room temperature. In fact, some devices based on screen-printed polycrystalline material oxides have been built showing that there are some possible niches for applications. However, the fast decay of the LFMR with temperature and the fact that the Curie temperature remains critically low represent serious drawbacks for applications requiring operation temperatures up to 150–180 ^{0}C.

In any event, half-metallic ferromagnets of higher Curie temperatures are needed. Progress on crystallochemistry of double perovskites such as Sr_2FeMoO_6, has been impressive and nowadays oxides of almost ideal bulk properties can be prepared. However, detailed understanding of the LFMR in these oxides and the nature of grain

boundaries remain elusive. Shaping of materials suitable for some applications is also starting and in addition to tremendous progress in thin film preparation, thick films are already available. However, much effort on microstructural and structural analysis is required in order to understand and progress towards the control of the LFMR. Recent results on possible ways to further raise the Curie temperature in double perovskites are encouraging and there is still room for new ideas and progress.

The motivation for this research project is due to the novel and intriguing properties of the double perovskite materials reported by Kobayashi [53] in 1998. Investigations of the magnetoresistance properties of Sr_2FeMoO_6 related to size effect were investigated in 1999 by Yuan et al. [80]. Their investigation revealed that IMR can be enhanced significantly over a wide temperature range at low magnetic field by decreasing the grain size of Sr_2FeMoO_6 to nanometer scale, making it a promising candidate for magnetic recording materials operating at room temperature [80]. The potential applications offered by this new class of materials in the field of electronics lead us to explore the physics behind the phenomena so as to propose the underlying mechanisms with regards to the intergrain tunneling magnetoresistance of the double perovskite materials, especially at a relatively low magnetic field and room temperature.

In this thesis, firstly, in Chapter One, the basics of the common MR effects are described. An in depth review of the physical properties of the double perovskite materials are also presented along with the motivation and outline of the thesis. Secondly, in Chapter Two, the method is discussed in detail. Those include the preparation of the samples by means of both sol-gel technique and solid state reaction, thin film preparation by pulsed laser deposition technique, and the methods used to evaluate of the materials properties in various aspects. Chapter Three-Six are the main

parts of this thesis. The grain boundary modification studies of Sr_2FeMoO_6 polycrystals are presented in Chapter Three. In Chapter Four, the properties of magnetotransport of $Sr_2CoMoO_{6-\delta}$ films are presented. The electrical, magnetic, and transport properties of Cu-doped polycrystalline samples $Sr_2Fe_{1-x}Cu_xMoO_6$ with ordered double perovskite structure are presented in Chapter Five. For comparison with Chapter Five, Chapter Six focuses on a subject: the effects of Cu doping on the magnetoresistive behavior of perovskites $La_{0.7}Ca_{0.3}MnO_y$. Finally in Chapter Seven, we conclude the thesis and give some suggestions on future work.

Reference:

[1].   J. M. D. Coey, *J. Mag. Mag. Mater.* **196-197,** 1 (1999)

[2].   G. Prinz, K. Hathaway, in *Phys. Today, Special Issue (April)* P24 (1995)

[3].   S. S. P. Parkin in Aspects of Modern Magnetism, Ed. By Pu F C, Wang Y J and Shang C H, (*Singapore: World Scientific*) P.118 (1996)

[4].   T. Venkatesan, M. Rajeswari, Z. W. Dong, S. B. Ogale and R. Ramesh, *Phil. Trans. R. Soc. Lond. A* **356,** 1661 (1998)

[5].   J. M. D. Coey, M. Viret, S. Molnar, *Adv. In Phys.* **48,**167 (1999)

[6].   G. turilli, *Magnetoresistance, phenomenology and applications*, P102 of *Magnetic Properties of Matter: proceedings of the National School "New Developments and Magnetism's Applications"*, Napoli, October 23-28 (1995); T. R. Mcguire and R. I. Potter, *IEEE tans. Magn.* **11**, 1018 (1975)

[7].   J. M. D. Coey, *J. Appl. Phys.* **85**, 5576 (1999)

[8].   A. E. Berkowitzet al, *Phys Rev. Lett.* **68,** 3745 (1998); JE. Evetts, MG. Blamire, ND. Mathur, et al., *Phil. Trans. R. Soc. Lond. A* **365,** 1593 (1998)

[9].   H. R. Qu, M. Lu, H. W. Zhao and K. Xia, *Progress in Physics* **17**, 159 (1997)

[10].   S. Jin, T. H. Tiefel, M. McCormack, R. A. Fastnacht, R. Ramesh and L. H. Chen, *Science* **264**, 413 (1994)

[11].   S. Jin, H. M. O'Bryan, T. H. Tiefel, M. Mccormack and W. W. Rhodes, *Appl. Phys. Lett.* **66**, 382 (1995)

[12].   Y. Shimakawa, Y. Kubo and T. Manako, *Nature* **379,** 53 (1996)

[13].   A. P. Ramirez, R. J. Cava and J. Krajewski, *Nature* **387,** 268 (1997)

[14].   M. Venkatesan, P. Velasco, J. A. Alonso, J. L. Martínez and J. M. D. Coey, *J.Phys.: Condens Matter* **16**, 3465 (2004)

[15].   Y. Moritomo, A. Asamitsu, H. Kuwahara and Y. Tokura, *Nature* **380,** 141 (1996)

[16]. C. Zener, *Phys. Rev.* **81,** 440 (1951)

[17]. P. W. Anderson and H. Hasegawa, *Phys. Rev.* **100,** 675 (1955)

[18]. P-G. De Gennes, *Phys. Rev.* **118,** 141 (1960)

[19]. J. B. Goodenough, *Magnetism and the Chemical Bond (Huntington: Krieger)* 1976

[20]. A. Urushibara, Y. Moritomo, T. Arima, A. Asamitsu, G. Kido and Y. Tokura, *Phys. Rev.* B **51,** 14103 (1995)

[21]. Y. Tokura, A. Urushibara, Y. Moritomo, T. Arima, A. Asamitsu, G. Kido and N. Furukawa, *J. Phys. Soc. Japan* **63,** 3931 (1994)

[22]. A. Asamitsu, Y. Moritomo, Y. Tomioka, T. Arima and Y. Tokura, *Nature* **373,** 407 (1995)

[23]. H. Kuwahara, Y. Tomioka, A. Asamitsu, Y. Moritomo and Y. Tokura, *Science* **270,** 961 (1995)

[24]. P. Schiffer, A. P. Ramirez, W. Bao and S-W. Cheong, *Phys. Rev. Lett.* **75,** 3336 (1995)

[25]. G. Q. Gong, C. Canedy, G. Xiao, Z. J. Sun, A. Gupta and A. Gallagher , *Appl. Phys. Lett.* **67,** 1783 (1995); G. Q. Gong, A. Gupta, G. Xiao, P. Lecoeur and T. R. McGuire, *Phys. Rev. B* **54,** R3742 (1996)

[26]. S-W. Cheong, C. M. Lopez and H. Y. Hwang, *Preprint* 1997

[27]. R. von Helmolt, J. Wecker, B. Holzapfel, L. Schultz and K. Samwer, *Phys. Rev. Lett.* **71,** 2331 (1993)

[28]. R. von Helmolt, L. Haupt, K. Bärner and U. Sondermann, *Solid State Commun.* **82,** 641 (1992)

[29]. Y. Moritomo, Y. Tomioka, A. Asamitsu, Y. Tokura and Y. Matsui, *Phys. Rev. B* **51,** 3297 (1995)

[30]. W. Bao, C. H. Chen, S. A. Carter and S-W. Cheong, *Solid State Commun.* **98,** 55 (1996)

[31]. H. Asano, J. Hayakawa and M. Matsui, *Appl. Phys. Lett.* **68,** 3638 (1996)

[32]. Y. Tomioka, A. Asamitsu and Y. Tokura, *Phys. Rev. B* **63,** 024421 (2001)

[33]. Y. Tomioka, A. Asamitsu, Y. Moritomo, H. Kuwahara and Y. Tokura *Phys. Rev. Lett.* **74,** 5108 (1995)

[34]. E. O. Wollan and W. C. Koehler, *Phys. Rev.B* **100,** 545 (1955)

[35]. A. P. Ramirez, P. Schiffer, S-W. Cheong, W. Bao,T. T. M. Palstra, P. L. Gammel, D. J. Bishop and B. Zegarski, *Phys. Rev. Lett.* **76,** 3188 (1996)

[36]. A. J. Millis, B. I. Shraiman and R. Mueller, *Phys. Rev. Lett.* **77,** 175 (1996)

[37]. H. Rӧder, J. Zhang and A. R. Bishop, *Phys. Rev. Lett.* **76,** 1356 (1996)

[38]. G. Zhao, K. Conder, H. Keller and K. A. M¨uller, *Nature* **381,** 676 (1996)

[39]. P. Dai, J. Zhang, H. A. Mook, S-H. Liou, P. A. Dowben and E. W. Plummer, *Phys. Rev. B* **54,** R3694 (1996)

[40]. J. R. Fletcher and K. W. H. Stephens, *J. Phys. C: Solid State Phys.* **2,** 444 (1969)

[41]. J. B. A. Elemans, B. Van Laar, K. R. Van Der Veen and B. O. Loopstra, *J. Solid State Chem.* **3,** 238 (1971)

[42]. A. J. Millis, P. B. Littlewood and B. I. Shraiman, *Phys. Rev. Lett.* **74**, 5144 (1995)

[43]. A. J. Millis, P. B. Littlewood and B. I. Shraiman, *Phys. Rev. Lett.* **77**, 175 (1996)

[44]. A. J. Millis, *Phys. Rev. Lett.* **80**, 4358 (1998)

[45]. S. J. L. Billinge *et al*., *Phys. Rev. Lett.* **77**, 715 (1996)

[46]. J. M. D. Teresa *et al*., *Nature* **386,** 256 (1997)

[47]. D. D. Sarma *et al*., *Phys. Rev. B* **53**, 6873 (1996)

[48]. C. Meneghini *et al.*, *Phys. Rev. B* **56**, 3520 (1997)

[49]. C. Meneghini *et al.*, *Phys. Stat. Solidi* **215**, 647 (1999)

[50]. C. N. R. Rao and R. Mahesh, *Current Opinion in Solid State and Material Science* **2**, 32 (1997)

[51]. C. N. R. Rao and A. Arulraj, *ibid* **3**, 23 (1998)

[52]. S. von Molnar and J. M. D. Coey, *ibid* **3**, 171 (1998)

[53]. K-I. Kobayashi, T. Kimura, H. Sawada, K. Terakura and Y. Tokura, *Nature* **395** 677 (1998)

[54]. F. K. Patterson, W. C. Moeller and R. Ward, *Inorg. Chem.* **2**, 196 (1963)

[55]. F. S. Galasso, *J. Chem. Phys.* **44,** 1672 (1966)

[56]. J. M. Longo and R. Ward, *J. Am. Chem. Soc.* **83,** 1088 (1961)

[57]. A. W. Sleight, J. M. Longo and R. Ward, *Inorg. Chem.* **1,** 245 (1962)

[58]. A. W. Sleight and J. F. Weiher, *J. Phys. Chem. Solids* **33,** 679 (1972)

[59]. R. P. Borges, R. M. Thomas, C. Cullinan, J. M. D. Coey, R. Suryanarayanan, L. Ben-Dor, L. Pinsard-Gaudart and A. Revcolevschi, *J. Phys.: Condens. Matter* **11,** L445 (1999)

[60]. A. Arulraj, K. Ramesha, J. Gopalakrishnan and C. N. R. Rao, *J. Solid State Chem.* **155,** 233 (2000)

[61]. K-I. Kobayashi, T. Kimura, Y. Tomioka, H. Sawada, K. Terakura and Y. Tokura, *Phys. Rev.* *B* **59,** 11159 (1999)

[62]. N. Hamada and Y. Moritomo，*The 3rd Japan-Korea Joint Workshop on First-Principles Electronic Structure Calculations*, P. 56 (2000)

[63]. Y. Moritomo, S. Xu, A. Machida, T. Akimoto, E. Nishibori, M. Takata and M. Sakata, *Phys. Rev. B* **61**, R7827 (2000)

[64]. J. M. Greneche, M. Venkatesan, R. Suryanarayanan and J. M. D. Coey, *Phys. Rev. B* **63,** 174403 (2001)

[65]. O. Chmaissem, R. Kruk, B. Dabrowski, D. E. Brown, X. Xiong, S. Kolesnik, J. D. Jorgensen and C. W. Kimball, *Phys. Rev. B* **62,** 14197 (2000)

[66]. C. Ritter, M. R. Ibarra, L. Morellon, J. BlascotJ, J. García and J. M. de Teresa, *J. Phys.: Condens. Matter* **12,** 8295 (2000)

[67]. L. Pinsard-Gaudart, R. Suryanarayanan, A. Revcolevski, J. Rodriguez-Carvajal, JM. Greneche *et al. J. Appl. Phys.* **87,** 7118 (2000)

[68]. B. García-Landa, C. Ritter, IbarraMR, J. Blasco, P. A. Algarabel, R. Mahendiran and J. García, *Solid State Commun.* **110,** 435 (1999)

[69]. S. Ray, A. Kumar, D. D. Sarma, R. Cimino, S. Turchini, S. Zennaro and N. Zema, *Phys. Rev. B* **87,** 097204 (2001)

[70]. T. Manako, M. Izumi, Y. Konishi, K-I. Kobayashi, M. Kawasaki and Y. Tokura, *Appl. Phys. Lett.* **74** 2215 1999

[71]. Y. Tomioka, T. Okuda, Y. Okimoto, R. Kumai, K-I. Kobayashi and Y. Tokura, *Phys. Rev. B* **61,** 422 (2000)

[72]. L1. Balcells, J. Navarro, M. Bibes, A. Roig *et al.*, *Appl. Phys. Lett.* **78,** 781 (2001)

[73]. A. S. Ogale, S. B. Ogale, R. Ramesh and T. Venkatesan, *Appl. Phys. Lett.* **75,** 537 (1999)

[74]. B. Martínez, J. Navarro, L1. Balcells and J. Fontcuberta, *J. Phys.: Condens. Matter.* **12,** 10515 (2000)

[75]. J. Gopalakrishnan, A. Chattopadhyay, S. B. Ogale, T. Venkatesan, R. L. Greene, A. J. Millis, K. Ramesha, B. Hannoyer and G. Marest, *Phys. Rev. B* **61,** 9538 (2000)

[76]. W. Westerburg, D. Reisinger and G. Jakob, *Phys. Rev. B* **62,** R767 (2000)

[77]. H. Asano *et al*, *Appl. Phys. Lett.* **74,** 3696 (1999)

[78]. D. Niebieskikwiat, R. D. Sánchez A. Caneiro, L. Morales, M. Vásquez-Mansilla, F. Rivadulla, and L. E. Hueso, *Phys. Rev. B* **62,** 3340 (2000)

[79]. J. Gopalakrishnan, A. Chattopadhyay, S. B. Ogale, T. Venkatesan, R. L. Greene, A. J. Millis, K. Ramesha, B. Hannoyer and G. Marest, *Phys. Rev. B.* **61**, 9538 (2000)

[80]. C. L. Yuan, S. G. Wang, W. H. Song, T. Yu, J. M. Dai, S. L. Ye, Y. P. Sun, *Appl. Phys. Lett.***75**, 3853 (1999)

[81]. T. H. Kim, M. Uehara, S-W. Cheong and S. Lee, *Appl. Phys. Lett.* **74**, 1737 (1999)

[82]. J. A. Alonso, CasaisMT, Martínez-LopeMJ, J. L. Martínez, P. Velasco, A. Muñoz and Fernández-DíazMT, *Chem. Mater.* **12,** 161 (2000)

[83]. S. Lee, H. Y. Hwang, B. I. Shraiman, et al. *Phys. Rev. Lett.* **82** 4508 (1999)

[84]. M. García-Hernández, J. L. Martínez-Lope, M. T. Casais, and J. A. Alonso, *Phys. Rev. Lett.* **86**, 2443 (2001).

[85]. J. Navarro, L. I. Balcells, F. Sandiumenge, M. Bibes, A. Roig, B. Martínez, and J. Fontcuberta, *J. Phys.: Condens. Matter.* **13**, 8481 (2001).

Chapter 2

Apparatus and experimental details

2.1. Sample preparations

2.1.1. Sol-gel method

The chemical methods such as sol-gel routine were developed as new ceramic synthesis techniques. These methods have the advantage to achieve improved chemical homogeneity on the molecular scale. Therefore, the diffusion distance is reduced on calcinations compared to the conventional preparations that favor the lower crystallized temperatures for multi-component ceramics.

Bulk Sr_2FeMoO_6 sample was prepared by the sol-gel method followed by heat treatment at different temperatures. Briefly, the method consisted of weighing stoichiometric quantities of $(NH_4)_6Mo_7O_{24} \cdot 4H_2O$, $Fe(NO_3)_3 \cdot 9H_2O$, $Sr(NO_3)_2$, preparing them in solution form, and mixing the solutions of $Sr(NO_3)_2$ and $(NH_4)_6Mo_7O_{24} \cdot 4H_2O$ with nitric acid according to the proportion of ~10 times in moles of $(NH_4)_6Mo_7O_{24} \cdot 4H_2O$. The resultant mixture was then mixed with the solution of $Fe(NO_3)_3 \cdot 9H_2O$ to form a light green gel after several minutes. The gel was dried at 60°C, and then powderized by high-energy ball milling for 3 h. It was then preheated at 700 °C for 6 h and further milled by high-energy ball milling for another 3 h. Finally, the powder was pressed into pellets, followed by sintering at 900 °C in the ambience of a controlled stream of various proportions of gaseous H_2-Ar mixtures for 3 h. The Sr_2FeMoO_6 sample synthesis procedure by the sol-gel method is shown in Fig. 2.1.

The oxygen-stoichiometric Sr_2CoMoO_6 perovskite was prepared as a black

polycrystalline powder from citrate precursors obtained by Sol-gel method. Stoichiometric amounts of analytical grade $Sr(NO_3)_2$, $Co(NO_3)_2 \cdot 6H_2O$, and $(NH_4)_6Mo_7O_{24} \cdot 4H_2O$ were dissolved in citric acid. The citrate + nitrate solutions were slowly evaporated, leading to organic resins containing a random distribution of the involved cations at an atomic level. These resins were first dried at 150 ^{o}C and then slowly decomposed at temperatures up to 400 ^{o}C, and finally powderized by high-energy ball milling for 3 h. All the organic materials and nitrates were eliminated in a subsequent treatment at 700 ^{o}C in air, for 6 h, and then milled by high-energy ball milling for another 3 h. This treatment gave rise to highly reactive precursor materials. Afterward, the resulting black powder was pressed into pellets, followed by sintering at 900 °C in the ambience of a controlled stream of various proportions of gaseous H_2-Ar mixtures for 3 h. The Sr_2CoMoO_6 sample synthesis procedure by the sol-gel method is shown in Fig.2.2.

2.1.2. Solid-state reaction

The solid-state reaction is the most conventional synthesis method for preparing the multi-component ceramics. This method involves repeated grinding, compaction and firing of the component oxides until a single-phase material is achieved. As a standard variant, the carbonates or the oxalates are also used as precursors for the oxides. Upon the first heating or calcining, the precursors decompose to the ultrafine grain oxide powers. The high reactivity of the powders helps the solid-state reactions process in the following sintering. As the solid-state reaction method depends on the inter-diffusion between the oxide powders, it is necessary to use fine, well-compacted powders and to sinter them under a temperature high enough for the diffusion length to exceed the particle size. The advantages of the solid-state reaction are the ready

availability of oxide precursors, low cost and the precise weighing of oxide precursors and the reaction components.

Bulk $La_{0.7}Ca_{0.3}Mn_{1-x}Cu_xO_y$ samples were prepared by the conventional solid-state reaction processing in air. Stoichiometric proportions of La_2O_3, $CaCO_3$, $MnCO_3$ and CuO were mixed and ground, then fired at 1000°C for 24 h. After grounding, the resulting mixture was pelleted and sintered in air at 1200°C for 24 h and at 1250°C for another 24 h, with several intermediate grindings. Finally, the furnace was cooled down to room temperature naturally. The $La_{0.7}Ca_{0.3}Mn_{1-x}Cu_xO_y$ sample synthesis procedure by the solid-state reaction is shown in Fig.2.3.

| $(NH_4)_6Mo_7O_{24}\cdot 4H_2O$ | $Sr(NO_3)_2$ | | $Fe(NO_3)_3\cdot 9H_2O$ |

+H₂O

+H₂O   +HNO₃

Solution   Solution

Light green gel

Dry at 60 °C

Brown powder

Ball milling (3 h)   Sintering at 700 °C (6 h)

Black Powder

Ball milling (3 h)

Press into pellets

H₂+Ar
Sintering at 900 °C (3 h)

Sr₂FeMoO₆

Fig.2.1. The Sr₂FeMoO₆ sample synthesis procedure by the sol-gel method

| $(NH_4)_6Mo_7O_{24}\cdot 4H_2O$ | $Sr(NO_3)_2$ | $Co(NO_3)_2\cdot 6H_2O$ |

+HNO$_3$ Evaporate
+Citric acid

Organic resins

Dry at 150 ^{o}C   Sintering at 400 ^{o}C (6 h)

Black powder

Ball milling (3 h)

Black Powder

Sintering at 700 ^{o}C (6 h)   Ball milling (3 h)

Press into pellets

H$_2$+Ar
Sintering at 900 ^{o}C (3 h)

Sr$_2$CoMoO$_6$

Fig.2.2. The Sr$_2$CoMoO$_6$ sample synthesis procedure by the sol-gel method
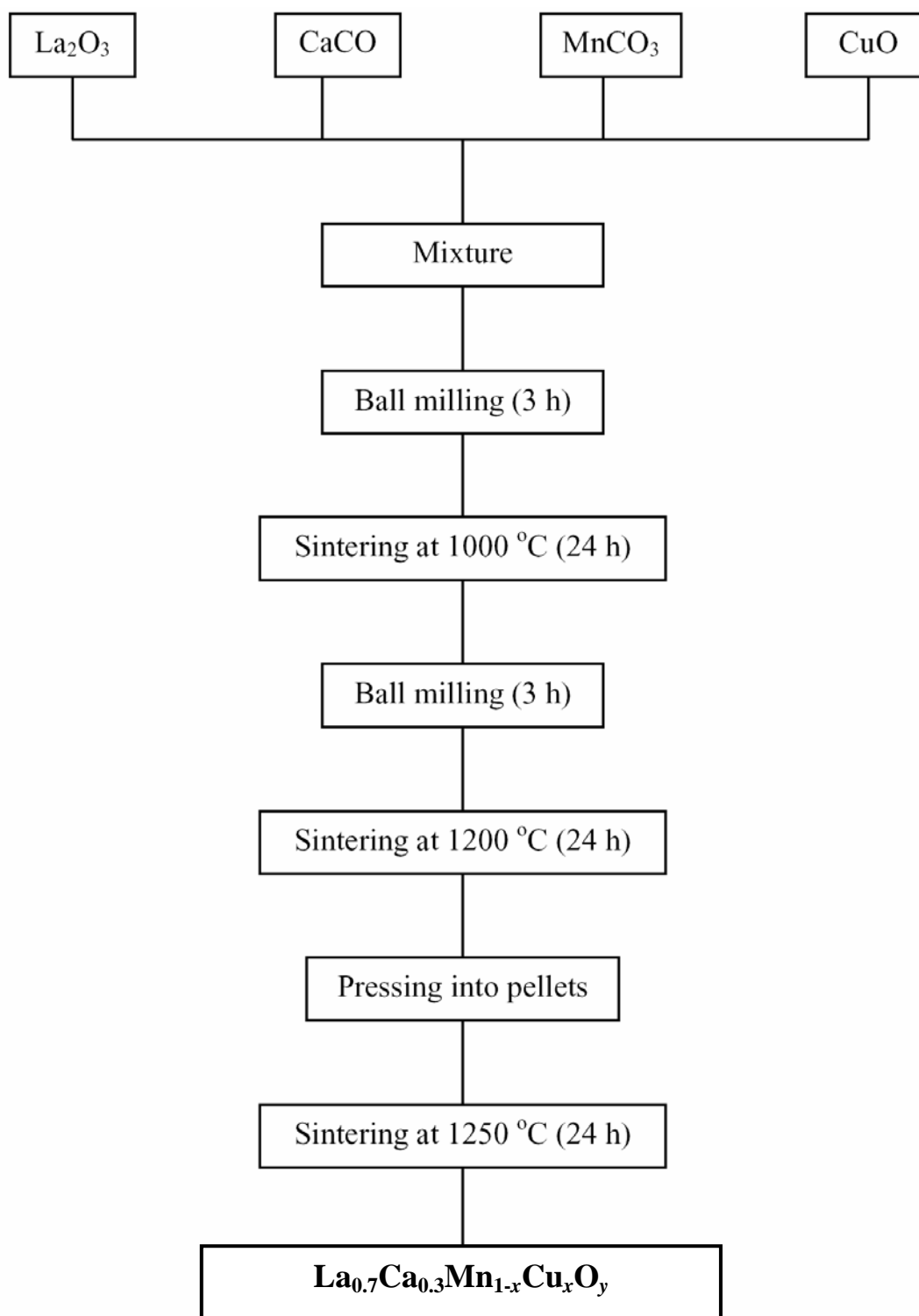
Fig.2.3. The $La_{0.7}Ca_{0.3}Mn_{1-x}Cu_xO_y$ sample synthesis procedure by the solid-state reaction

2.1.3. Thin film deposition by PLD method

PLD remained little known until the late 1980s, despite the fact that the first experiment which was carried out some thirty years ago had demonstrated the ease which material was vaporized by intense laser radiation and used to deposit thin films. One possible reason was competition from other thin-film growth deposition techniques such as sputtering and molecular beam epitaxy (MBE). Sputtering has been successfully used to deposit thin films of metal, dielectrics and oxides, whereas MBE has been focused on the growth of group III to IV semiconductor epitaxy layers. Another reason was that PLD never had a well-identified focal point and earlier efforts and works had spread too thin among the deposition of different materials.

The first major breakthrough came in mid 1970s with the development of electronic Q-switching, which enables the delivery of short pulses with high peak power density exceeding 108 W/cm^2. This broadens the scope of materials that can be deposited because laser radiation of such short pulses can readily transform the materials to form plasma with congruent evaporation. The second was triggered by the successful growth of high Tc superconducting films in 1987, which literally lifted PLD off the ground. Subsequent-pioneering works further convinced skeptics and opened the floodgate that has led to many other studies.

Pulsed Laser Deposition (PLD) is an extremely versatile technique for preparing a wide range of thin films and multi-layered structures for any kind of materials by using appropriate lasers. Its advantages include flexibility, fast response, and congruent evaporation of energetic evaporates. It has a cost advantage over many other vacuum techniques. For example, it costs 10 times less than MBE system but is capable of producing similar high-quality films, and is thus readily accepted among material scientists.
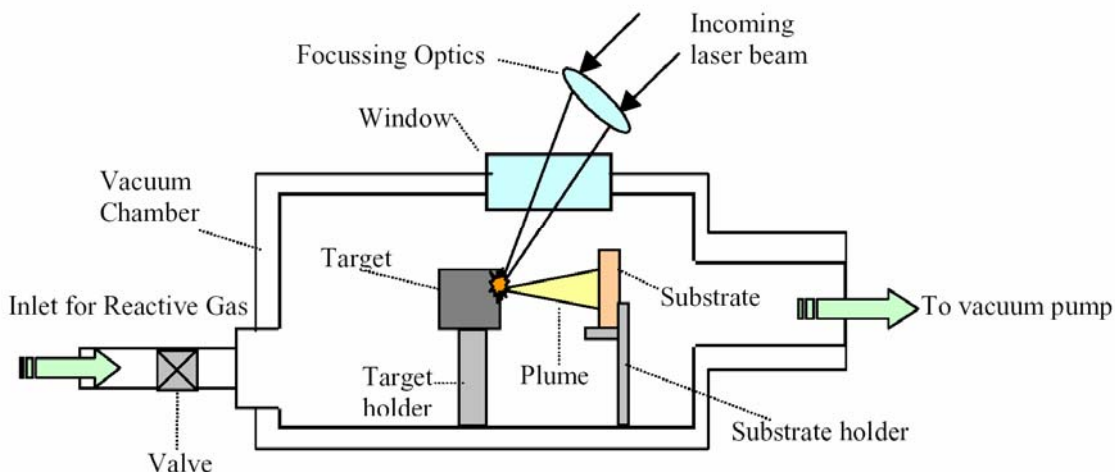
Fig.2.4. Illustration of Pulsed Laser Deposition (PLD) system

The basic setup for the PLD technique includes a target and a substrate holder placed within a vacuum chamber, and a high-power laser which is used as an external energy source to vaporize materials from the target and to deposit a layer of thin film onto a substrate (see Fig. 2.4). A set of optical components consisting of lens and mirrors is required to focus and raster the laser beam onto the target surface.

When laser radiation is absorbed by a solid target surface, electromagnetic energy is first converted to electronic excitation and then to thermal, chemical, and even mechanical energies, which then cause evaporation, ablation, excitation, plasma formation. The evaporated materials form a plasma plume which consists of a mixture of energetic species of atoms, molecules, electrons, ions and micron-sized solid particulates. Immediately after laser irradiation, the plume rapidly expands in a conical fashion from the target surface and into the vacuum with hydrodynamic flow characteristics.

Both conceptually and experimentally, PLD is extremely simple, probably the simplest among all thin film growth techniques. As the vacuum hardware and the evaporation power source are not grouped together within the vacuum chamber, PLD

technique is flexible and easily adaptable to different operational modes in comparison to techniques imposed by internally powered evaporation sources. In addition, film growth can be carried out in a reactive environment containing any kind of gas, with or without plasma excitation.

In our experiment, Nd:YAG pulsed laser (Spectra-Physics, GCR-170) beam of 355 nm wavelength 10 Hz pulse frequency was used to ablate the target in an ultrahigh vacuum chamber. With Q-switching, the laser pulse width was generally less than 10 ns and its power could reach 10^8 W. The substrate selected was (001) oriented single crystal $SrTiO_3$ and the substrate temperature is ~500 ^{o}C. The distance between target and substrate is about 5 cm.

2.2. Structure characterization

2.2.1. X-ray diffraction

X-ray diffraction from crystalline solids occurs as a result of the interaction of X-rays with the electron charge distribution in the crystal lattice. The ordered nature of the electron charge distribution, whereby most of the electrons are distributed around regularly arranged atomic nuclei with translational periodicity, means that superposition of the scattered X-ray amplitudes will give rise to regions of constructive and destructive interference producing a diffraction pattern.

The diffraction maxima are sometimes individually considered to be the result of diffraction of the incident X-ray beam of wavelength λ from crystal lattice planes, having Miller indices hkl and spacing d_{hkl}. Diffraction occurs at an angle of incidence equal to the Bragg angle θ_B, i.e. Bragg's law is obeyed:

$$n\lambda = 2d_{hkl} \sin\theta_B \tag{2-1}$$

The relative amplitude Γ_{hkl} and phase ϕ_{hkl} of a reflected X-ray are dependent on the arrangement of atoms within the crystal with respect to the lattice plane being considered and are thus ultimately dependent on the atomic structure of the basis group i.e. that group of atoms which assemble in a repeated and ordered fashion to form the resulting crystal structure. The amplitudes and phases of the diffracted beams therefore contain information about the internal structure of the crystal. In fact at a position (x, y, z) in a unit cell of volume V, the electron density $\rho(r)$ is directly related to the set of Γ_{hkl}'s and ϕ_{hkl}'s *via* a discrete Fourier transform, i.e.

$$\rho(x, y, z) = \frac{1}{V} \sum_{hkl} \Gamma_{hkl} \exp(\phi_{hkl}) \exp(2\pi(hx + ky + lz)) \qquad (2\text{-}2)$$

This is the basis of the technique of structural analysis by X-ray crystallography. With knowledge of the amplitude and phase of each diffracted X-ray a map of the electron density distribution within the unit cell may be calculated. In Fig.2.5, the conditions for Bragg scattering and the detector arrangement are illustrated.

In our experiments, we used a Philips PW1710 diffractometer with a *Cu Kα* radiation source ($\lambda = 1.5418 \overset{\text{o}}{\text{A}}$), combined with the computer running *PC-APD* analytical software for peak identification. The scan modes were $\theta - 2\theta$ and omega, for this instrument does not have a $\phi - scan$ accessory. Generally we select sampling time of 1 second and the step size of 0.02^{o}. We also adopted the free software *winfit* (from Stefan Krumm) to fit the powder XRD spectrum. The main peak positions obtained, either by peak search or fitting, were input into another free software XLAT (from Bernhard Rupp) together with standard powder diffraction data and the crystal system, so that the unit cell constants could be refined.
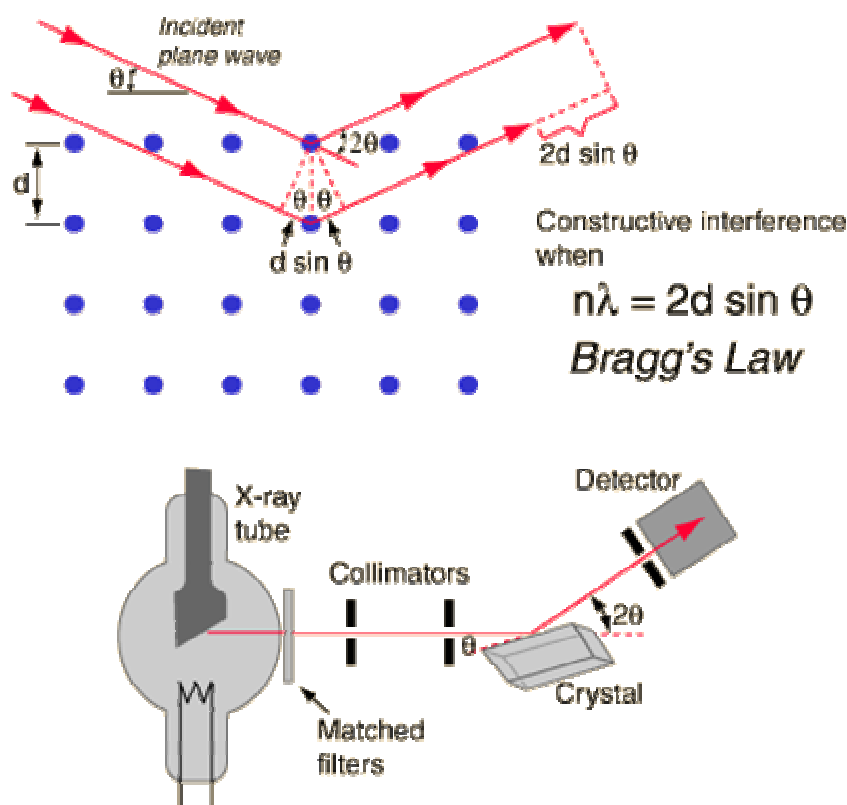
Fig.2.5. (a) Conditions for Bragg scattering (b) Detector arrangement

2.2.2. Raman Spectroscopy

Raman spectroscopy as a local probe is very sensitive to crystallinity and microstructures of materials and hence was employed to monitor the phase formation process of the perovskite materials from namely solid-state reactions of mixed oxides and soft chemistry methods, all of which involved starting materials which can be either crystalline or amorphous. Raman spectroscopy has several fundamental advantages such as non-destructive non-contact and no sample preparation required. Contributions of Raman spectroscopy to solid state and materials science are partly due to the evolution of Raman instruments, especially in the past ten years.

Raman measurements in this experiment were performed using an ISA Jobin

Yvon-Spex T64000 Triple Grating system with a backscattering geometry, coupled with an Olympus microscope attachment and a liquid-nitrogen cooled CCD detector. An argon-ion laser at 514.5 nm and 488 nm was used as the exciting light source and the instrumental resolution was 0.67 cm^{-1}. Fig. 2.6 shows the Jobin Yvon-Spex T64000 Triple Grating system.
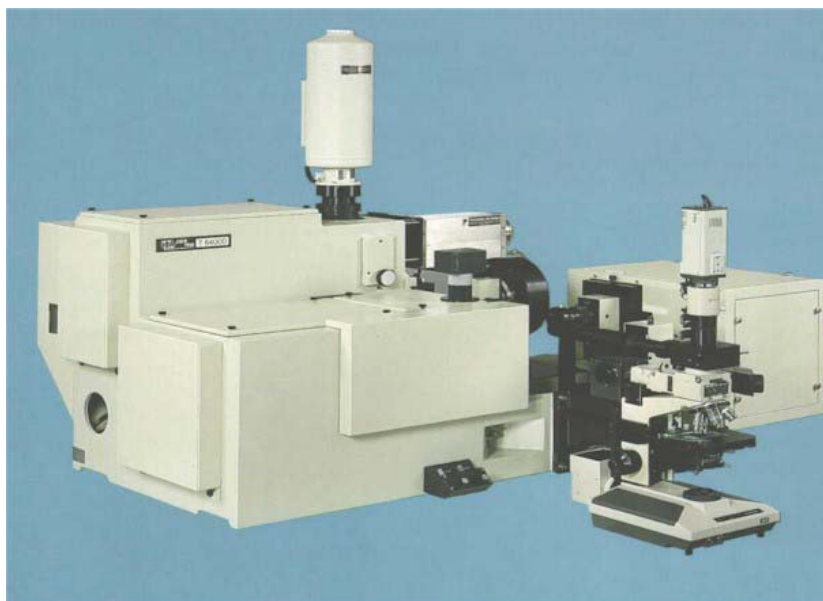
Fig.2.6. The Jobin Yvon-Spex T64000 Triple Grating system.

Like most Raman spectrometer, the Jobin Yvon-Spex T64000 system consists of 4 basic components: (1) An intense monochromatic light source-the laser, (2) a sample illuminating system, (3) triple spectrograph and (4) a signal processing system, including a nitrogen-cooled CCD detector, an amplification system, computer system for instrument control and data acquisition and processing.

The sample to be examined is placed in the sample stage and is viewed using an incident white light either on a TV monitor connected to the closed circuit viewing system (CCTV) or through the eyepieces. The sample area of interest is then located and irradiated by a visible laser beam. The light source emits a directional polarized beam which is directed onto a semi-reflecting mirror (beam splitter) in an optical

microscope. A portion of the incident laser radiation is reflected downwards through the microscope objective lens which serves to focus the laser beam to a diffraction limited spot on the sample and to collect the scattered radiation from the sample, while the other portion is transmitted through the beam splitter. The reflection and transmission characteristics of the beam splitter are determined by the dielectric coating used. The scattered radiation collected is then directed and focused by coupling optics onto the entrance slit of the grating spectrometer, which acts as the tunable filter. The output of the grating spectrometer is focused on the CCD and the resultant signal is recorded in a micromputer, which is used to control the spectrograph and detector.

2.2.3 Scanning Electron Microscopy (SEM)

SEM is an essential analyzing technique for exploring microstructures of ceramic materials. The working principle of SEM is illustrated schematically in Fig.2.7. A fine "probe" beam of electrons from an electron gun is focused on the specimen surface. The electron beam is controlled by a scan generator that allows it to scan in a raster-like pattern over the specimen surface. When electrons collides the specimen surface, various signals are created. These signals are then collected by the detectors, amplified and converted into electrical signals. They are finally sent to a cathode ray tube (CRT), which is used to control the intensity of the scanning spots to generate the on-screen image. Since the positions of the spots on the CRT scan in the same way as the scan generator that controls the incident electron beam, CRT can therefore produce magnified images according to the brightness and contrast based on the signals picked up from the specimen surface.

There are several emissions that can be created during the interaction between electrons and specimen surface, including X-rays, photons, backscattering electrons,

and the secondary electrons (SE). These emissions can be collected and utilized to analyze the surface morphology and composition of the specimen, as described below:

1. Secondary electron (SE): It is the most commonly used emission in SEM, which is produced when the energy of the incident electron beam is absorbed by the atoms of the specimen, leading to ionization and generation of low-energy secondary electrons. Secondary electrons are very sensitive to the surface morphology of the specimen, and are therefore used to produce surface images.

2. Backscattering electron (BSE): It occurs when the incident electrons are scattered backwards. Production of the backscattered electrons is closely dependent on the atomic weights of elements presented in the specimen. Thus, BSE gives a contrast image of the elemental distribution on specimen surface, based on the difference in atomic weight of the elements.

3. Energy dispersive X-ray (EDX): When a low energy (usually K-shell) electron is emitted, a high energy electron will fall into the low energy level to fill the vacancy, in turn generating X-rays to balance the total energy. The emitted X-ray shows a characteristic energy or wavelength, which is unique to the element from which it originates. Thus the X-ray can be utilized to qualitatively analyze the elemental content of a selected area in specimen. In addition, EDX can also be used to generate EDX compositional mapping which provide spatial distribution of various elements in the specimen.

In this study, sintered samples were characterized using a Philips XL-FEG scanning electron microscope (Philips FEG-SEM XL 30), which has an X-ray microanalysis attachment for EDX. Each sample was first dispersed on the surface of a conducting tape before being coated with a layer of conducting film, e.g. gold or

carbon film deposited by a sputter Coater (SCD 005 Sputter Coater).
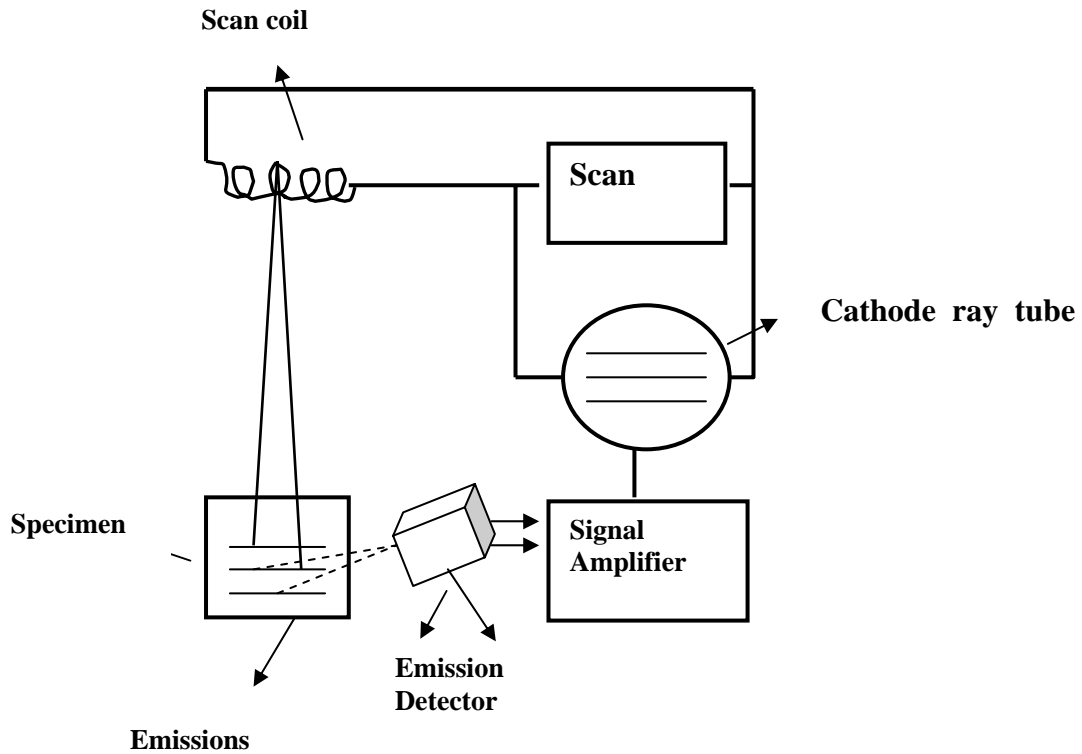
Fig.2.7. Schematic diagram of a scanning electron microscopy

2.3. Electro-transport and magneto-transport measurements

A standard technique to measure resistivity is typically referred to as a Van der Pauw four-point measurement. A current is applied to the sample across two adjacent contacts, and the voltage drop across the material is measured using the other two contacts, as shown in Fig.2.8. From knowledge of the current applied and a geometric factor involving the arrangement of the contacts one may convert the voltage measurement directly into a resistivity value. It is best if the current is kept constant, so that changes in voltage truly represent changes in resistivity. A standard trick to accomplish this is using a 'bias' resistor connected in series with the sample. The value chosen should be large enough that the sample resistance may be neglected in calculating the current in the circuit.

A drawback of four-probe measurements is that the resistance measured is dependent on the geometry of the sample and the probe. This is due to the geometry dependence of the current distribution in the sample. Therefore in order to get an accurate value of ρ, the sample usually needs to be patterned to a narrow bridge of about 20-30 um.

The four-probe measurement system employed in our laboratory is sketched in Fig. 2.8. First of all, the film was greased to a copper holder to ensure a good thermal contact. The temperature sensor, a thermal couple, or a Pt100, or a silicon diode was inserted into the copper holder. It is most important to make sure that the sample is kept at the same temperature as the sensor at all times. The heating coil was wrapped on the copper holder in order to control the temperature ramp. Four enameled copper wires with diameter of 0.1 mm were soldered using indium on the electrodes to connect the sample to the sample holder. Then the sample holder was covered and sealed using an O-ring. Vacuum pumping for 5 min is necessary to prevent the vapor from impairing the sample at low temperatures. If a faster cooling down speed and thus a good thermal conduction is needed, the sample holder can be filled with helium.

The measuring current, usually in the range of 1 uA to 10 mA, was supplied by an Advantest R6142 programmable DC voltage/current generator. The voltage on the sample was measured using a Keithley 181 nanovoltmeter. The temperature T was controlled using a Lakeshore 321 autotuning temperature controller. An analog signal of temperature reading between 0 and 10 V was output by the controller and was collected by a Keithley 2000 multimeter. The magnet used in our experiments was the Walker Scientific HF-7 electro-magnet with a water-cooling system and the maximum magnetic field available was about 15 KOe. The magnetic field was read by a magnetometer with a Hall probe and the data were also collected by a similar

multimeter. All the experimental data were automatically recorded by the PC.
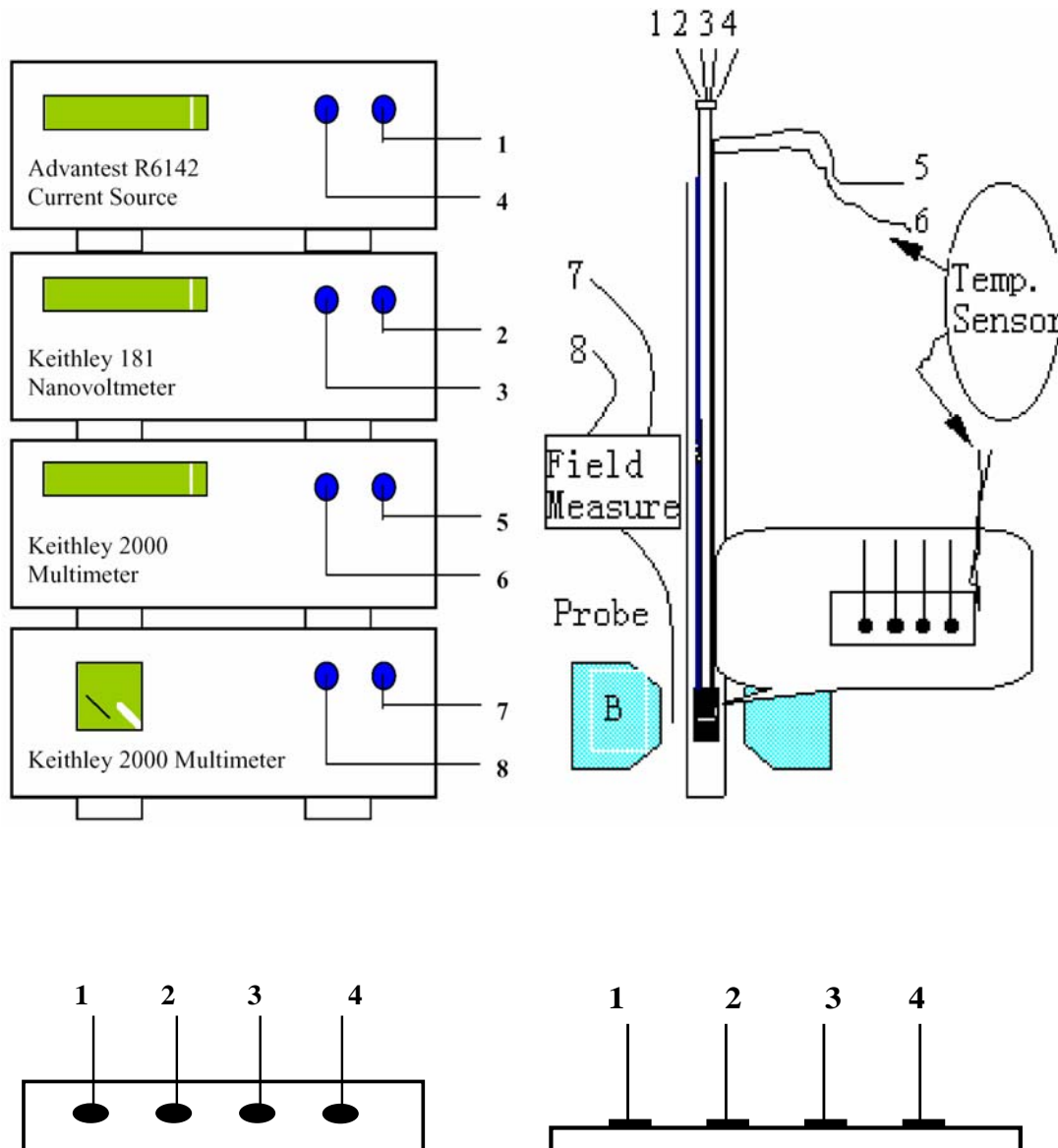
Fig.2.8. Schematic illustration of the experimental set-up for the 4-point probe measurement

2.4. Vibrating sample magnetometer (VSM)

Vibrating sample magnetometer (VSM) is widely used in magnetic materials research to measure the magnetic properties. In a VSM, the time rate of change of magnetic flux in the pick-up coil is produced by mechanically vibrating the magnetized sample. The general arrangement is shown in Fig.2.9. The magnetizing field in VSM can be provided either by an electromagnet or superconducting coils. If superconducting coils are used, magnetic fields as high as several ten teslas can be easily reached. The magnetic field in a VSM can be changed only slowly, over periods of tens of seconds. The sample is suspended on a non-magnetic rod, which vibrates vertically over amplitude of perhaps 1.5 mm, at a frequency of 45 Hz. The pick-up coils are connected in pull-push. That is, as the sample ascends, both the coils produce the same electrical polarity. The AC voltage, which is proportional to sample's magnetic moment, produced by these coils is taken to an extremely high-gain lock-in amplifier. This lock-in amplifier is effectively an extremely narrow bandwidth amplifier. The rectified output is then applied to a computer and the operation and data processing are all controlled by it.

In the present study, an Oxford instrument superconducting VSM with a maximum applied field of 90 kOe is used. The magnetic moment resolutions are about 10^{-5} to 10^{-4} emu. The VSM is also equipped with a low temperature controlling system, by which magnetic measurements at low temperatures are conducted.
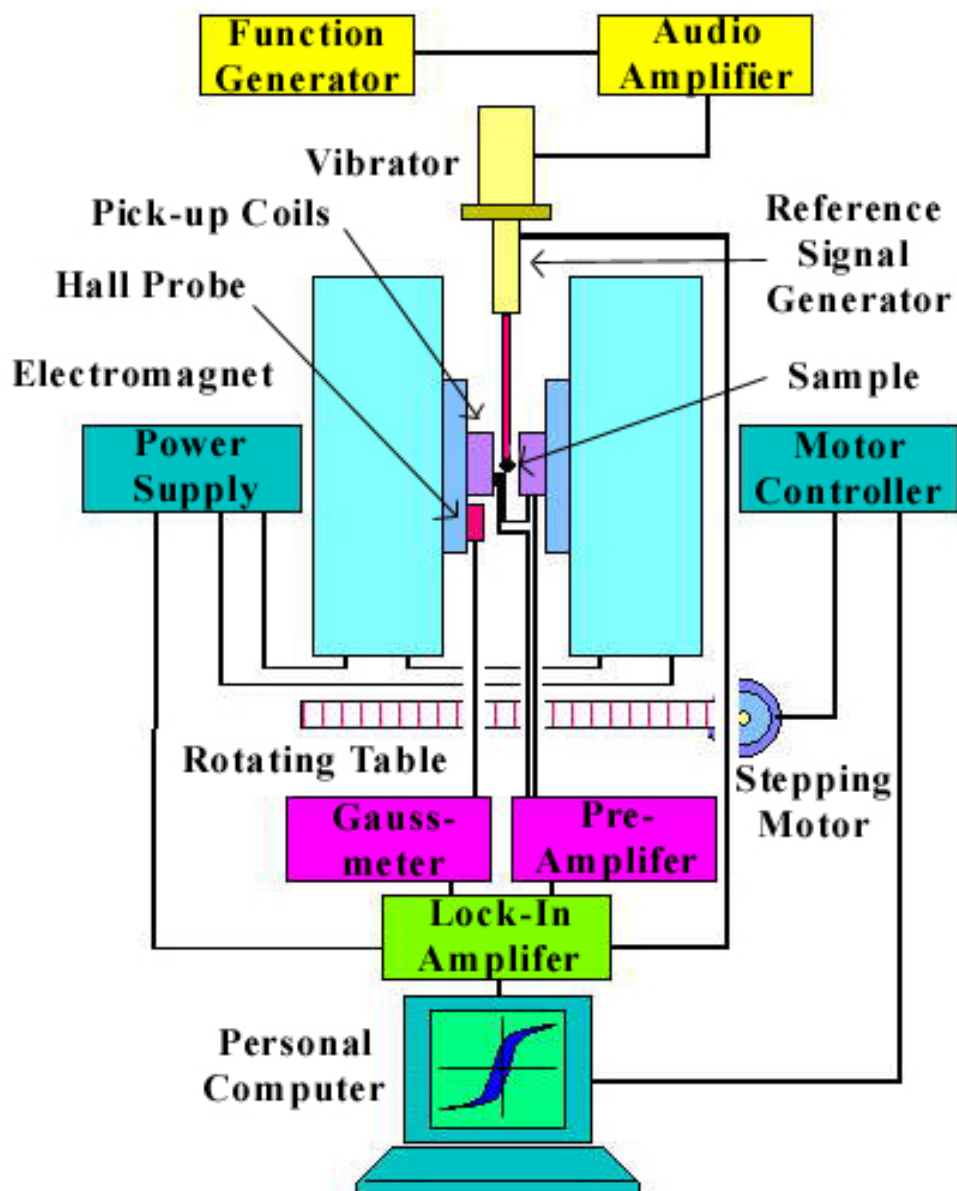
Fig.2.9. System diagram of Vibrating sample magnetometer (VSM)

Chapter 3

Grain boundary modification of Sr$_2$FeMoO$_6$ polycrystals

Although the low-field magnetoresistance (LFMR) response of granular samples is a property largely studied in several compounds [1-3], its origin is still controversially understood. In the celebrated manganites, several works [4, 5] have shown that this response can be understood as arising from a spin-polarized tunneling of carriers across insulating barriers occurring at the interfaces between ceramic grains. It is well established that the barriers located at the grain boundaries strongly affect the resistivity of the samples, but the mechanism by which those barriers give rise to the LFMR is not clear. Experimentally, it has been found that when the resistivity increases the LFMR also does. In the ferromagnetic CrO$_2$ compound, it has been shown [6, 7] that the partial reduction of the grain surface leads to the formation of an insulating Cr$_2$O$_3$ shell that enhances the resistivity and promotes the appearance of a substantial LFMR.

In the case of polycrystalline Sr$_2$FeMoO$_6$ the situation is even more complex and there have been some claims [8] that the LFMR in double perovskites could be mainly related to the existence of anti-site defects. In the present chapter we shall provide evidence that the existence of an insulating barrier SrMoO$_4$ at the grain boundaries of Sr$_2$FeMoO$_6$ plays a fundamental role in determining the LFMR. Also, we will try to

show the relationship between the magnetoresistance and the $SrMoO_4$ impurities, improve our understanding of the LFMR of Sr_2FeMoO_6 in physics and technology.

3.1. Introduction

Recently, there has been a rapidly increasing bulk of research work on double perovskites with the research focused mainly on Sr_2FeMoO_6 at around the Curie temperature of about 420 K [9]. Compared to the perovskite-like manganites, double perovskites have advantages of large low-field room-temperature magnetoresistance (MR) with only little temperature dependence. The transport properties of Sr_2FeMoO_6 are strongly dependent on spin-polarized tunneling through insulating grain boundaries [2], and it is well known that nonmagnetic $SrMoO_4$ impurity is induced to appear at the grain boundaries [10]. Furthermore, the resistivity of Sr_2FeMoO_6 depends sensitively on the preparation conditions such as annealing and film growth parameters, which are presumably due to cation disorder, grain-boundary scattering and/or oxygen content. Both semiconducting and metallic behavior have been observed in Sr_2FeMoO_6 [11-15]. Based on measurements on a single crystal grown by the floating zone method, the stoichiometric compound has a metallic resistivity below the Curie temperature [11]. Semiconductor behavior occurs for the compound prepared by solid-state reactions [9] and sol-gel methods [16]. D. Niebieskikwiat *et al* [10] also presented evidence of a strong influence of environmental conditions on the resistivity. Moreover, the level of the $SrMoO_4$ impurity is intimately correlated to the mixture ratio of the ambient gaseous H_2-Ar stream passing over the material during its high- temperature sintering.

All these characteristics make it possible to control the magnetotransport properties of this compound by modification of its contents of $SrMoO_4$ impurity at different preparation conditions.

Raman scattering has been used to investigate CMR materials [17] and the structures of the polycrystalline Sr_2FeMoO_6 [18]. Therefore, in this chapter, in addition to the current empirical work, a micro-Raman scattering method was also employed to investigate the variation of the content of $SrMoO_4$ impurity in the polycrystalline Sr_2FeMoO_6.

3.2. Experimental

Bulk Sr_2FeMoO_6 samples were prepared by the sol-gel method followed by heat treatment at different temperatures. Briefly, the method consisted of weighing stoichiometric quantities of $(NH_4)_6Mo_7O_{24}\cdot4H_2O$, $Fe(NO_3)_3\cdot9H_2O$ and $Sr(NO_3)_2$, first preparing the chemicals in solution form, and then mixing the solutions of $Sr(NO_3)_2$ and $(NH_4)_6Mo_7O_{24}\cdot4H_2O$ with nitric acid according to the proportion of $\sim$ 10 times moles of $(NH_4)_6Mo_7O_{24}\cdot4H_2O$. The resultant mixture was then mixed with the solution of $Fe(NO_3)_3\cdot9H_2O$ which formed a light green gel after several minutes. The gel was then dried at 60^oC. Subsequently, powder A, B and C were obtained by high-energy ball milling of the gel for 3 hours and powder D was obtained by grinding it in mortar for 3 hours. Then, powders A, B, C and D were preheated at 700^oC for 6 hours, after which powders A, B and C underwent high-energy ball milling for a further 3 hours whereas powder D was conventionally ground for the same duration. Finally, these

powders A, B, C and D were pressed into pellets followed by sintering at 900°C in a steady stream of 5%, 3%, 10% and 5% of H_2 to Ar in the gas mixture for 3 hours, respectively.

During the preparation process, the main difference among samples A, B, and C was that they were sintered in the different mixture ratio of the ambient H_2-Ar gas stream, while the main difference between samples A and D was that two times high energy ball milling were involved in the fabrication process of sample A. The preparation parameters for Sr_2FeMoO_6 samples A, B, C and D are shown in table 3.1.

	A	B	C	D
High energy ball milling	Yes	Yes	Yes	No
H_2/Ar mixture ratio	5%	3%	10%	5%
Synthesis temperature	$900\ ^{o}$C	$900\ ^{o}$C	$900\ ^{o}$C	$900\ ^{o}$C

Table 3.1 Preparation parameters for Sr_2FeMoO_6 samples A, B, C and D, respectively.

The crystal structure and the phase purity of the samples were examined by X-ray diffraction with Cu K_α radiation. The average grain size is calculated using the Scherrer formula $D_{hkl} = k\lambda / B\cos\theta$, where D_{hkl} is grain diameter, k is a constant (shape factor ~ 0.9) [19], B is the width difference of half height of the peaks between the measured sample and the standard of KCl used to calibrate the intrinsic width associated with the equipment, λ is wavelength of the X-ray. All micro-Raman spectra were measured in the backscattering geometry mode using an ISA Jobin-Yvon-Spex

T64000 Raman spectrometer with Olympus microscope attachment. The 514.5 nm line of an argon-ion laser was used as the excitation source. Scanning electron microscopy (SEM; Model XL 30, Philips) was used to study the particle characteristics as well as the fracture surface of sintered ceramic bodies. The electrical resistivity ρ was measured using the standard four-probe technique in the temperature range from 78 to 300K. The magnetoresistivity ratio is defined as $MR = [\rho(H) - \rho(0)]/\rho(0)$, where ρ_H and ρ_0 are respectively the resistivity in an applied magnetic field and in zero field. Magnetic measurements were carried out using a vibrating sample magnetometer.

3.3. Experimental results

3.3.1 Crystal structure and phase analysis

X-ray diffraction patterns of the four samples are shown in Fig. 3.1. The inset shows the expanded section in the range $25^o < 2\theta < 30^o$ containing the strongest peak originating from the SrMoO₄ impurity for samples A and B. Obviously, single phase Sr₂FeMoO₆ can be obtained only within a very small window of oxygen partial pressures [20]. All the XRD peaks of sample A and the peaks of the main phase of Sr₂FeMoO₆ except for the peaks of SrMoO₄ of samples B, C and D can be indexed according to the space group I4/mmm. Since the integrated intensity from a diffraction peak is proportional to the volume fraction of that material in a sample, qualitatively, from the relative intensities ratio of the strongest diffraction peaks of SrMoO₄ phase to that of Sr₂FeMoO₆ phase, we can conclude that there are more amount of SrMoO₄

impurities in samples B, C and D than that of sample A. For sample A, B and C, with increasing proportion of H_2, the $SrMoO_4$ impurity content first decreased, and then increased again. Sample A, which was prepared by high-energy ball milling, is much purer than sample D because the high-energy ball milling yields higher uniformity of the mixed raw compounds, thus providing sufficient reactivity of the mixture during streaming of the 5% H_2/Ar. As a result, very little $SrMoO_4$ impurity was left. The average grain size calculated using the Scherrer equation on the basis of X-ray traces is 45 nm, 40 nm and 20 nm for sample A, B and C, respectively. Although sample A, B and C were prepared at same condition except for the variation of the mixture ratio of the ambient H_2-Ar gas stream surrounding the sample during annealing, the average grain size of samples B and C are smaller than that of sample A, which mainly due to the decomposition process of Sr_2FeMoO_6 is mainly a surface effect and $SrMoO_4$ impurity phase was induced in the grain boundaries region [21], whereby the average grain size of Sr_2FeMoO_6 sample B and C are refined. Similar phenomenon was observed in the ferromagnetic CrO_2 compound, which showed that the partial reduction of the grain surface leads to the formation of an insulating Cr_2O_3 shell [6, 7]. For sample A and D, although the high energy ball milling can refine the grain size of sample A, however, there is large amount of $SrMoO_4$ induced at grain boundaries regions of sample D, which also cause the average grain size of sample D is smaller than that of sample A. The relative content of $SrMoO_4$ and the average grain size of sample A, B, C and D, respectively, are shown in table 3.2.
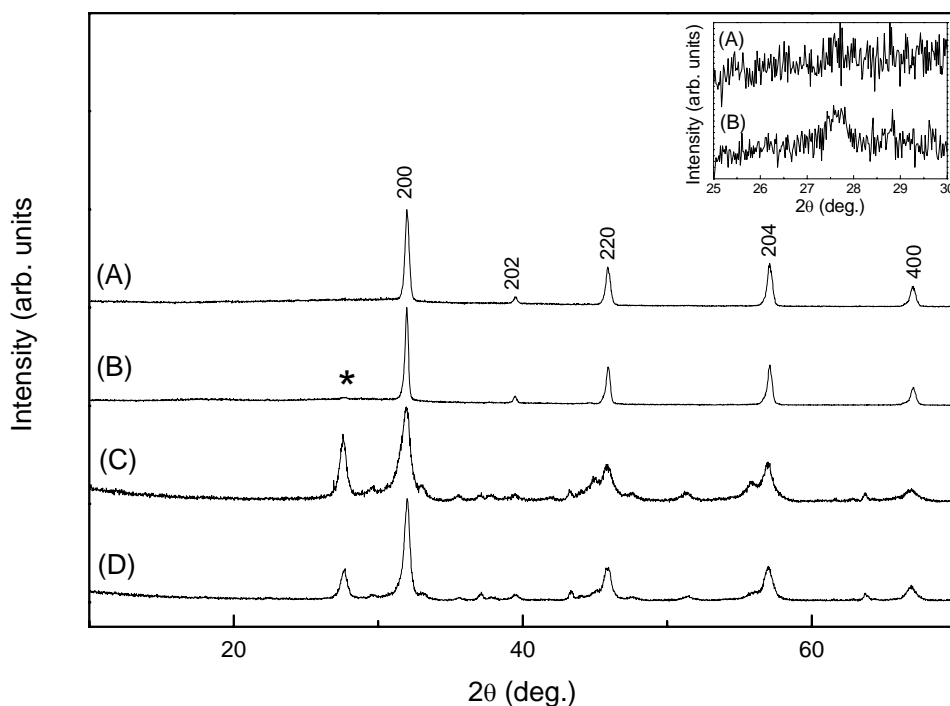
Fig.3.1. X-ray diffraction patterns of polycrystalline Sr_2FeMoO_6 samples A, B, C and D under different preparation conditions. The magnified section in the range $25^o < 2\theta < 30^o$ containing the strongest peaks of the $SrMoO_4$ impurity phase of samples A and B are shown in the inset.

	A	B	C	D
Average grain size	45 nm	40 nm	20 nm	30 nm
Amount of $SrMoO_4$	None	Minor	Most	Much

Table 3.2 Relative content of $SrMoO_4$ and average grain size of samples A, B, C and D, respectively.

Fig.3.2 shows the Raman spectra of samples A, B, C and D at room temperature. The peak at 882.3 cm^{-1}, labeled "*" in Fig.3.2, is the strongest line in the Raman scattering spectrum of the $SrMoO_4$ impurity phase, and it is clear that the amount of $SrMoO_4$ impurity in sample B, C and D are more than that of sample A, which is consistent with the XRD data shown in Fig. 3.1. These results establish conclusively that high-energy ball milling led to the suppression of the $SrMoO_4$ impurity content and the level of the $SrMoO_4$ impurity is intimately correlated to the mixture ratio of the ambient gaseous H_2-Ar stream passing over the material during its high- temperature sintering.
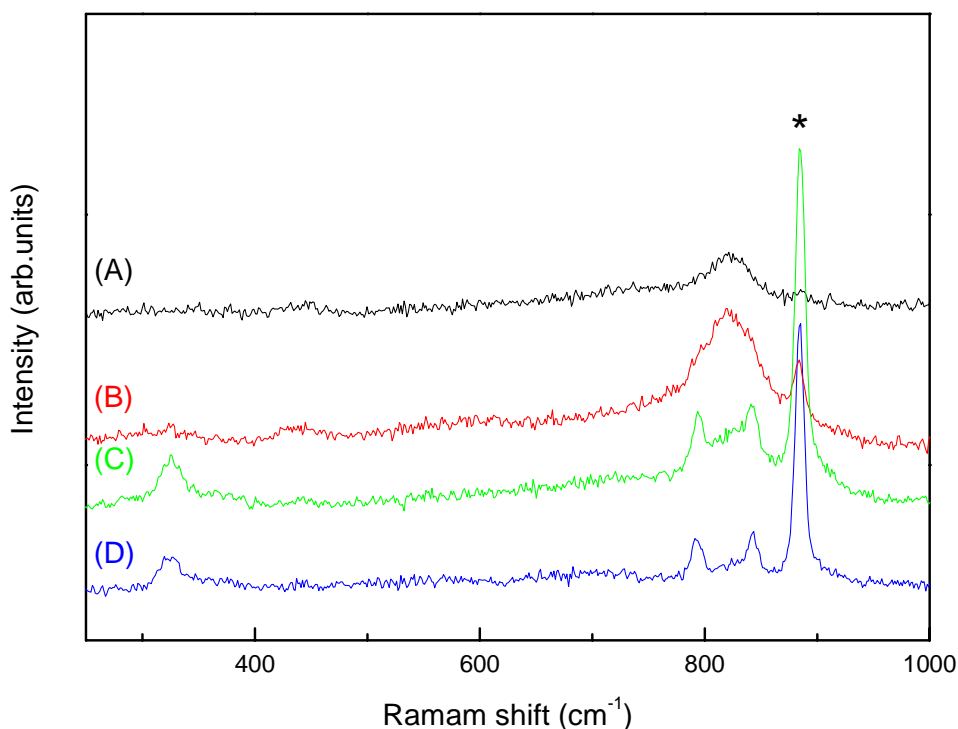
Fig.3.2. Raman spectra of samples A, B, C and D at room temperature, the peak labeled "*" is attributed to $SrMoO_4$.

Figure 3.3 (a) and (b) are SEM micrographs for the Sr_2FeMoO_6 sample A and C. Obviously, the particle surface had become much rougher for sample C, which due to the decomposition process of Sr_2FeMoO_6 is mainly a surface effect and $SrMoO_4$ impurity phase was induced in the grain boundaries region, thus producing a large number of weak-link grain boundaries [22].
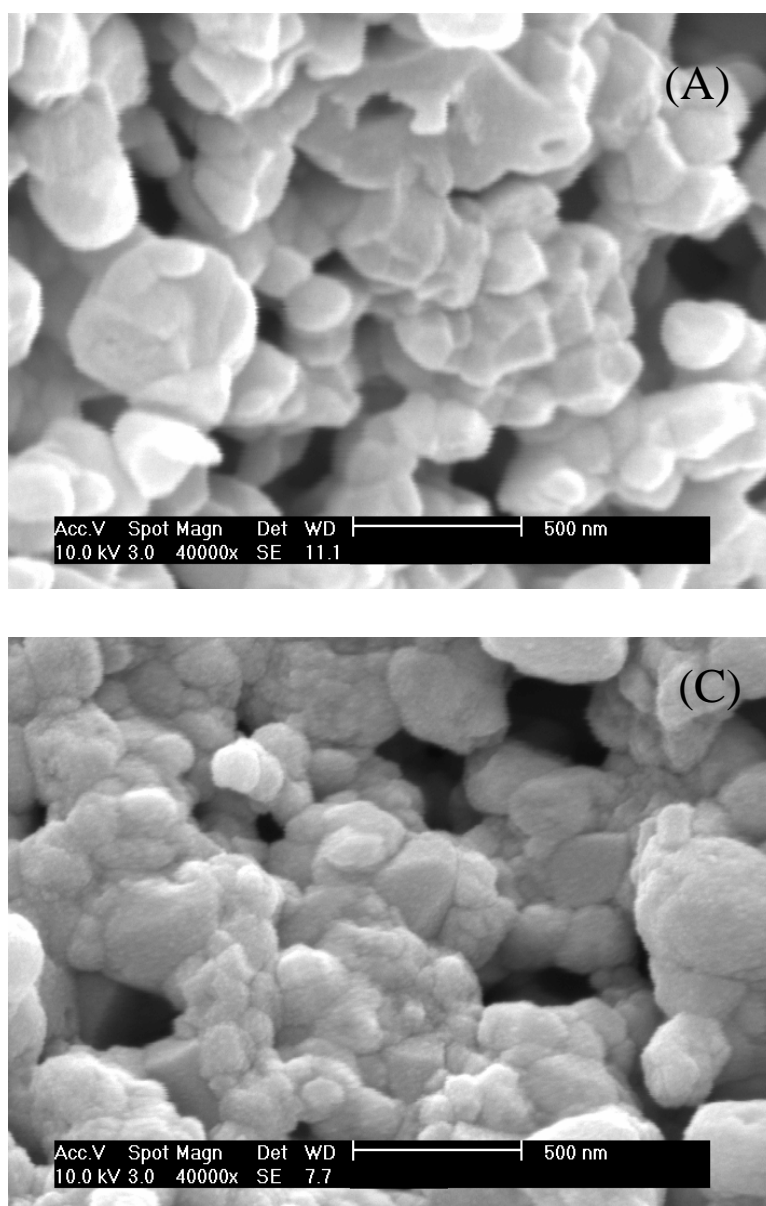
Fig.3.3. SEM micrographs showing the fracture surfaces of samples A and C

3.3.2. Magnetic properties

Magnetic hysteresis loops for Sr$_2$FeMoO$_6$ samples A, B, C and D were measured at 288 K with an applied field up to 3 T, as shown in Fig.3.4. The magnetization value at 3 T for sample A, B, C and D, are 11.4 *emu/g*, 11.2 *emu/g*, 7.0 *emu/g* and 7.4 *emu/g*, respectively. Obviously, with amount of nonmagnetic insulating SrMoO$_4$ increase, the magnetization value of sample decrease, which can be attributed to the stronger disorder effect arising from grain boundaries in the nano-grained sample with more amount of SrMoO$_4$ impurity induced in the grain boundary regions.
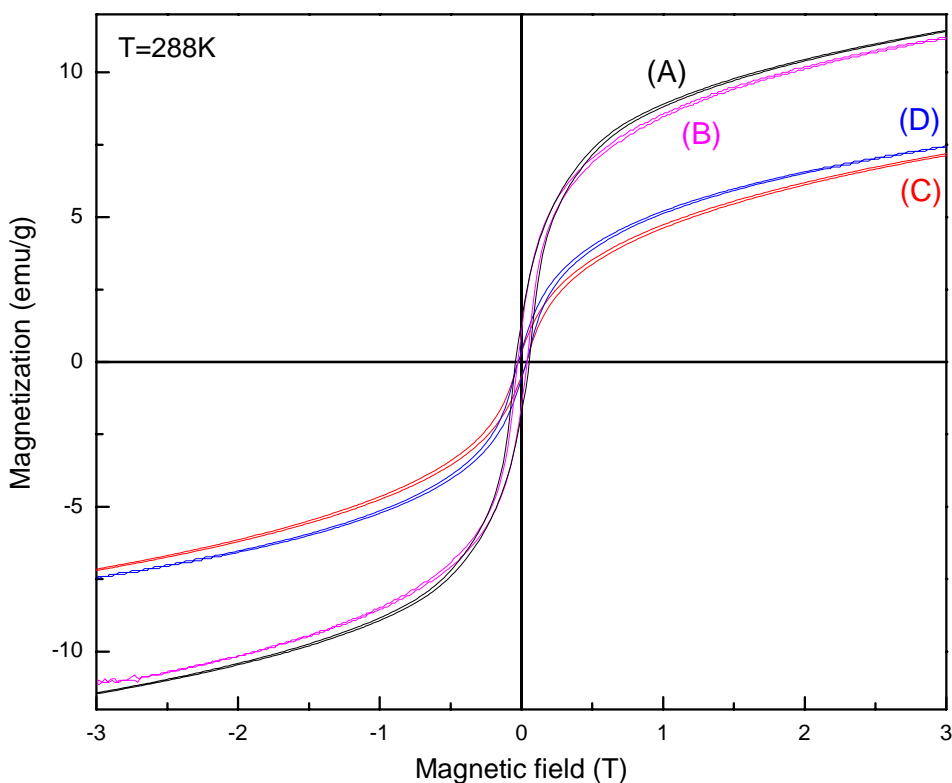
Fig.3.4. Magnetic hysteresis loops of samples A, B, C and D at an applied field up to 3 T at 288 K

3.3.3. Electrical resistivity

Fig.3.5 shows the temperature dependence of the resistivities for the samples A, B, C and D. Samples B, C and D show semiconductor behavior with their resistivities decreasing with temperature over the entire measured temperature range. In contrast, sample A shows metallic behavior over almost the same temperature range. The resistivities of sample A are also smaller than those of samples B, C and D, respectively. These surprising results are found to be correlated to the different $SrMoO_4$ impurity contents. The resistivity depends sensitively on the preparation conditions. In Sr_2FeMoO_6, both semiconducting and metallic behavior has been observed under different preparation condition [23-27]. With proper annealing, Sr_2FeMoO_6 samples can be made insulating, semimetallic, or metallic. Insulating Sr_2FeMoO_6 samples were made metallic [28] and this behavioral change was alternatively explained as possibly due to the improvement of conductivity of the grain-boundary phase or to the homogenization of the composition of the sample [27]. Because the nonmagnetic $SrMoO_4$ impurity is induced to appear at the grain boundaries, and the transport property of the sample is determined by electron tunneling between grains, the higher resistivity and semiconductor behavior of samples B, C and D, and the metal behavior of sample A, can all be ascribed to the prevailing contribution of the grain boundary, which is known to form tunneling barriers for carrier transport. Clearly, the enhanced $SrMoO_4$ impurity level in samples B, C and D enhances the grain boundary effect on their resistivities. Since the resistivity depends sensitively on the preparation conditions, compared with sample D, although there is

less concentration of $SrMoO_4$ in sample B, the resistivity of sample B is still larger than that of sample D, which mainly due to the high-energy ball milling yields higher uniformity of the mixed compound, thus the nonmagnetic $SrMoO_4$ insulator impurity was induced uniformly at the grain boundaries regions, leading to larger resistivity. The restivity at 77 K for sample A, B, C and D, respectively, are also list in table 3.3.
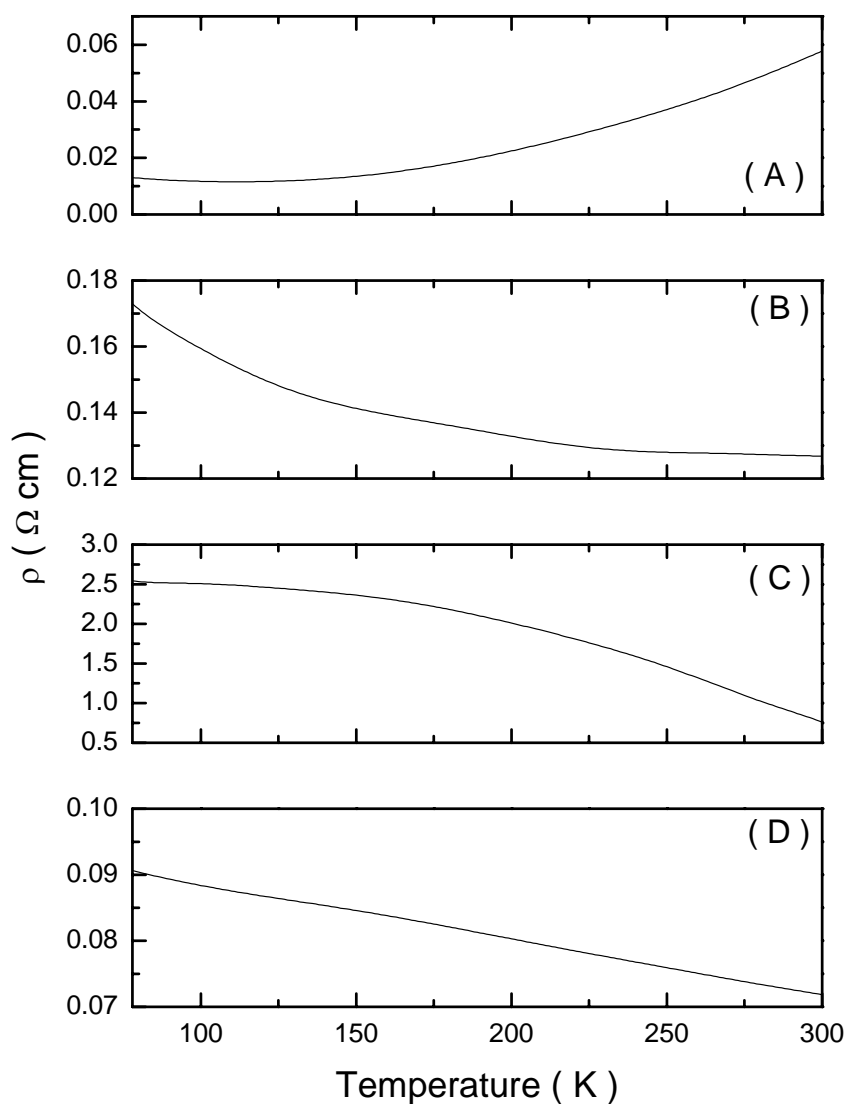
Fig.3.5. Temperature dependence of resistivity for Sr_2FeMoO_6 samples A, B, C and D under different preparation condition

	A	B	C	D
Resistivity at 77 K (Ωcm)	0.013	0.17	2.5	0.09

Table 3.3 Restivity at 77 K for samples A, B, C and D, respectively.

3.3.4. Magnetoresistance

The temperature dependence of the magnetoresistivity ratio $MR(\%) = \Delta\rho / \rho_0 \times 100\%$ ($\Delta\rho = \rho_0 - \rho_H$) for the samples A, B, C and D are shown in Fig.3.6. The Isothermal magnetoresistivity of samples A (solid circles) and D (open circles) at 78 K and 300 K respectively, are also shown in Fig3.7. Obviously, the MR is significantly modified as a result of high-energy ball milling and controlled stream of gaseous H_2-Ar mixtures during annealing. Measurements at a magnetic field show only a small magnetoresistivity effect for the metallic sample A, but a significant magnetoresistive response for the semiconducting sample B and D. This result clearly demonstrates that for samples B and D, the enhancement of the IMR is correlated with the large effective intergrain-tunneling barrier arising from the increased level of the impurity $SrMoO_4$. Although the LFMR in general increases with the $SrMoO_4$ impurity in the sample, further increase of the $SrMoO_4$ impurity as in sample C results in a drop in the LFMR. This is because as the $SrMoO_4$ impurity concentration increases, a point is reached when the boundary thickness becomes comparable or even greater than the spin memory length thereby causing spin-polarized tunneling to become less effective.
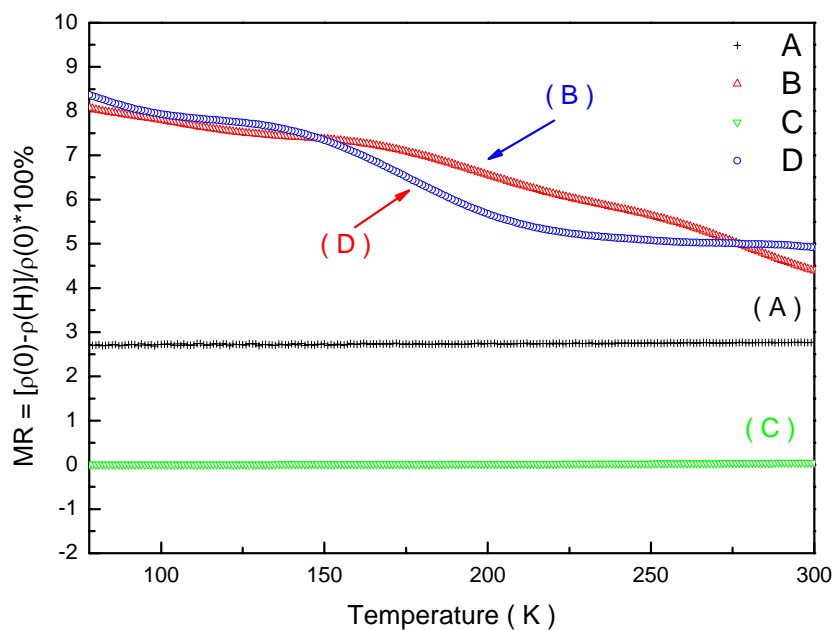
Fig.3.6. Temperature dependence of the magnetoresistivity ratio of sample A (H=1T), B (H=1T), C (H=1T) and D (H=0.4 T).
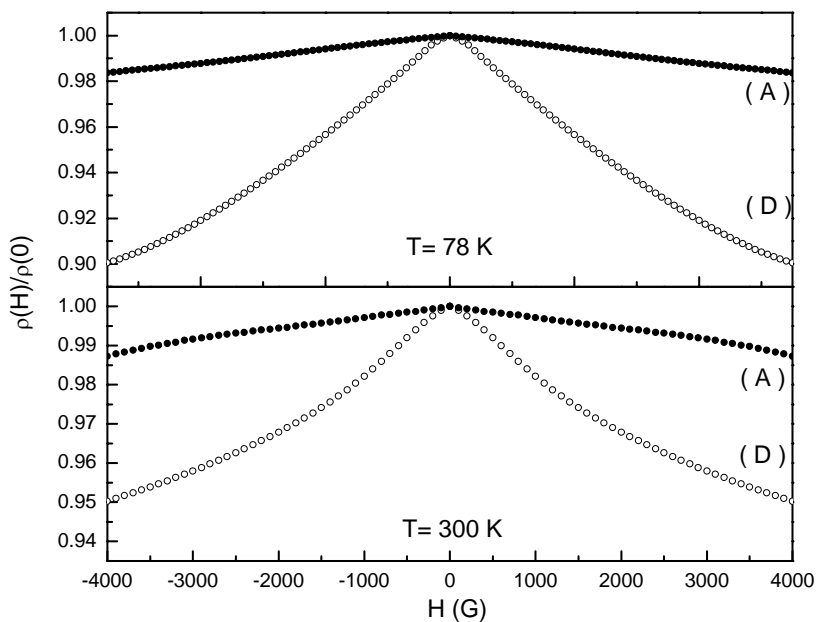
Fig.3.7. Isothermal magnetoresistivity of samples A (solid circles) and D (open circles) at 78 K and 300 K respectively.

3.4. Discussion and conclusions

The magnetic and electric properties of the Sr_2FeMoO_6 compound under different preparation conditions were studied. Depending on preparation condition, we found a strong variation in nonmagnetic $SrMoO_4$ impurity, resulting in metallic or semiconducting behavior of resistivity of the sample. In particular, high-energy ball milling process suppresses the formation of the nonmagnetic $SrMoO_4$ impurity in the grain boundaries region. Also, the mixture ratio of the stream of gaseous H_2-Ar mixture strongly affects the eventual nonmagnetic $SrMoO_4$ impurity level in the annealed material. This $SrMoO_4$ impurity level, in turn, plays a crucial role in determining the low-magnetic-field intergrain tunneling magnetoresistance. The presence of the impurity leads to an enhancement of the intergrain tunneling barrier, with a consequential increase in the resistivity and the low-field magnetoresistance. The magnetic domain reorientation in the polycrystalline Sr_2FeMoO_6 can be controlled by the application of a magnetic field which tends to parallelize the magnetization directions of the ferromagnetic domains. The corresponding reduction in the spin scattering of spin-polarized carriers at the grain boundaries gives rise to a significant decrease of the measured resistivity [9]. When the intergrain barrier diminishes, the itinerant electrons in the surface of each grain become delocalized between the two neighboring grains. This delocalization would be brought about by a reduction in the misalignment between the localized t_{2g} spins located at the surface of the two grains, thus reducing the effective angle θ between the magnetizations of neighboring grains at zero field. The intergrain barrier is diminished resulting in a suppression of the

low-field magnetoresistance [5, 10]. This property opens up the possibility of implementing refined control of the magnetotransport properties of high-temperature half-metallic ferromagnetic materials. Our works also provide a simple method to prepare the single phase Sr$_2$FeMoO$_6$ polycrystals.

If a large magnetoresistivity ratio at high temperatures is required, one may consider increasing the imperfections at the grain boundaries. For example, it will be quite easy to enhance the magnetoresistivity by raising the intergrain barrier layer with a corresponding increase in the SrMoO$_4$ impurity at the grain boundaries, which can in turn be controlled by adjusting the mixture ratio of the ambient H$_2$-Ar stream surrounding the sample during its high-temperature sintering.

In summary, we conclude that the magnetic and electric properties of the Sr$_2$FeMoO$_6$ double perovskite material, its SrMoO$_4$ impurity level, and the preparation conditions are all inter-related, thereby providing us a simple means to control the transport properties by controlling the preparation conditions.

Reference:

[1].   T.H. Kim, M. Uehara, S-W. Cheong, and S. Lee, *Appl. Phys. Lett.* **74**, 1737 (1999)

[2].   Gupta, G.Q. Gong, G. Xiao, P.R. Duncombe, P. Lecoeur, P. Trouilloud, Y.Y. Wang, V.P. Dravid, and J.Z. Sun, *Phys. Rev. B* **54**, R15 629 (1996).

[3].   Ll. Balcells, J. Fontcuberta, B. Martínez, and X. Obradors, *Phys. Rev. B* **58**, R14 697 (1998).

[4].   P. Raychaudhuri, K. Sheshadri, P. Taneja, S. Bandyopadhyay, P. Ayyub, A.K. Nigam, R. Pinto, S. Chaudhary, and S. B. Roy, *Phys. Rev. B* **59**, 13919 (1999);

[5].   H.Y. Hwang, S-W. Cheong, N.P. Ong, and B. Batlogg, *Phys. Rev. Lett.* **77**, 2041 (1996).

[6].   H.Y. Hwang and S-W. Cheong, *Science* **278**, 1607 (1997).

[7].   J. M. D. Coey and Y. Tokura, *Phys. Rev. B* **59**, 11 159 (1999).

[8].   M. García-Hernaíndez, J.L. Martínez, M.J. Martínez-Lope, M.T. Casais, and J.A. Alonso, *Phys. Rev. Lett.* **86**, 2443 (2001).

[9].   K.-I. Kobayashi, T. Kimura, H. Sawada, K. Terakura, and Y. Tokura, *Nature (London)* **395**, 667 (1998)

[10].   D. Niebieskikwiat, A. Caneiro, R. D. Sánchez and J. Fontcuberta, *Phys. Rev. B.* **64** 180406 (2001).

[11].   Tomioka Y, Okuda T, Okimoto Y, Kumai R, Kobayashi K-I and Tokura. *Phys. Rev. B* **61** 422 (2000).

[12].   Westerburg W, Reisinger D and Jakob G, *Phys. Rev. B* **62** R767 (2000).

[13].   Asano, H S. B. Ogale, J. Garrison, A. Orozco, Y. H. Li, E. Li, V. Smolyaninova, C. Galley, M. Downes, M. Rajeswari, R. Ramesh, and T. Venkatesan. *Appl. Phys. Lett.* **74** 3696 (1999).

[14].   Manako T, Izumi M, Konishi Y, Kobayashi K-I, Kawasaki M and Tokura, *Appl. Phys. Lett.* **74** 2215 (1999).

[15].   Chmaissem O, Kruk R, Dabrowski B, Brown D E, Xiong X, Kolesnik S, Jorgensen J D and Kimball CW. *Phys. Rev. B* **62** 14197 (2000).

[16].   C. L. Yuan, S. G. Wang, W. H. Song, T. Yu, J. M. Dai, S. L. Ye, and Y. P. Sun, *Appl. Phys. Lett.* **75**, 3853 (1999).

[17].   V. Dediu, C. Ferdeghini, F. C. Matacotta, P. Nozar, and G. Ruani, *Phys. Rev. Lett.* **84**, 4489 (2000)

[18].   L. Hoang Son , Nguyen Xuan Phuc, Phan Vinh Phuc, Nguyen Minh Hong and Le Van Hong, *J. Raman Spectroscopy.* **10**, 817 (2001).

[19].   H. P. Klug and L. P. Alexander, *X-ray Diffraction Procedures for Polycrystalline and Amorphous Materials*, 2nd ed, (Wiley, New York, 1974), P. 618.

[20].   Tetsur$\bar{o}$ Nakamura, Kenjii Kunihara and Yoshikazu Hirose, *Mat. Res. Bull.* **16**, 321 (1981).

[21].   J. Navarro, C. Frontera, D. Rubi, N. Mestres, J. Fontcuberta, *Mat. Res. Bull.* **38**, 1477 (2003).

[22].   X. L. Wang, S. X. Dou, H. K. Liu, M. Lonescu, B. Zeimetz, *Appl. Phys. Lett.* **73**, 396 (1998).

[23]. Y. Tomioka, T. Okuda, Y. Okimoto, R. Kumai, K-I. Kobayashi and Y. Tokura, *Phys. Rev. B.* **61,** 422 (2000)

[24]. W. Westerburg, D. Reisinger and G. Jakob, *Phys. Rev. B* **62,** R767 (2000)

[25]. H. Asano *et al*, *Appl. Phys. Lett.* **74,** 3696 (1999)

[26]. T. Manako, M. Izumi, Y. Konishi, K-I. Kobayashi, M. Kawasaki and Y. Tokura, *Appl. Phys. Lett.* **74** 2215 1999

[27]. O. Chmaissem, R. Kruk, B. Dabrowski, D. E. Brown, X. Xiong, S. Kolesnik, J. D. Jorgensen and C. W. Kimball, *Phys. Rev. B* **62,** 14197 (2000)

[28]. M. Itoh, I. Ohta and Y. Inaguma, *Mater. Sci. Eng.*, B **41**, 55 (1996)

Chapter 4

Temperature dependence of resistivity of $Sr_2CoMoO_{6-\delta}$ films

In the last chapter, we have demonstrated that the $SrMoO_4$ impurity content plays a key role in modifying the low magnetic field intergrain tunneling magnetoresistance of the Sr_2FeMoO_6 sample, thus the low field magnetoresistance will be enhanced when the insulating nonmagnetic $SrMoO_4$ impurity close to the conduction threshold at the grain boundary region. Recently, research works found that manganites are intrinsically inhomogeneous [1-8]. In other words, the states formed in these compounds are dominated by coexisting clusters of competing phases. These phases are typically ferromagnetic and antiferromagnetic. These inhomogeneties are thought the case of the unusually large magnetoresistance found in manganites. In order to enhance our understanding on the low field magnetoresistance mechanism of double perovskites, we also investigated such mixed-phase phenomenology in the ordered double-perovskite structured materials. Since the substitution of Fe site with Co ions leads to an antiferromagnet, it provides a good platform for our investigation of this interesting mixed-phase phenomenology.

In this chapter, we investigate the temperature dependence of the resistivity and magnetoresistance of a polycrystalline $Sr_2CoMoO_{6-\delta}$ film deposited on (100)-$SrTiO_3$ substrate prepared by the pulsed laser deposition method. X-ray diffraction, Raman and magnetoresistance results demonstrate clearly the coexistence of a ferromagnetic metallic and an antiferromagnetic (or paramagnetic) insulating domain. Percolative transition between these two phases as the temperature varies, which is believed to

induce a metal-insulator transition at around T_C, has been directly observed in our measurements of the temperature dependence of the sample resistivity. Thus we have provided new direct evidence that a phase separation scenario also exists in the ordered double-perovskite structures materials.

4.1. Introduction

Since the observation of most significant colossal magnetoresistance (CMR) effect close to the magnetic transition temperatures, there has been an intense search for compounds with magnetic transition temperatures substantially higher than the T_C (~ 200-350 K) in manganites [9-11]. Recently, it has been reported that the transition-metal oxides with the ordered double-perovskite structure, A_2MMoO_6, (where A is a rare-earth metal and M a transition metal), exhibits a pronounced negative CMR at lower magnetic fields and higher temperatures compared to the doped manganites [12-15]. The reason for this improved MR property in these compounds at a relatively higher temperature arises primarily from the fact that they have a surprisingly high magnetic transition temperature (Sr_2FeMoO_6 ~ 415 K [12]; Sr_2CoMoO_6 ~ 350 K [15]) compared to manganites. The largest MR response is expected close to the magnetic transition temperature T_C. The combination of a large MR effect and a high T_C value makes this family of perovskites promising for practical applications.

Up to the present, many researchers have reported the structural, magnetic, and electrical properties of the double-perovskite transition-metal oxides, especially the Fe-based compounds. To the best of our knowledge, however, the behavior of resistivity at high temperatures especially near T_C is less addressed and the temperature dependence of the grain-boundary resistivity is not very well understood [16]. In this work we investigate the temperature dependence of the resistivity and

magnetoresistance of a polycrystalline $Sr_2CoMoO_{6-\delta}$ film, especially its resistivity behavior at high temperatures.

Experimental and theoretical investigations [1-8] suggest that due to the tendencies toward phase separation, the ground state of manganite models will not be a homogeneous state, but an inhomogeneous one, typically involving both ferromagnetic (FM) metallic and antiferromagnetic (AFM) charge and orbital ordered insulating domains [8]. The strong tendencies of phase mixing originate from (1) phase separation between different-density phases arising from specific electronic structures, and (2) disorder-induced phase separation with percolative characteristics between equal-density phases driven by disorder near first-order metal-insulator transitions. It is also argued[16] that the interesting mixed-phase tendencies and percolation should be present in a large variety of other compounds as well. In this paper we report the finding of actual evidence of percolative mixed-phase characteristics in the temperature dependence of the resistivity of the polycrystalline $Sr_2CoMoO_{6-\delta}$ films appearing as a metal-insulator transition peak in the resistivity-temperature curve.

4.2. Experimental

The oxygen-stoichiometric Sr_2CoMoO_6 perovskite was prepared as a black polycrystalline powder from citrate precursors obtained by soft chemistry procedures. Stoichiometric amounts of analytical grade $Sr(NO_3)_2$, $Co(NO_3)_2 \cdot 6H_2O$, and $(NH_4)_6Mo_7O_{24} \cdot 4H_2O$ were dissolved in citric acid. The citrate + nitrate solutions were slowly evaporated, leading to organic resins containing a random distribution of the involved cations at an atomic level. These resins were first dried at 120 ^{o}C and then slowly decomposed at temperatures up to 500 ^{o}C. All the organic materials and nitrates were eliminated in a subsequent treatment at 700 ^{o}C in air, for 6 h. This treatment gave

rise to highly reactive precursor materials. Finally, the powder was pressed into pellets followed by sintering at 900 ^{o}C in the ambience of a controlled stream of various proportions of gaseous H_2-Ar mixtures for 3 hours. The resulting test samples obtained by sintering in air, a stream of 3%, 5%, 5%, 8%, 10%, 12%, 15%, 18% and 20% of H_2 to Ar in the gas mixture, respectively. From X-ray diffraction patterns of these samples shown in Fig. 4.1, we can see that with increased proportion of H_2 to Ar in the ambience of a stream of gaseous H_2-Ar mixtures during annealing, the $SrMoO_3$ impurity content decreased. The mixture ratio of the stream of gaseous H_2-Ar mixture strongly affects the eventual nonmagnetic $SrMoO_3$ impurity level in the annealed material. It can also be seen from Fig. 4.1 that if we further increase the proportion of H_2 to Ar in the ambience of a stream of gaseous H_2-Ar mixtures during annealing, the amount of nonmagnetic $SrMoO_3$ will further decrease. However, because of safety and the limitation of our facilities, 20% of the H_2 proportion is the limitation that we can afford. Therefore, in this chapter, we select the sample sintered in the ambience of a stream of 20% of H_2 to Ar in the gas mixture as our target.
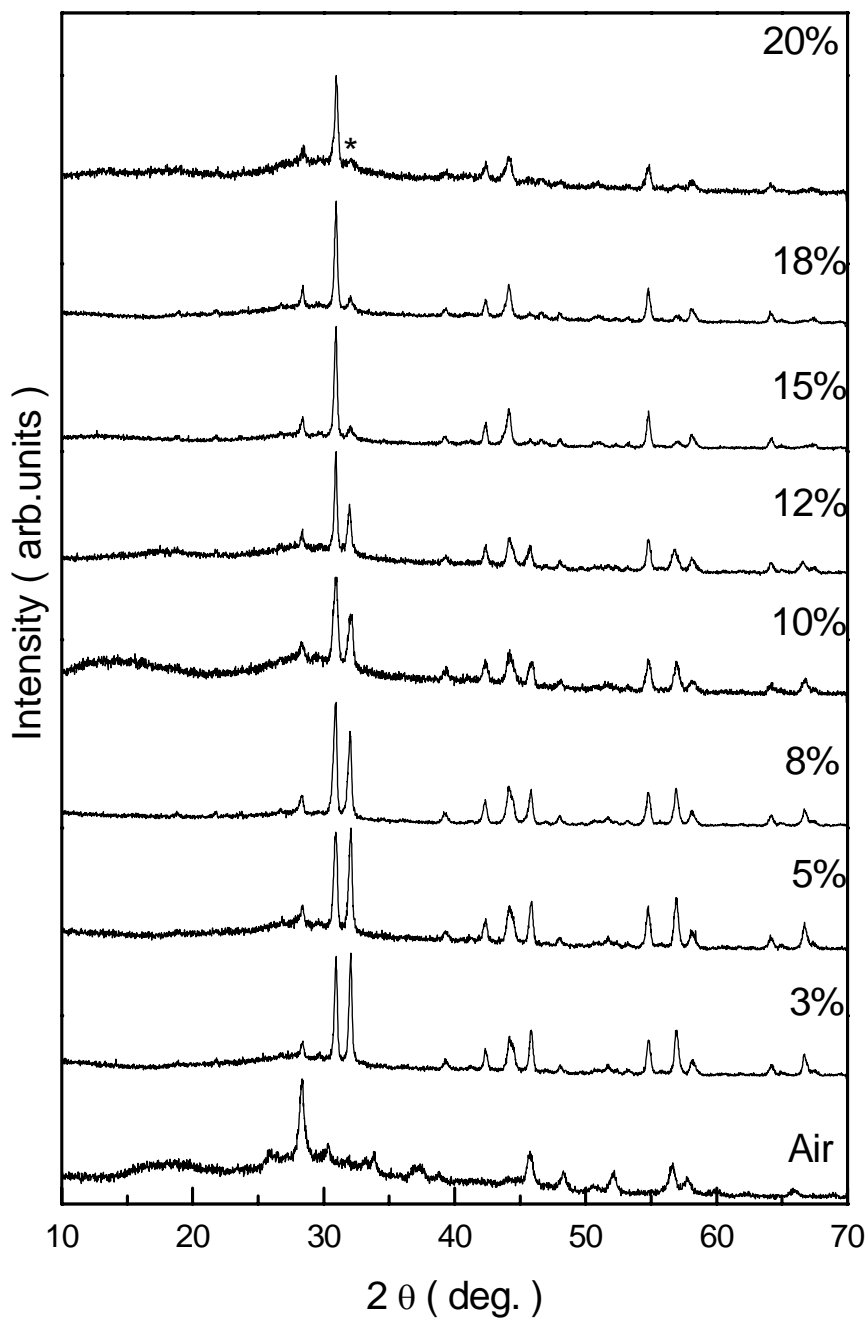
Fig.4.1. X-ray diffraction patterns of polycrystalline Sr_2CoMoO_6 samples prepared under different H_2-Ar mixture ambience. The strongest peaks of the $SrMoO_3$ impurity phase is indicated by "*".

A thin film of $Sr_2CoMoO_{6-\delta}$ thickness 700 nm was deposited on (100) $SrTiO_3$ (STO) substrate by pulsed laser deposition. The substrate temperature during deposition was kept at 500 ^oC in high vacuum (10^{-7} Torr). The crystal structure and phase purity of the samples were examined by X-ray diffraction using Cu K_α radiation. The micro-Raman spectrum was measured in the backscattering geometry using an ISA Jobin-Yvon-Spex T64000 Raman spectrometer with an Olympus microscope attachment. The 514.5 nm line of an argon-ion laser was used as the excitation source. The electrical resistivity ρ was measured using the standard four-probe technique. The magnetoresistivity ratio, MR, is defined as $MR(\%) = \Delta\rho / \rho_0 \times 100\%$ where $\Delta\rho = \rho_0 - \rho_H$, and ρ_H and ρ_0 are respectively the resistivities in an applied magnetic field and in zero field.

4.3. Results and discussion

Fig. 4.2 depicts the X-ray diffraction pattern for the deposited $Sr_2CoMoO_{6-\delta}$ thin films on STO at room temperature. It shows that the film was polycrystalline, and a minor amount of $SrMoO_3$ was also detected. The peak, labelled "*", corresponds to the peak of the $SrMoO_3$ impurity phase. All the other peaks corresponding to the main phase of $Sr_2CoMoO_{6-\delta}$ can be indexed according to the space group I4/mmm.

Fig. 4.3 shows the Raman spectra of the sample at room temperature in air. The peak at 882.3 cm^{-1}, labelled "*", corresponds to the strongest Raman line of the $SrMoO_4$ impurity phase, which mainly due to that $SrMoO_3$ was unstable at high temperature caused by the laser spot of Raman spectrometer in air, leading to $SrMoO_4$ because of the oxidation process. The presence of the $SrMoO_4$ impurity in the sample reinforces the conclusion obtained in the XRD analysis in Fig. 4.2.
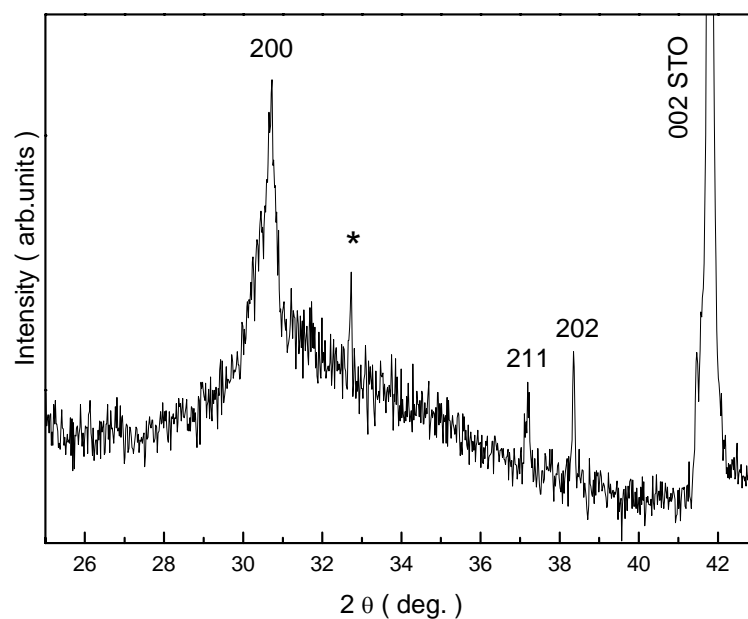
Fig.4.2. X-ray diffraction patterns of polycrystalline $Sr_2CoMoO_{6-\delta}$ thin film. The peak pertaining to the impurity $SrMoO_3$ is indicated by "*".
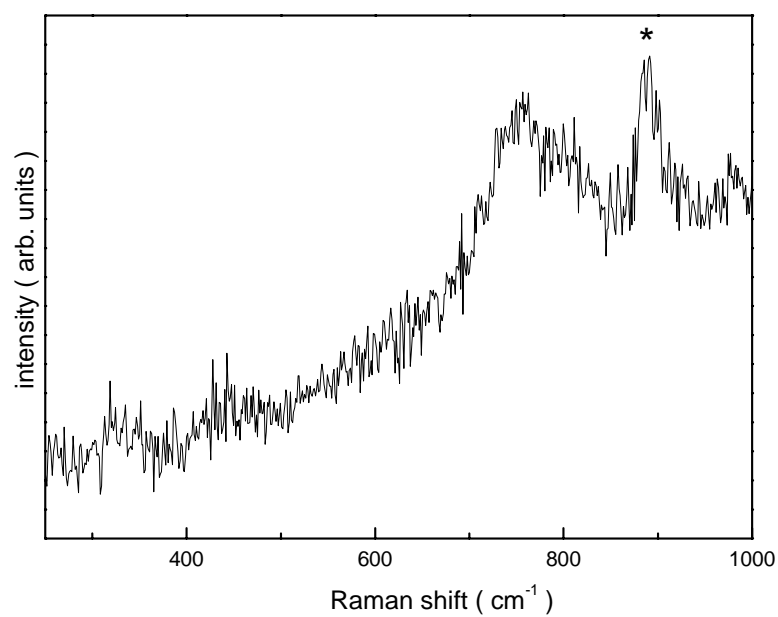
Fig.4.3. Raman spectra of polycrystalline $Sr_2CoMoO_{6-\delta}$ thin film at room temperature. The peak pertaining to the impurity $SrMoO_4$ is indicated by "*".

Fig. 4.4 shows the temperature dependence of the resistivities at zero field and at 1T respectively for the sample in the temperature range from 80-300K. At the lower temperature range, the resistivity decreases exponentially with temperature, showing a semiconductor-like or thermally activated behavior. The temperature dependence of the magnetoresistivity ratio $MR(\%) = \Delta\rho / \rho_0 \times 100\%$ ($\Delta\rho = \rho_0 - \rho_H$) at 1T is presented in the insert of fig 4.3. The magnetoresistance (MR) decays as the temperature increases, comparable to that found in the other double perovskite Sr_2FeMoO_6 [12]. The MR is dominated by the grain boundary tunneling at temperatures well below T_C. The increasing value of MR as the temperature is lowered is attributed to the weak spin thermal fluctuation at low temperatures.
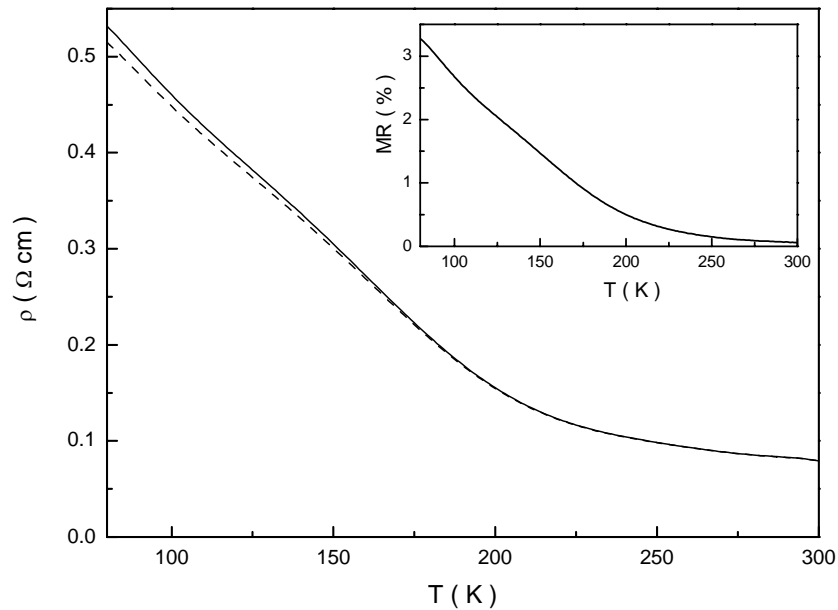
Fig.4.4. Temperature dependence of resistivity for polycrystalline $Sr_2CoMoO_{6-\delta}$ thin film at zero field (solid line) and at 1T (dash line) in the temperature range from 80 to 300 K. The insert represents the corresponding temperature dependence of the magnetoresistivity ratio $MR(\%) = (\rho_0 - \rho_H) / \rho_0 \times 100\%$ at H=1T in the same temperature range.

Fig. 4.5 shows the temperature dependence of the resistivity of the $Sr_2CoMoO_{6-\delta}$ film kept in vacuum (10^{-6} Torr) in the extended temperature range from 80 to 500 K. The arrow indicates the Curie temperature (T_C) as determined by Viola et al [15]. At very low temperatures Sr_2CoMoO_6 is known to behave as a paramagnetic insulator [15,17], which may be ascribed to the absence of the $4d$ electrons in the hexavalent $Mo^{6+}(4d^0)$ ions and the divalent nature of the Co ions [18]. Magnetic measurements suggest the presence of ferromagnetic domains characterized by T_C embedded in the antiferromagnetic matrix (AFM) characterized by Néel temperature (T_N) [15]. Contrary to the Sr_2FeMoO_6 structure, the formation of ferromagnetic clusters is not due to the double exchange mechanism [19] but rather to a kind of super-exchange interactions between the Co^{2+} and Mo^{5+} moments. Based on a consideration of the small number of itinerant electrons introduced from the oxygen vacancies, Mo^{5+} cations should be randomly isolated and so only isolated ferromagnetic clusters can be formed [15]. Therefore $Sr_2CoMoO_{6-\delta}$ can be viewed as a canted-spin system or one containing inhomogeneous ferromagnetic clusters embedded in a paramagnetic matrix (or AFM matrix if the temperature is below T_N). At low temperatures the resistivity exhibits a semiconductor-like or thermally activated behavior. The resistivity of the $Sr_2CoMoO_{6-\delta}$ film is about two orders of magnitude smaller than that of the bulk Sr_2CoMoO_6, implying that a higher density of charge carriers (electrons) is involved in the conduction process. However, this resistivity is still too high compared to that in a metallic state. This indicates that the resistivity of the sample arises from carrier scattering at the ferromagnetic grain boundaries [12]. This observation is supported by the inverse temperature dependence of the measured MR shown in the insert of Fig. 4.4.
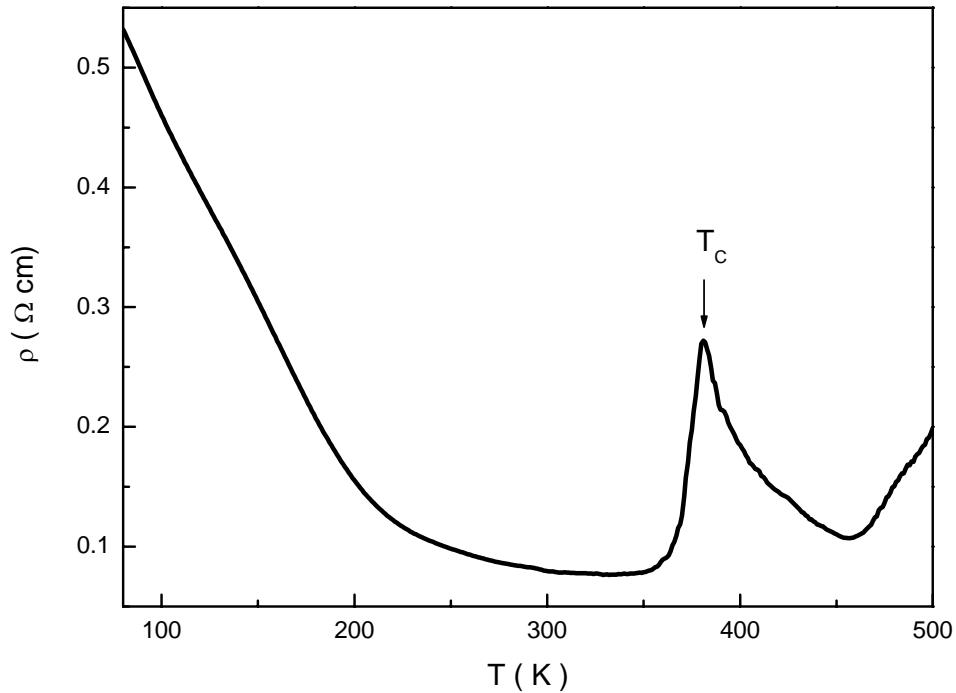
Fig.4.5. Temperature dependence of resistivity for polycrystalline $Sr_2CoMoO_{6-\delta}$ thin film in the extended temperature range from 80 to 500 K.

A conspicuous change in the resistivity ρ is observed at around T_C. In the low-temperature ($T<T_C$) ferromagnetic phase, a metallic behavior (i.e. ρ increases with T) is observed, while a semiconductor behavior is observed in the paramagnetic phase ($T>T_C$). The semiconducting behavior at T above T_C could be due to the thermal spin fluctuation of the ferromagnetic domains and the randomness of the boundary scattering. With further increase in temperature significantly beyond T_C, the resistivity shows a linear increase, which may be ascribed to the enhanced phonon scattering of the carriers and other localization effects.

The temperature dependence of the resistivity of $Sr_2CoMoO_{6-\delta}$ can be well explained from the phase separation scenario involving percolative transport through the ferromagnetic clusters in a background AFM matrix [1-3, 8]. Starting from a

regime where the ferromagnetic clusters are formed dynamically (spin fluctuation) at a high temperature T^* above T_C, the metallic state can be achieved if the temperature is decreased and the size of clusters grows gradually until eventually percolative transport through the ferromagnetic domains becomes possible. At this temperature, the carriers can move over a long distance and the metallic state is reached [1-3, 8]. Alternatively, one can imagine the metallic fraction p to drop with increasing temperature, which is a reasonable assumption since the metallic portion of the sample originates in the ferromagnetic (FM) arrangement of spins that improves conduction. Such a spin arrangement deteriorates as the temperature increases. Moreover it is reasonable to imagine that the size of the FM clusters decrease as the temperature grows. Then, a pattern of FM clusters that erstwhile had been connected at low temperatures (leading to a metallic behavior) may become disconnected at higher temperatures. The direct observation of the metal-insulator transition peak appearing in our temperature dependence of the sample resistivity represents evidence of the onset of percolative transition, and hence the existence of the phase separation scenario in the $Sr_2CoMoO_{6-\delta}$ film. The decrease in the metallic portion with increasing temperature was confirmed by a recent theoretical investigation on the random field Ising model [7] based on the random resistor network model [20]. However, quantitative determination of the T^* at which the ferromagnetic clusters are formed is difficult and needs further investigation. The phase diagram of $Sr_2CoMoO_{6-\delta}$ film was also included in Fig.4.6 to conclude our findings and arguments.
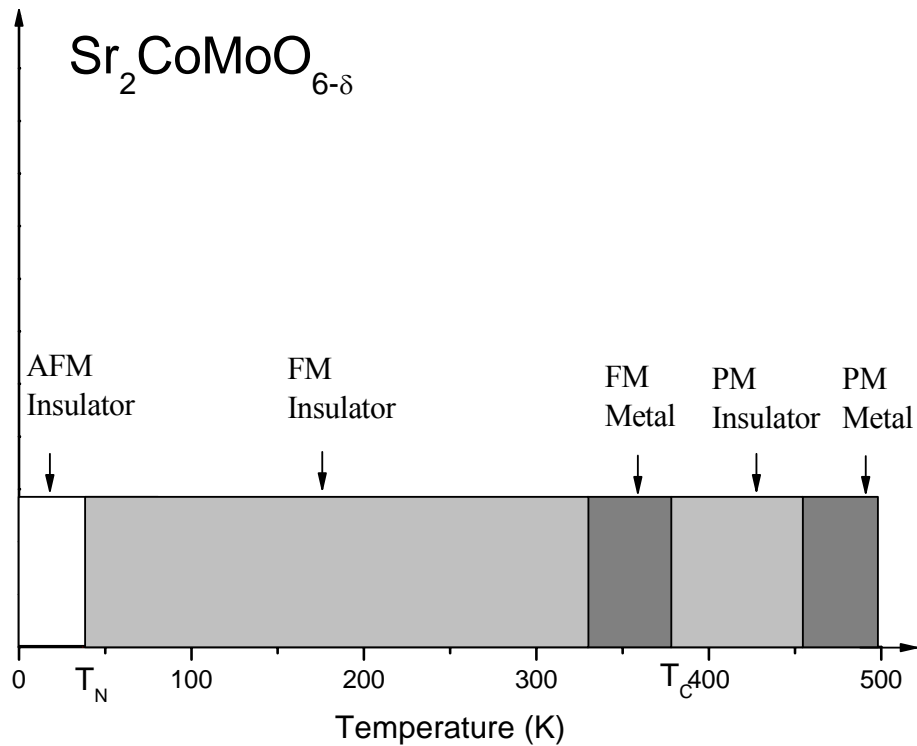
Fig.4.6. Phase diagram of $Sr_2CoMoO_{6-\delta}$

4.4 conclusions

In summary, a polycrystalline $Sr_2CoMoO_{6-\delta}$ film was fabricated on STO and the behavior of its resistivity at high temperatures, especially around T_C, has been investigated. The sample can be viewed as a typical mixed-phase system with ferromagnetic metallic clusters embedded in the AFM insulating matrix. With increasing temperature, its magnetoresistance decreases until the room temperature. At higher temperatures, the sample resistivity exhibits a metal-insulator transition peak near T_C, which is attributed to the percolative transition between the FM metallic and AFM insulating phases. It provides the experimental evidence that the phase separation scenario also exists in the transition-metal oxides with the ordered double-perovskite structure.

References:

[1].   M. Uehara, S. Mori, C. H. Chen and S. -W. Cheong, *Nature* **399**, 560 (1999).

[2].   M. Fath, S. Freisem, A. A. Menovsky, Y. Tomioka, J. Aarts, and J. A. Mydosh, *Science* **285**, 540 (1999).

[3].   Mereo, S. Yunoki, and E. Dagotto, *Science* **283**, 2034(1999).

[4].   Mereo, M. Mayr, A. Feiguin, S. Yunoki, E. Dagotto, *Phys. Rev. Lett.* **84**, 5568 (2000).

[5].   G. Varelogiannis, *Phys. Rev. Lett.* **85**, 4172 (2000).

[6].   T. Hotta, Y. Takada, H. Koizumi, E. Dagotto, *Phys. Rev. Lett.* **84**, 2477 (2000).

[7].   M. Mayr, A. Moreo, J. Vergs, J. Arispe, A. Feiguin, E. Dagotto, *Phys. Rev. Lett.* **86**, 135 (2001)

[8].   Elbio Dagotto, Takashi hotta, Adriana Moreo, *Phys. Reports* **344**, 1-153 (2001)

[9].   R. von Helmolt, J. Wecker, B. Holzapfel, L. Schultz, and K. Samwer, *Phys. Rev. Lett.* **71**, 2331 (1993).

[10].   J. J. Neumeier, M. F. Hundley, J. D. Thompson, and R. H. Heffner, *Phys. Rev. B* **52**, R7006 (1995).

[11].   P. Schiffer, A. P. Ramirez, W. Bao, and S-W. Cheong, *Phys. Rev. Lett.* **75**, 3336 (1995).

[12].   K. I. Kobayashi, T. Kimura, H. Sawada, K. Terakura, and Y. Tokura, *Nature (London)*. **395**, 667 (1998).

[13].   R. P. Borges, R. M. Thomas, C. Cullinan, J. M. D. Coey, R. Suryanarayanan, L. Ben-Dor, L. Pinsard-Gaudart, A. Revcolevschi, *J. Phys.: Condens. Matter* **11**, L445 (1999).

[14].   K.-I. Kobayashi, T. Kimura, H. Sawada, K. Terakura, and Y. Tokura, *Phys. Rev. B.* **59**, 11159 (1999).

[15]. M. C. Viola, M. J. Martnez-Lope, J. A. Alonso, P. Velasco, J. L. Martnez, J. C. Pedregosa, R. E. Carbonio, and M. T. Fernndez-Daz, *Chem. Mater.* **14**, 812, (2002).

[16]. D. Niebieskikwiat, R. D. Snchez A. Caneiro, L. Morales, M. Vsquez-Mansilla, F. Rivadulla, and L. E. Hueso, *Phys. Rev. B.* **62**, 3340 (2000).

[17]. M. Itoh, I. Ohota, and Y. Inaguma, *Mater. Sci. Eng. B*, **41**, 55 (1996).

[18]. W. Sleight and J. F. Weiher, *J. Phys. Chem. Solids* **33**, 679 (1972).

[19]. Y. Moritomo, Sh. Xu, A. Machida, T. Akimoto, E. Nishibori, M. Takata, and M. Sakata, *Phys. Rev. B.* **61** 7827(R) (2000).

[20]. S. Kirkpatrick, *Rev. Mod. Phys.* **45**, 574 (1973).

Chapter 5

Effect of Cu doping on the magnetoresistive behavior of

double perovskite Sr$_2$FeMoO$_6$ polycrystals

In the last two chapters, we have demonstrated that the SrMoO$_4$ impurity content plays a key role in modifying the low magnetic field intergrain tunneling magnetoresistance of the Sr$_2$FeMoO$_6$ sample and provided the experimental evidence that the phase separation scenario also exists in transition-metal oxides with the ordered double-perovskite structure. Although most studies suggest that the grain boundaries are responsible for the low-field MR in Sr$_2$FeMoO$_6$, there are also reports suggesting that the low-field MR is connected to the cationic disorder in double perovskites. García-Hernández *et al.* [1] observed that the magnitude of the low-field MR decreases linearly as the disorder increases. On the other hand, Navarro *et al.* [2] claim that the MR increases with an increase in antisite disorder. In their studies, the polycrystalline Sr$_2$FeMoO$_6$ samples having higher-antisite disorder showed larger MR than those with less disorder. The different observations and explanations reported in the literature indicate that the precise mechanism responsible for the MR in Sr$_2$FeMoO$_6$ is still a controversial issue. Therefore, in this chapter, the effect of B site order on the magnetoresistance will be investigated.

The electrical, magnetic, and transport properties of Cu-doped polycrystalline samples Sr$_2$Fe$_{1-x}$Cu$_x$MoO$_6$ with ordered double perovskite structure were investigated systematically in this chapter. Analysis of the X-ray powder diffraction pattern based on the Rietveld analysis indicates that the substitution of Fe^{3+} ions by Cu^{2+} ions

enhances the site location order of Fe, Cu and Mo on the B-site for the high-doping-level samples (x=0.20, 0.25, 0.30). With increasing doping level, a transition from semiconductor to metal behavior was also found to occur. Furthermore, the transition temperature was found to decrease either by the application of a magnetic field or by increasing the doping level. It can be concluded that the existence of Cu^{2+} ions induces the occurrence of $Fe^{3+\delta}$ ions and the double exchange (DE) interaction in $Fe^{3+} - O - Mo - O - Fe^{3+\delta}$. The transport mechanism in these samples can be attributed to the competition between the metal phase and the semiconductor phase arising from the doping of Cu^{2+} ions. Both the semiconductor-to-metal transition and the magnetoresistive behavior can be explained by the percolation threshold model.

5.1. Introduction

Recently, much interest has been focused on the magnetotransport properties of the ordered double perovskite $A_2B'B''O_6$ (such as Sr_2FeMoO_6) and related half-metallic ferromagnets (or ferrimagnets), in which low field spin-polarized intergrain tunneling magnetoresistance (IMR) and a high degree of spin polarization of Fermi-level electrons were observed [3, 4]. Compared to the perovskite-like manganites, this kind of materials has advantages of large low-field room-temperature magnetoresistance (MR), little temperature dependence of MR and high Curie temperature. Therefore, today, there are lots of reports about the electrical, magnetic, and transport properties of the polycrystalline bulks, epitaxial films and single crystalline materials of Sr_2FeMoO_6 and Sr_2FeReO_6 [5-8]. However, little study has been made on atomic substitution at the B-site. We have synthesized the polycrystalline ordered double perovskite Sr_2FeMoO_6 bulk samples with grain size in the range of 29-45nm using a sol-gel method [9]. (*The average grain size is calculated*

using the Scherrer formula $\mathrm{D_{hkl}} = \mathrm{k}\lambda / B\cos\theta$*, where D$_{hkl}$ is grain diameter, k is a constant (shape factor ~ 0.9) [10], B is the width difference of half height of the peaks between the measured sample and the standard of KCl used to calibrate the intrinsic width associated with the equipment, λ is wavelength of the X-ray.*) However, growth of such double perovskites, in bulk-sintered, single-crystalline, or epitaxial thin-film form, would necessarily lead to a certain degree of mis-site disorder on the octahedral cation (B', B'') sublattices [3, 11]. For instance, in their work on sintered Sr$_2$FeMoO$_6$, Kobayashi *et al.* [3] found that 13% of the Fe and Mo ions were not located on their respective sublattices. More recently, Asano *et al.* [6] found that the magnetotransport properties of Sr$_2$FeMoO$_6$ thin films grown under different conditions differ dramatically, so much so that even the sign of magnetoresistance could be changed. They speculated that the probable cause of their observation was due to mis-site disorder or partial phase segregation. The larger the difference in the sizes of the B' and B'' atoms or the sizes and charges of the B' and B'' ions, the greater was the chance that the compounds would have an order structure [12]. Because the difference between the radii of Cu^{2+} ion and Mo^{5+} ion is larger than that between Fe^{3+} and Mo^{5+} ions, the substitution of Fe^{3+} ions by Cu^{2+} ions may facilitate the formation of the ordered structure. In this paper we report the effect of Cu-doping on the electrical, magnetic, and transport properties of nanometer-scale polycrystalline samples of Sr$_2$Fe$_{1-x}$Cu$_x$MoO$_6$ with the ordered double perovskite structure.

5.2. Experimental

Bulk $Sr_2Fe_{1-x}Cu_xMoO_6$ samples (with x = 0, 0.10, 0.15, 0.20, 0.25, and 0.30) were prepared by the sol-gel method [9] followed by heat treatment at different temperatures. Briefly, the method consisted of weighing stoichiometric quantities of $(NH_4)_6Mo_7O_{24}\cdot4H_2O$, $Fe(NO_3)_3\cdot9H_2O$, $Cu(NO_3)_2\cdot3H_2O$, $Sr(NO_3)_2$, preparing them in solution form, and mixing the solutions of $Sr(NO_3)_2$, $Cu(NO_3)_2\cdot3H_2O$ and $(NH_4)_6Mo_7O_{24}\cdot4H_2O$ with nitric acid according to the proportion of ~10 times in moles of $(NH_4)_6Mo_7O_{24}\cdot4H_2O$. The resultant mixture was then mixed with the solution of $Fe(NO_3)_3\cdot9H_2O$ to form a light green gel after several minutes. The gel was dried at 60 ^oC, and then preheated at 400 ^oC and at 700 ^oC for 6 h each, respectively. Finally, the powder was finely pulverized and pressed into pellets followed by sintering at 900 ^oC in a stream of 5% H_2/Ar for 3 h. In this chapter, in order to show that the substitution of Fe^{3+} ions by Cu^{2+} ions may facilitate the formation of the ordered structure, there is no high energy ball milling involved in the sample fabrication process.

The crystal structure and the phase purity of the samples were examined by X-ray diffraction with Cu K_α radiation. The electrical resistivity ρ was measured using the standard four-probe technique in the temperature range from 40 to 300 K, obtained by using cryogenic refrigeration equipment, in applied magnetic fields of up to 10 kG. The ac susceptibility was measured by means of a sensitive mutual-inductance method at a frequency of 1 kHz and in a low field of 0.15G in the temperature range from 80 to 430 K [13]. The MR ratio here is defined as $MR = [\Delta\rho / \rho(0)] = [\rho(H) - \rho(0)] / \rho(0)$, where ρ_H and ρ_0 are respectively the resistance in an applied magnetic field and in zero field.

5.3. Results and Discussion

The XRD patterns of the synthesized samples at room temperature are shown in Fig.5.1. It shows that the undoped sample of Sr_2FeMoO_6 has a small amount of $SrMoO_4$ impurity phase, in accordance with previous reports [3, 9 and 14]. The analysis of crystal site order is based on the standard Rietveld technique [15] from which the structural parameters are computed. All XRD peaks of the main phase of these samples (x=0.10, 0.15, 0.20, 0.25, and 0.30) except for the peaks of $SrMoO_4$ can be indexed according to the combination of an orthorhombically distorted perovskite structure with the space group I4/mmm and a structure phase with space group Pbnm. All XRD peaks of the main phase of Sr_2FeMoO_6 except for the peaks of $SrMoO_4$, however, can be indexed according to the space group I4/mmm. The larger the difference in the sizes of the B' and B'' atoms or the sizes and charges of the B' and B'' ions the greater was the chance that the compounds would have an ordered structure [15]. Because the difference between the radii of Cu^{2+} ion and Mo^{5+} ions is larger than that between Fe^{2+} and Mo^{5+} ions, the substitution of Fe^{3+} ions by Cu^{2+} ions facilitate the formation of the ordered structure. The structure with space group Pbnm occurs owing to the difference in radii of Fe^{3+} and Cu^{2+}. Analysis of the X-ray powder diffraction pattern in terms of the Rietveld analysis indicates an order value of 76% for the Fe, Cu and Mo on the B-site for the sample with x=0. As x increases from 0.10 to 0.15 the B-site ordering degree drops from 75% to 73%, but with further increase of x it increases again to 81% at x=0.20 and 93% at x=0.30. The full Rietveld refinements of XRD data for (A) Sr_2FeMoO_6; (B)$Sr_2Fe_{0.9}Cu_{0.1}MoO_6$; (C) $Sr_2Fe_{0.8}Cu_{0.2}MoO_6$; (D) $Sr_2Fe_{0.7}Cu_{0.3}MoO_6$ are shown in Fig.5.2. The drop in B-site ordering for the low doping level samples (x=0.10 and 0.15) can be attributed to parts of the Cu^{2+} ions not occupying the B-site, thereby forming stray scattering centers. This result agrees well

with our resistivity results presented below.
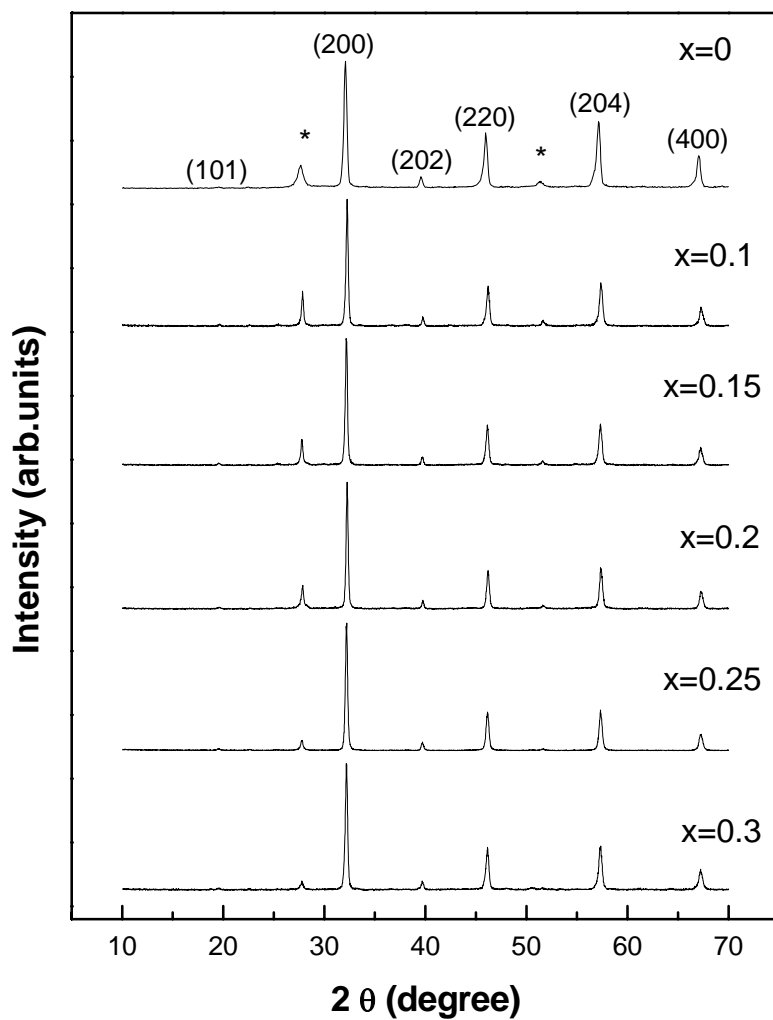
Fig.5.1. X-ray pattern of polycrystalline $Sr_2Fe_{1-x}Cu_xMoO_6$ (x =0, 0.10, 0.15, 0.20, 0.25, and 0.30) samples. The second phase ($SrMoO_4$) peaks are noted by *.
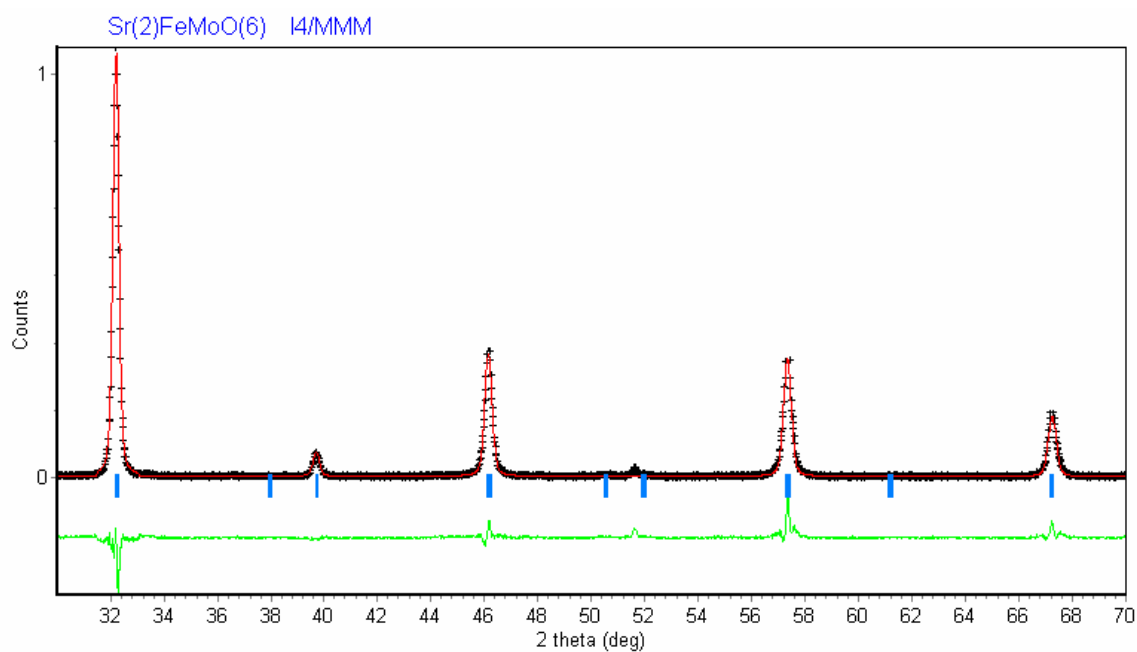
(A) Sr_2FeMoO_6
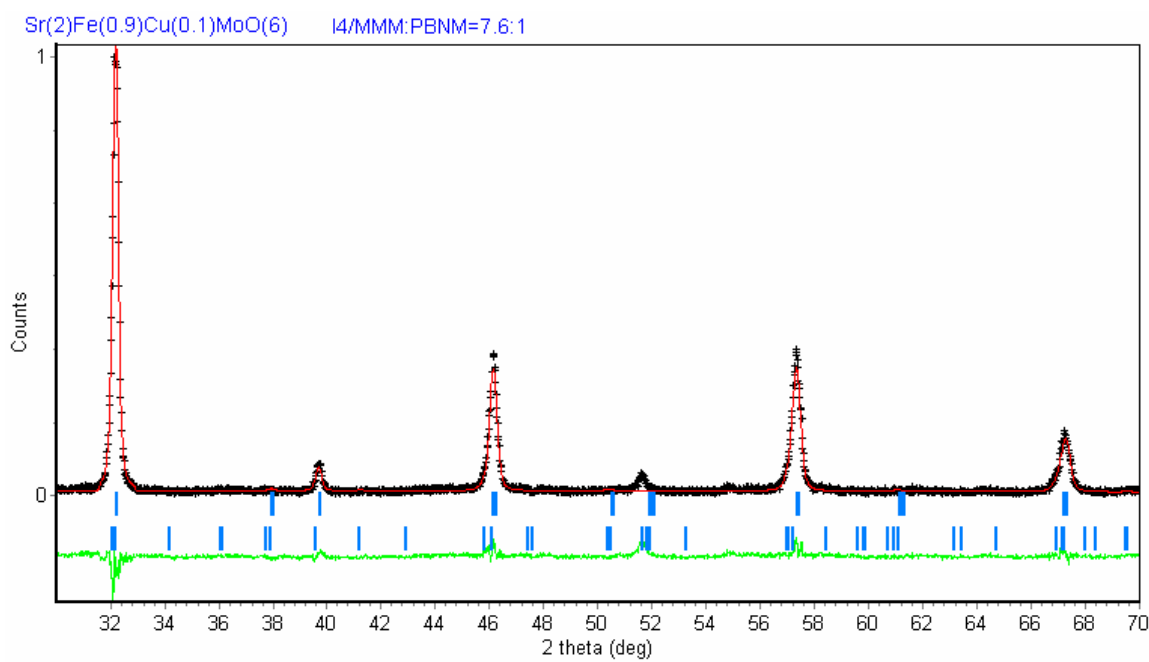
(B) $Sr_2Fe_{0.9}Cu_{0.1}MoO_6$
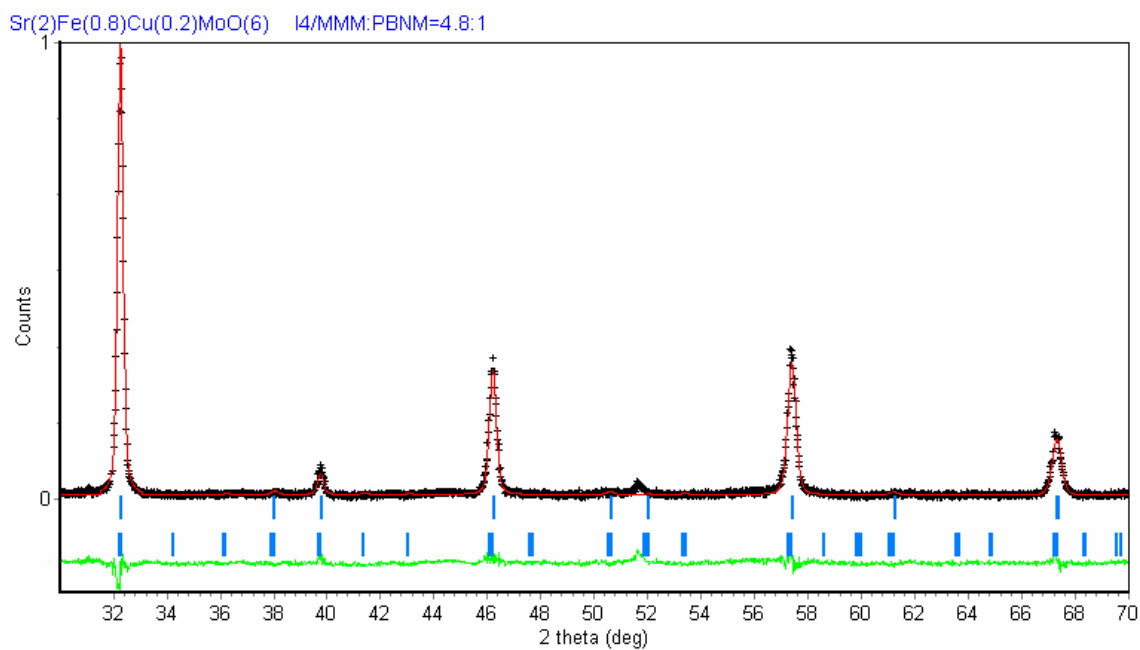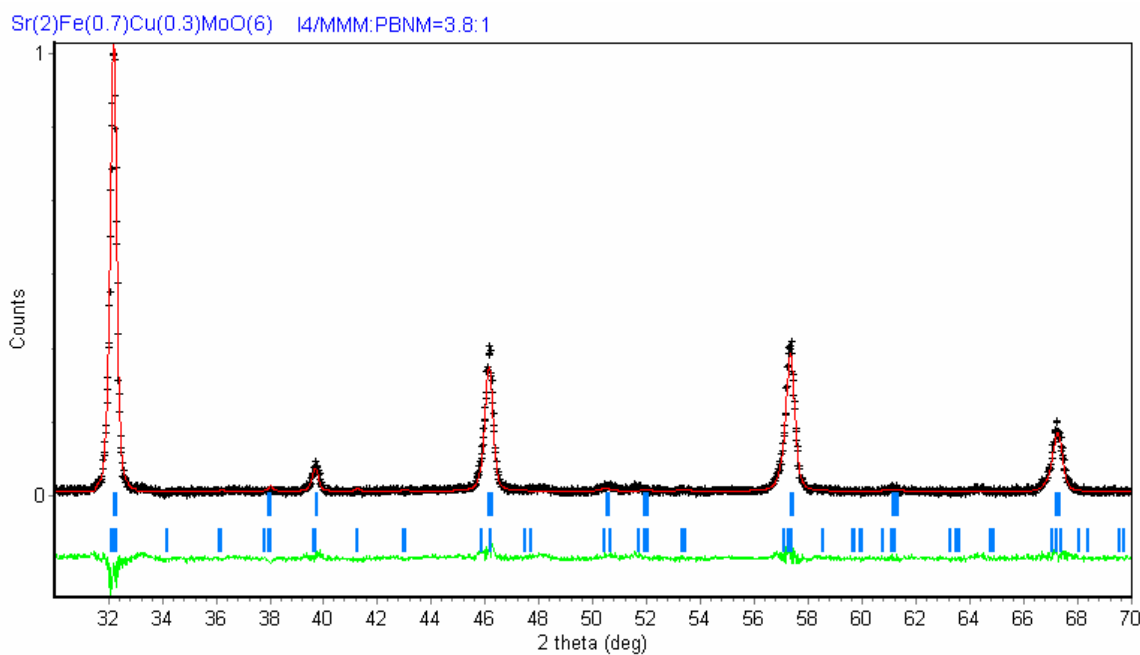
(C) Sr$_2$Fe$_{0.8}$Cu$_{0.2}$MoO$_6$

(D) Sr$_2$Fe$_{0.7}$Cu$_{0.3}$MoO$_6$

Fig.5.2 Rietveld refinement of XRD data for (A) Sr$_2$FeMoO$_6$; (B)Sr$_2$Fe$_{0.9}$Cu$_{0.1}$MoO$_6$; (C) Sr$_2$Fe$_{0.8}$Cu$_{0.2}$MoO$_6$; (D) Sr$_2$Fe$_{0.7}$Cu$_{0.3}$MoO$_6$. Calculated (full line), experimental (+), and difference (bottom) profiles are shown.

Fig.5.3(a) and (b) show the temperature dependence of the resistivity of samples in zero fields and in an applied magnetic field of 4 kG for the two low doping levels (x = 0.10, 0.15), and for high doping levels (x = 0.20, 0.25, 0.30), respectively. The resistivity curves for the undoped sample (x=0) is also included in Fig.5.3 (a) for comparison. For samples with low doping levels, the resistivity decreases as the temperature increases. The sample with higher x has a higher resistivity. The low-doping-level samples exhibit semiconductor behavior over the entire measured temperature range from 40 to 300 K. Their resistivities are larger than those of the undoped Sr_2FeMoO_6 polycrystalline samples with crystalline grains of about a nanometer scale (about 10^{-1} Ωcm) [9]. For the high-doping-level samples, their resistivities are generally much smaller than those of the low-doping-level samples. More interestingly, for each sample, the resistivity decreases with increasing temperature until a minimum resistivity is reached after which it increases as the temperature further increases. This temperature represents the semiconductor-to-metal transition temperature, T_{SM}. All the high-doping-level samples exhibit semiconductor behaviour at temperatures below T_{SM} and metal behavior above T_{SM}. Furthermore, T_{SM} is found to decrease with increasing x, and/or applied magnetic field strength.
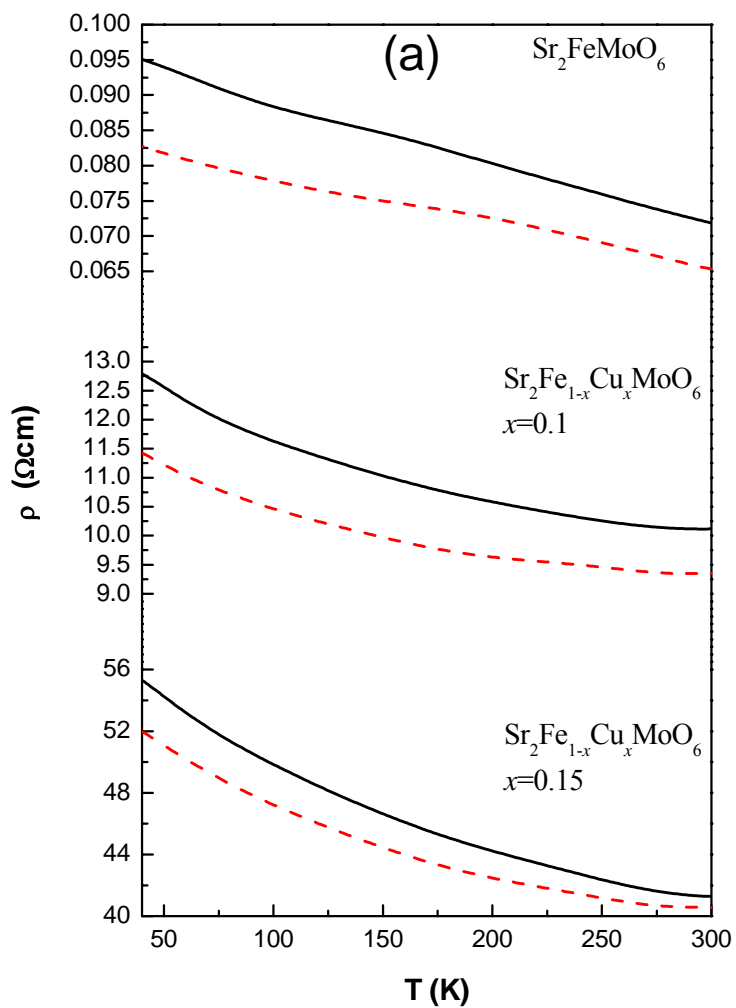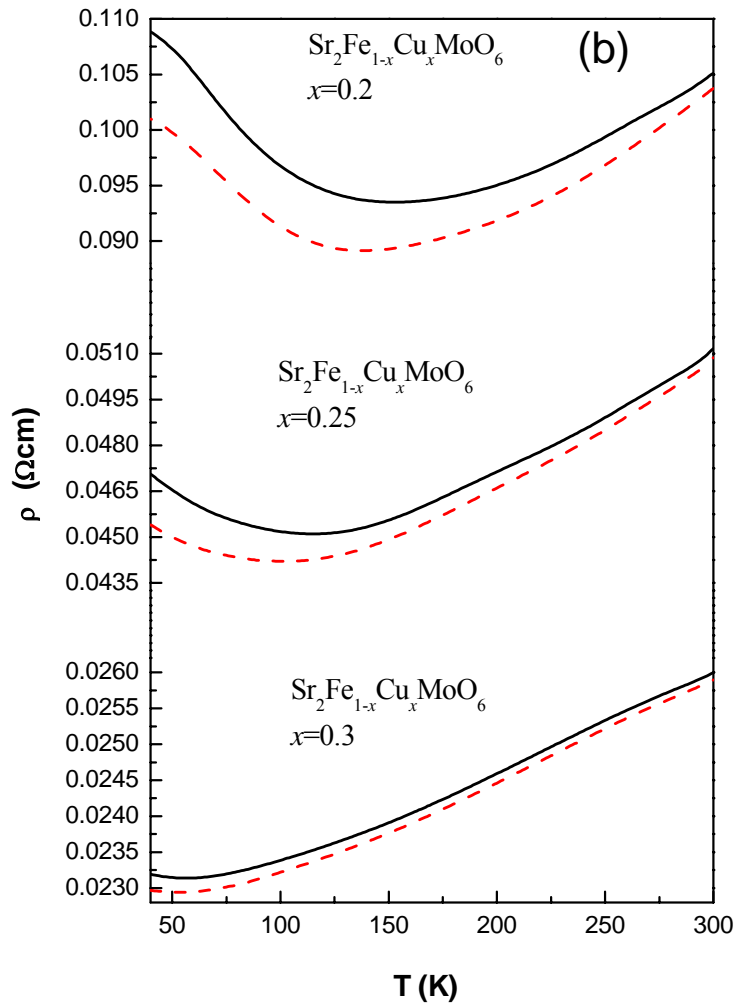
Fig.5.3. Temperature dependence of resistivity of polycrystalline $Sr_2Fe_{1-x}Cu_xMoO_6$ (x =0, 0.10, 0.15, 0.20, 0.25, 0.30) samples in zero field (solid line) and 4 kG (dash line). (a) x=0, 0.10, 0.15; (b) x=0.2, 0.25, 0.30.

Fig.5.4 shows the temperature dependence of the magnetoresistance (MR) ratio $MR(\%) = (\rho_0 - \rho_H)/\rho_0 \times 100\%$ in the same magnetic field of 4 kG for all samples with their respective doping levels. The MR (T) functions for all the samples have a similar trend; they decrease slowly with increasing temperature and doping level (except for an anomalous curve crossover between x=0.15 and x=0.20). This behavior is remarkably different from that observed in polycrystalline manganese oxides with perovskite structure [13].
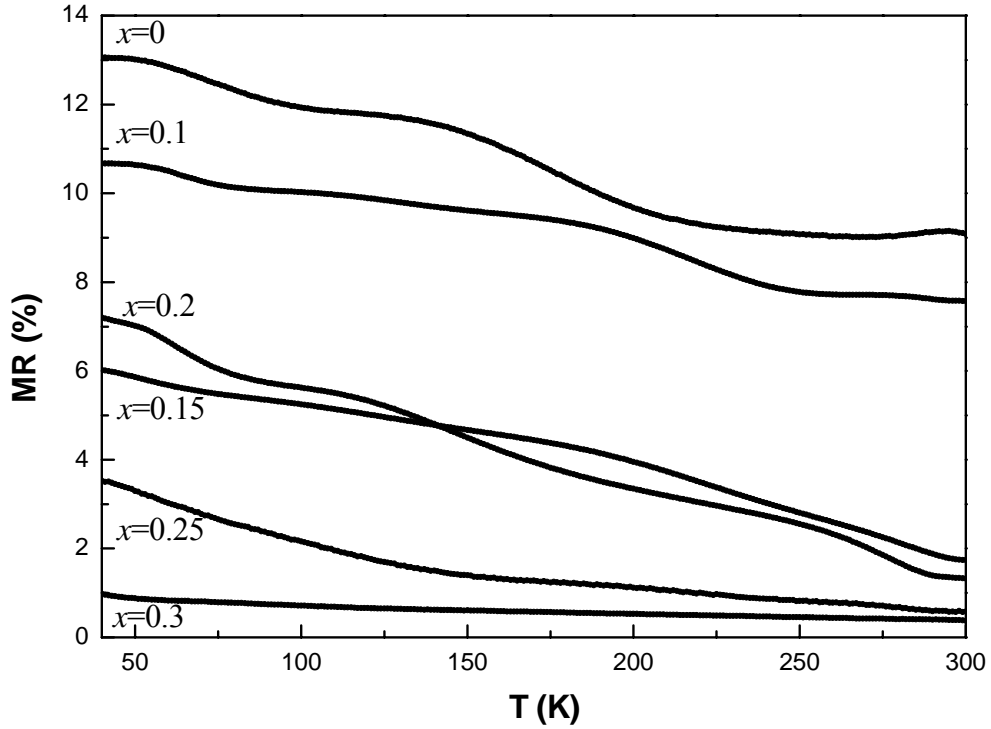
Fig.5.4.   Temperature   dependence   of   magnetoresistivity   ratio $MR(\%) = (\rho_0 - \rho_H)/\rho_0 \times 100\%$ for polycrystalline $Sr_2Fe_{1-x}Cu_xMoO_6$ (x =0, 0.10, 0.15, 0.20, 0.25, 0.30) samples at 4kG.

Fig.5.5 shows the temperature dependence of the ac susceptibility χ [Fig.5.5a] and its differential $d\chi/dT$ [Fig.5.5b] for all samples. The critical temperature at which $\left|d\chi/dT\right|$ is a maximum is defined as the magnetic transition temperature T_C. From Fig.5.5 we can see that there is only one magnetic transition temperature T_C for the undoped sample (x=0), whereas for the Cu-doped samples there are two magnetic transition temperatures (T_{C1}, T_{C2}). The higher magnetic transition temperature T_{C1} corresponds to the structure with space group I4/mmm, and the lower T_{C2} corresponds to that with space group Pbnm. As x increases from 0 to 0.30, T_{C1} increases from 402 to 417 K, while T_{C2} increases from 346 to 399 K as x increases from 0.10 to 0.30. These results are well in agreement with our XRD data.
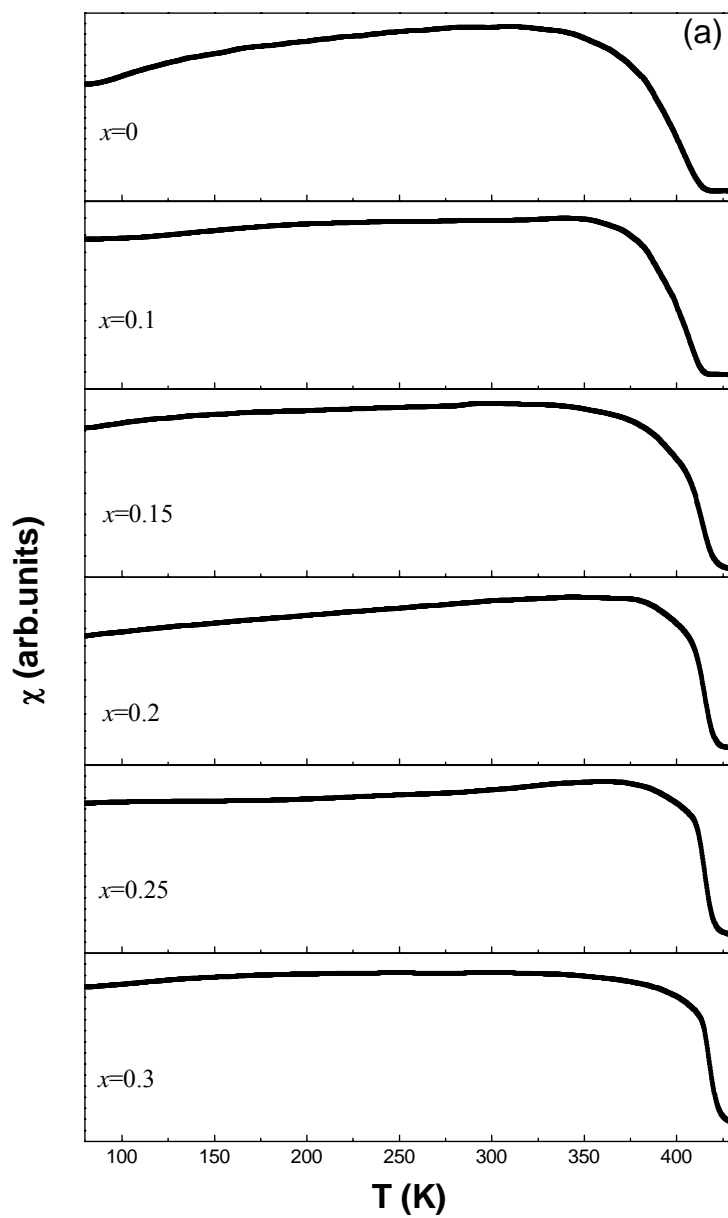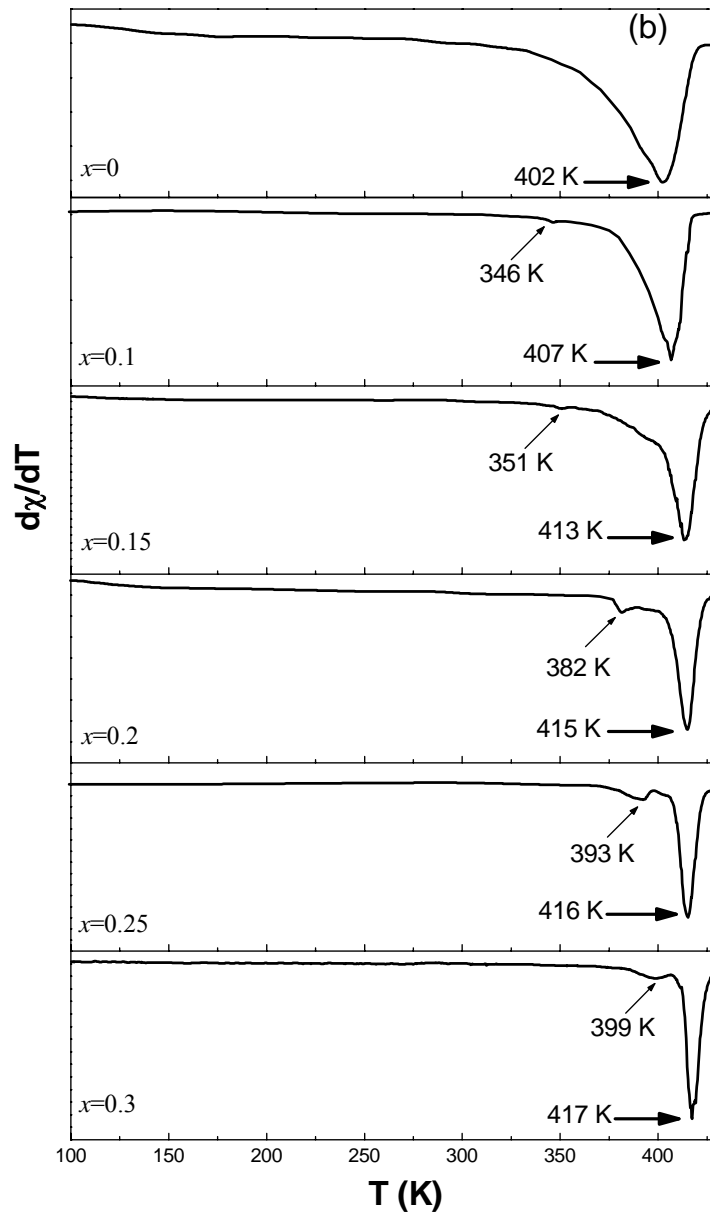
Fig.5.5. Temperature dependence of low-field ac susceptibility χ [Fig.5.5 (a)] and its differential $d\chi/dT$ [Fig.5.5 (b)], of polycrystalline $Sr_2Fe_{1-x}Cu_xMoO_6$ (x =0, 0.10, 0.15, 0.20, 0.25, and 0.30) samples.

We can now show that Cu^{2+} ions should occupy the Fe-sites. Firstly, if Cu were to occupy the Mo site, then, according to our stoichiometric proportions used, it would cause more mis-site disorder, leading to a decrease in both the saturation magnetization and the T_C of our samples [11], which is contrary to our experimental

observation that the Curie temperature T_C increases with doping level *x*. Secondly, we can infer that the substitution of Fe^{3+} ions by Cu^{2+} ions induces some $Fe^{3+\delta}$ ions. If this were not so, then some Mo^{5+} ions would be turned into Mo^{6+} ions, and the carrier density according to the concentration of the itinerant t_{2g} Mo electrons would be reduced, resulting in the resistivity increasing with increasing doping level [14]. Instead, our observed results show that for the high-doping-level sample (*x*=0.20, 0.25, 0.30), the resistivity decreases with increasing doping level. Thirdly, there is no Fe-O-Fe or Mo-O-Mo interactions and the direct Fe-Fe or Mo-Mo interaction is also very unlikely because it has to take place over a large distance of $5.584 \overset{o}{A}$ [14]. As explained above, we conclude that in our samples there exist Fe^{3+} ions and $Fe^{3+\delta}$ ions. In such a case the ferromagnetic coupling of the Fe ions may be described as a sort of double exchange mechanism as proposed by Zener [17] and B. García-Landa [14] involving $Fe^{3+}-O-Mo-O-Fe^{3+\delta}$ charge transfer.

Recently, Asano *et al.* [6] have pointed out that the magnetotransport properties of Sr_2FeMoO_6 thin films may be due to mis-site disorder or to partial phase segregation. On the basis of our experimental data, we suggest that the interesting feature of the resistivity as a function of temperature for the high-doping-level samples may indeed be due to phase segregation. Our system consists of a mixture of semiconductor regions and ferromagnetic metallic domains, where the latter may be due to the double exchange interaction in $Fe^{3+}-O-Mo-O-Fe^{3+\delta}$. The semiconductor-to-metal transport property can be explained in terms of the competition between these two coexistent phases, similar to that found in (La, Pr, Ca)MnO₃ and $La_{1-x}Sr_xCoO_3$ [18, 19] whose CMR (colossal magnetoresistive) behavior can be explained by the percolation threshold model. M. Fäth *et al.* [20] has also observed the phase separation at temperatures below T_C in which inhomogeneous structures of metallic and insulating

areas coexist, and their sizes and structures in single crystals and in thin films of $La_{1-x}Ca_xMnO_3$(with x of about 0.30) are strongly field-dependent. Insulating areas are found to persist at temperatures far below T_C. It was suggested that the transition and associated magnetoresistance behavior should be viewed as a percolation of metallic ferromagnetic domains. As seen in Fig.5.3 (a) for low doping levels (x=0.10 and 0.15), the resistivity as a function of temperature exhibits semiconductor behavior. Their resistivity is larger than that of the undoped Sr_2FeMoO_6. The Cu substitution induces disorder and the ferromagnetic metallic phase, which is in agreement with our computation of site order of the respective samples in our XRD analysis. Under the above condition, the semiconductor phase is still dominant, and the disorder enhances scattering, leads to carrier localization, and raises the resistivity of the two samples. Therefore, the resistivity increases with increasing doping level. For the high doping levels with x=0.20, 0.25, and 0.30, the transport property changes from that of a semiconductor to that of a metal at a critical temperature. Increasing substitution of Cu^{2+} ions for Fe^{3+} ions leads to an increase in the $Fe^{3+\delta}$ ions, thereby enhancing the double-exchange (DE) interaction in $Fe^{3+}\text{-}O\text{-}Mo\text{-}O\text{-}Fe^{3+\delta}$. As is well-known, an increase in interactions of the form of Mn^{3+}-O-Mn^{4+} results in an increase of electrons hopping between the Mn sites, which induces the formation of the ferromagnetic metallic phase in LaCaMnO [17]. In the same way, the formation of the ferromagnetic metallic phase, as suggested here, is enhanced by the double-exchange (DE) interaction in $Fe^{3+}\text{-}O\text{-}Mo\text{-}O\text{-}Fe^{3+\delta}$. This suggestion can be confirmed from the trend of the ac susceptibility χ as a function of temperature as shown in Fig.5.5. It can be seen clearly that the Curie temperature (T_C) increases with increasing doping level, thus supporting the conclusion that the substitution of Cu^{2+} ions for Fe^{3+} ions leads to enhancement of the metallic phase and a corresponding suppression of the

semiconductor phase in all the samples.

The observed features in all samples can be explained on the basis of the competition between the metallic phase and the semiconductor phase. For high doping levels, the temperature dependence of resistivity shows semiconductor behavior at low temperatures which changes into metal behavior at temperatures higher than T_{SM}. This phenomenon can be attributed to the combination of conduction of the semiconducting and metallic phases. The volume of material in the metallic phase in the high-doping-level samples (x=0.20, 0.25, and 0.30) can exceed the percolation threshold, resulting in a transition between the semiconductor and the metal phases in high-doping-level samples. Since this transition was not observed in the low-doping-level samples (x=0.10, 0.15), there must exist a critical doping threshold, x_C, such that for $x>x_C$ the percolation threshold occurs, while no percolation threshold takes place for $x<x_C$. From our results, x_C must lie somewhere between 0.15 and 0.20. From Fig.5.3, T_{SM} decreases with applied magnetic field (H=4 kG) or with increasing doping level because both factors contribute towards enhancing the effective volume of the ferromagnetic and metallic phase. Both factors also enhance the $Fe^{3+}-O-Mo-O-Fe^{3+\delta}$ ferromagnetic double exchange interaction, resulting in an increase of the ferromagnetic metallic phase.

The magnetoresistance observed in our samples can also be understood from the basis of the percolation threshold model. As show in Fig.5.4, the value of the magnetoresistance decreases with increasing doping level. On the one hand, the occurrence of $Fe^{3+\delta}$ reduces the degree of spin polarization of Fermi-level electrons of these samples, resulting in the reduction of the spin-polarized intergrain tunneling magnetoresistance (IMR). On the other hand, the increase in magnetoresistance with reducing Cu doping could be attributed to a relative increase in volume in the

semiconductor phase. The greater the volume of material in the semiconductor phase the poorer would be the connection among the FM domains, and so the degree of this magnetization misalignment should increase [18]. The magnetic field of 4 kG applied here is high enough to orientate the ferromagnetic metallic domains [21] and produce a larger magnetoresistance, since the large low-field magnetoresistance over a wide temperature range is induced by weak-link grain boundaries [22]. The small magnetoresistance in the sample with x=0.30 of only about 1% is attributed to the increase in the volume of ferromagnetic metallic phase with increasing doping level.

Although the above scenario seems plausible, there remain some problems yet to be explained. First of all, the occurrence of phase segregation must be clarified. The double exchange in the $Fe^{3+}-O-Mo-O-Fe^{3+\delta}$ and the possibility of $Fe^{3+\delta}$ in the system also needs to be further clarified by experiment. Further investigation is being made at present.

5.4. Conclusion

We have investigated carefully the electrical, magnetic, and transport properties of Cu-doped polycrystalline samples of $Sr_2Fe_{1-x}Cu_xMoO_6$ with ordered double perovskite structure. Analysis of the X-ray powder diffraction pattern in terms of the Rietveld analysis indicates that the substitution of Fe^{3+} ions by Cu^{2+} ions enhances the location order of Fe, Cu and Mo on the B-site for the high-doping-level samples (x=0.20, 0.25, 0.30). With increasing doping level, the transition from semiconductor to metal behavior occurs. Furthermore, the transition temperature can be decreased either by the application of a magnetic field or by increasing the doping level. It can be concluded that the existence of Cu^{2+} ions induces the occurrence of $Fe^{3+\delta}$ ions and the double exchange (DE) interaction in $Fe^{3+}-O-Mo-O-Fe^{3+\delta}$. On the basis of the percolation

threshold model, the transport mechanism in these samples can be attributed to the competition between the metal phase and the semiconductor phase as the doping level of Cu^{2+} ions changes.

References:

[1].   M. García-Hernández, J. L. Martínez-Lope, M. T. Casais, and J. A. Alonso, *Phys. Rev. Lett.* **86**, 2443 (2001).

[2].   J. Navarro, L. I. Balcells, F. Sandiumenge, M. Bibes, A. Roig, B. Martínez, and J. Fontcuberta, *J. Phys.: Condens. Matter* **13**, 8481 (2001).

[3].   K. -I. Kobayashi, T. Kimura, H. Sawada, K. Terakura, and Y. Tokura, *Nature (London)* **395**, 667 (1998).

[4].   H. Q. Yin, J. -S. Zhou, J. -P. Zhou, R. Dass, J. T. McDevitt, John B. Goodenough, *Appl. Phys. Lett.* **75**, 2812 (1999).

[5].   T. H. Kim, M. Uehara, S. -W. Cheong, and S. Lee, *Appl. Phys. Lett.* **74**, 1737 (1999).

[6].   H. Asano, S. B. Ogale, J. Garrison, A. Orozco, Y. H. Li, E. Li, V. Smolyaninova, C. Galley, M. Downes, M. Rajeswari, R. Ramesh, and T. Venkatesah, *Appl. Phys. Lett.* **74**, 3696 (1999).

[7].   Takashi Manako, Makoto Lzumi, Yoshinori Konishi, Kei-Ichiro Kobayashi, Masashi Kawasaki, and Yoshinori Tokura, *Appl. Phys. Lett.* **74**, 2215 (1999).

[8].   Y. Tomioka, T. Okuda, Y. Okimoto, R. Kumai, and K. -I. Kobayashi, *Phys. Rev. B* **61**, 422 (2000).

[9].   C. L. Yuan, S. G. Wang, W. H. Song, T. Yu, J. M. Dai, S. L. Ye, and Y. P. Sun, *Appl. Phys. Lett.* **75**, 3853 (1999).

[10].   H. P. Klug and L. P. Alexander, *X-ray Diffraction Procedures for Polycrystalline and Amorphous Materials*, 2nd ed, (Wiley, New York, 1974), P. 618

[11].   Abhijit S. Ogale, S. B. Ogale, R. Ramesh, and T. Venkatesan, *Appl. Phys. Lett.* **75**, 537 (1999)

[12]. Francis S. Galasso, Structure and Properties of Inorganic Solids, (Pergamon Press, Oxford, New York, Toronto, Sydney, Braunschweig, (1970) P. 171.

[13]. S. G. Wang, Y. P. Sun, W. H. Song, K. B. Li, and Y. H. Zhang, *J. Magn. Magn. Mater.* **223**, 238 (2001).

[14]. B. García-Landa, C. Ritter, M. R. Ibarra, J. Blasco, P. A. Algarabel, R. Mahendiran, and J. García, *Solid State Commu.* **110**, 435 (1999).

[15]. D. B. Wiles and R. A. Young, *J. Appl. Cryst.* **14**, 149 (1981).

[16]. R. von Helmolt, J. Wecker, B. Holzapfel, L. Schultz, and K. Samwer, *Phys. Rev. Lett.* **71**, 2331 (1993).

[17]. C. Zener, *Phys. Rev*, **82**, 403 (1951).

[18]. M. Uehara, S. Mori, C. H. Chen, and S.-W. Cheong, *Nature (London)* **399**, 560 (1999).

[19]. R. Caciuffo, D. Rinaldi, G. Barucca, J. Mira, J. Rivas, M. A. Señarís-Rodríguez, P. G. Radaelli, D. Fiorani, and J. B. Goodenough, *Phys. Rev. B* **59**,1068 (1999).

[20]. M. Fäth, S. Freisem, A. A. Menovsky, Y. Tomioka, J. Aarts, J. A. Mydosh. *Sicence* **285**, 540 (1999).

[21]. Y. Tomioka, A. Asamitsu, H. Kuwahara, Y. Moritomo, and Y. Tokura, *Phys Rev. B* **53**, 1689 (1996).

[22]. X. L. Wang, S. X. Dou, H. K. Liu, M. Lonescu, and B. Zeimetz, *Appl. Phys. Lett.* **73**, 396 (1998).

Chapter 6

The effects of Cu doping on the magnetoresistive behavior of perovskites La$_{0.7}$Ca$_{0.3}$MnO$_y$

In last chapter, we have investigated the electrical, magnetic, and transport properties of Cu-doped polycrystalline samples of Sr$_2$Fe$_{1-x}$Cu$_x$MoO$_6$ with ordered double perovskite structure. We found that the existence of Cu^{2+} ions induces the occurrence of $Fe^{3+\delta}$ ions and the double exchange (DE) interaction in Fe^{3+} - O - Mo - O - Fe$^{3+\delta}$. On the basis of the percolation threshold model, the transport mechanism in these samples can be attributed to the competition between the metal phase and the semiconductor phase as the doping level of Cu^{2+} ions changes. In order to enhance the present understanding on the electrical, magnetic, and transport mechanism of the double perovskite materials, for comparison, we also studied the electronic and magnetic properties of perovskite La$_{0.7}$Ca$_{0.3}$Mn$_{1-x}$Cu$_x$O$_y$ by doping with Cu on the Mn sites, since Mn^{3+}-O-Mn^{4+} network is crucial significance in an unusual interplay of transport and magnetism displayed by manganites [1-3].

In this chapter, the perovskite structure was found to remain intact up to the highest doping level of $x = 0.20$. At low Cu concentration (x=0.05) the temperature-dependence of resistivity of the material exhibited up to two peaks corresponding to the magnetic transitions from the PM to the FM phase, and from the FM to the AFM phase. In general, the doping level was found to suppress the ferromagnetic ordering of the material, increase its resistivity, and produce large values of MR

(magnetoresistance) near the resistivity peak. These results were explained as due to the formation of the AF (antiferromagnetic) phase.

6.1. Introduction

Early work on the structural, magnetic, and transport properties of perovskite manganite systems was carried out in the fifties [4-6]. The observation of colossal magnetoresistance (CMR) of these compounds in the form RE$_x$A$_{1-x}$MnO$_3$ (where RE=rare earth, A=Ca, Sr, Ba) [7-10] has spurred considerable interest in the study of these materials during the past few years. These and other sequential studies [1-3] had revealed the crucial significance of the Mn^{3+}-O-Mn^{4+} network in an unusual interplay of transport and magnetism displayed by these materials.

An interesting way to modify the Mn^{3+}-O-Mn^{4+} network is to dope at the Mn site itself [11]. Some such studies have been undertaken during the past few years [12-19]. Blasco *et al.* [12] studied the structural, magnetic, and transport properties of the La$_{2/3}$Ca$_{1/3}$Mn$_{1-x}$Al$_x$O$_{3-\delta}$ compounds, wherein the Al doping at the Mn site was shown to lower its Curie temperature T$_C$ and the metal-insulator transition temperature T$_p$. Both T$_C$ and T$_p$ decrease rapidly with Al concentration which does not affect the MR significantly. At higher *x* values, spontaneous loss of oxygen was found with a concurrent enhancement of MR. Several authors have studied the effects of Fe doping at the Mn site on the CMR properties of perovskites [13-19]. Righi *et al.* [13] examined a 5% Fe-doped La$_{0.7}$Ca$_{0.3}$MnO$_3$ compound and found a 50-K decrease in its T$_C$ and a 10–15% decrease in the average moment measured at 1 T. Gayathri *et al* [17] studied the properties of the La$_{0.7}$Ca$_{0.3}$Mn$_{1-x}$Co$_x$O$_3$ system for 0.05<*x*<0.5. They suggested that the substitution of Mn by Co dilutes the double exchange interaction and transforms the long-range ferromagnetic order to a cluster-glass-type FM order

[16].

In this chapter, we present the resistivity, magnetic and MR results of perovskite La$_{0.7}$Ca$_{0.3}$Mn$_{1-x}$Cu$_x$O$_y$ by doping Cu on the Mn sites at various doping levels. An increase in Cu concentration in this material decreased its ferromagnetic ordering, increased its resistivity, and produced large values of MR near the resistivity peak.

6.2.   Experimental

Bulk La$_{0.7}$Ca$_{0.3}$Mn$_{1-x}$Cu$_x$O$_y$ samples (with x = 0, 0.05, 0.1, 0.15, 0.2, respectively) were prepared by the conventional solid-state reaction processing in air. Stoichiometric proportions of La$_2$O$_3$, CaCO$_3$, MnCO$_3$ and CuO were mixed and ground, then fired at 1000°C for 24 h. After grounding, the resulting mixture was pelleted and sintered in air at 1200°C for 24 h and at 1250°C for another 24 h, with several intermediate grindings. Finally, the furnace was cooled down to room temperature naturally.

The crystal structure and the phase purity of the samples were examined by X-ray diffraction with the Cu K$_\alpha$ radiation. Magnetic measurements were carried out using a vibrating sample magnetometer. Resistance measurements were performed by the standard four-probe method. Electrical contacts were made with silver paste. The MR ratio here is defined as $MR = [\Delta\rho / \rho(0)] = [\rho(H) - \rho(0)] / \rho(0)$, where ρ_H and ρ_0 are the resistivities in an applied magnetic field (H = 8 kG) and at zero field, respectively.

6.3.   Results and Discussion

X-ray diffraction patterns for the series of La$_{0.7}$Ca$_{0.3}$Mn$_{1-x}$Cu$_x$O$_y$ (x = 0, 0.05, 0.1, 0.15, 0.2) are shown in Fig. 6.1, which shows single-phase orthorhombic distorted perovskite structure for all samples [20]. For the series of La$_{0.7}$Ca$_{0.3}$Mn$_{1-x}$Cu$_x$O$_y$, no

appreciable difference in the diffraction patterns has been observed among the Cu-doped samples.
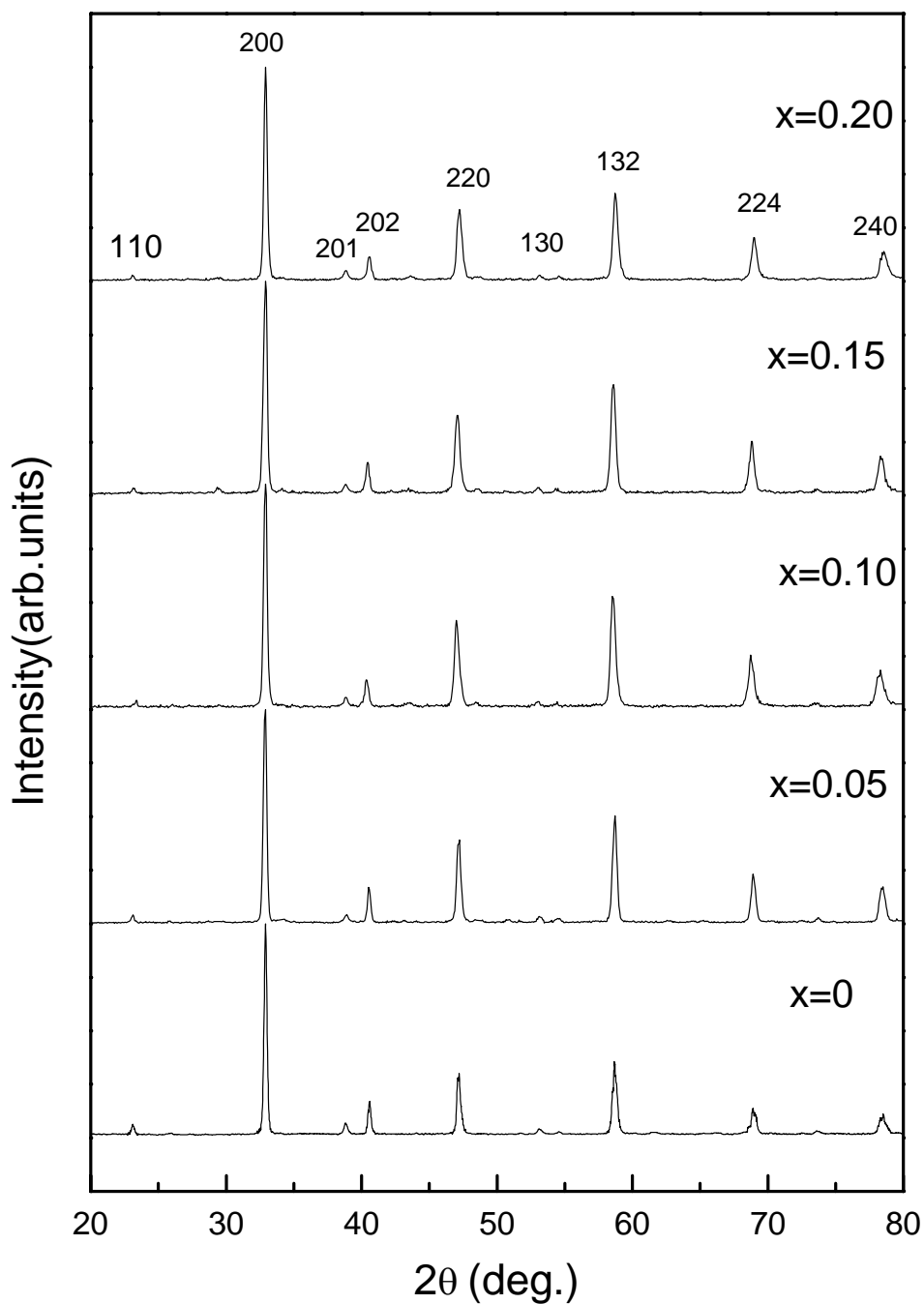
Fig.6.1. X-ray diffraction pattern of the polycrystalline La$_{0.7}$Ca$_{0.3}$Mn$_{1-x}$Cu$_x$O$_y$ samples with x =0, 0.05, 0.10, 0.15, 0.20 respectively.

Magnetic hysteresis loops with fields up to 3T have been measured at 77 K for all samples, as shown in Fig.6.2. The magnetizations are normalized to the value at 3T. The low-doping samples with $x=0$ and $x=0.05$ exhibit FM behavior, each with a clearly defined saturation magnetization and a square hysteresis loop. However, the results for the samples doped at the higher $x=0.10$ and $x=0.15$ levels do not exhibit saturation magnetization at high magnetic field. Their resultant magnetization curves appear to be essentially a superposition of both the FM and AF components, indicating a canted spin state, which is similar to those of La$_{0.63}$Ca$_{0.37}$Mn$_{1-y}$Fe$_y$O$_3$ [15]. When the sample doping level was further increased to $x=0.20$, the magnetization-dependent magnetic field becomes nearly linear. This indicates that only very little component of the material remains in the FM phase and most of it is in the AF phase.
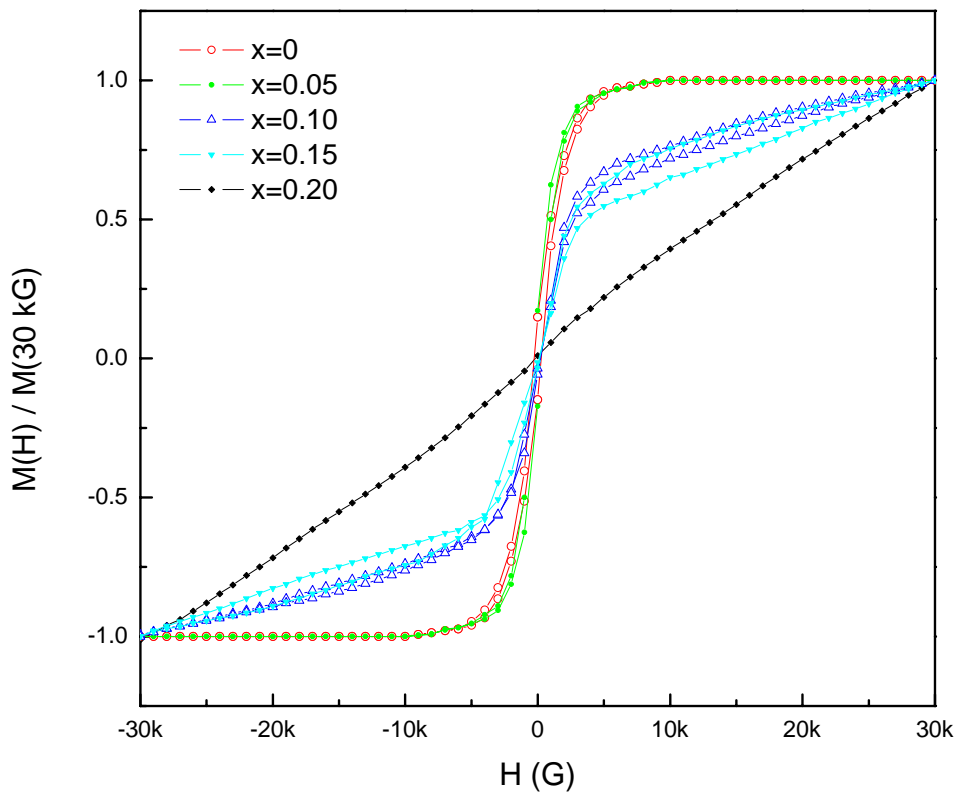
Fig.6.2. Magnetic hysteresis loops measured at 77K for the five La$_{0.7}$Ca$_{0.3}$Mn$_{1-x}$Cu$_x$O$_y$ samples. The magnetizations are normalized to the value at 3T.

The saturation magnetization of the FM component can be determined by extrapolating the linear part of the magnetization to H=0. These values displayed as saturation moment per formula unit are shown in Fig.6.3. We can see that the saturation magnetization decreases as the Cu-doping level increases. The saturation magnetization u$_s$ of the sample with *x*=0 is 3.78 μ_B. If we take only the spin magnetic moment into account, then this experimentally determined value is very close to the theoretical value. With the Cu-doping level increased to 0.20, the determined value of u$_s$ decreases to almost zero. Clearly, the presence of Cu actually suppresses ferromagnetism, instead of enhancing it, and thus enhances AF order.
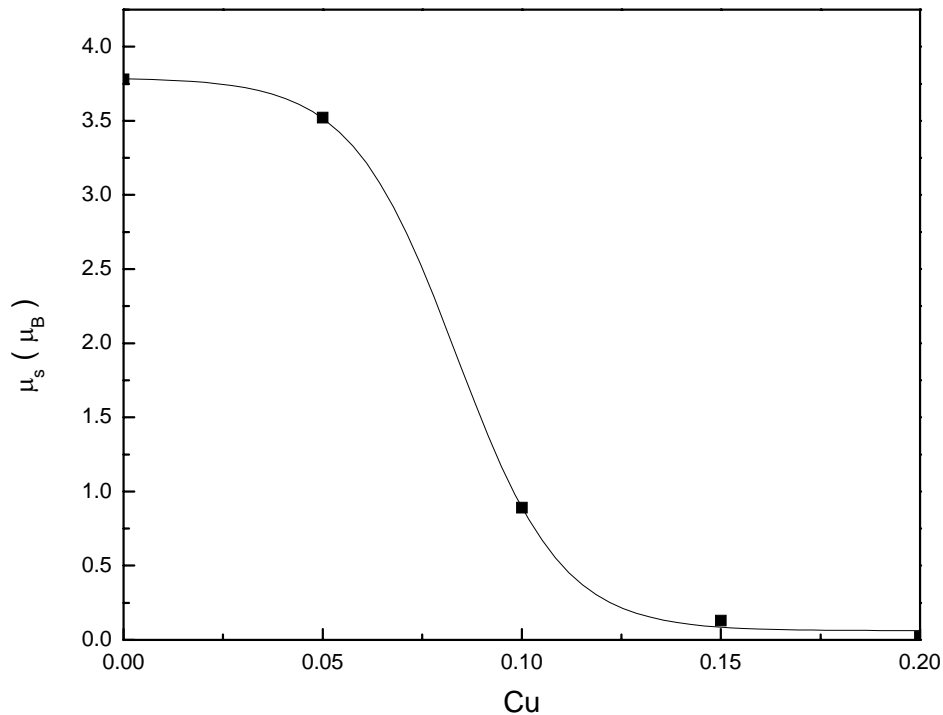
Fig.6.3. The corresponding saturation magnetization of the samples as a function of the concentration of Cu.

Fig.6.4 shows the temperature dependence of the dc magnetization for all samples. The magnetization was measured in the warming run with a field of 500 G after cooling down to 4.2 K in zero fields. The magnetic transition temperature T$_C$ is defined as the temperature at the maximum slope $\left|dM \middle/ dT\right|_{max}$ on the M-T curve. From Fig.6.4, we can see that there is only one magnetic transition temperature T$_C$=265K for the undoped sample (*x*=0). However, for the sample with *x*=0.05, there are two magnetic transition temperatures (T$_{C1}$=225 K and T$_{C2}$=180 K). The higher magnetic transition temperature, T$_{C1}$, corresponds to the transition from the PM phase to the FM phase, and the lower T$_{C2}$ corresponds to the transition from the FM phase to the AFM phase. For the samples with *x*=0.10 and 0.15 respectively, the canted spin state is known to exist. Therefore, for each sample, the higher magnetic transition temperature T$_{C1}$ (220K, 205K respectively) corresponds to the transition from the PM phase to the canted ferromagnetic phase, and the lower T$_{C2}$ (105 K, 95 K respectively) corresponds to the transition from the canted ferromagnetic phase to the AFM phase. When *x* is increased to 0.2, the curve for the zero-field cooled (ZFC) condition is quite different from that for the field-cooled (FC) condition. These two curves begin to separate and show the spin glass state when the sample temperature is taken below 35 K. This may be explained by the substantial substitution of Mn by Cu which enhances the exchange antiferromagnetism and weakens the double exchange ferromagnetism, thus causing a strong competition between these opposing phenomena. When the exchange antiferromagnetism balances the double exchange ferromagnetism at a certain temperature, the resultant short-range spin glass state will be exhibited.
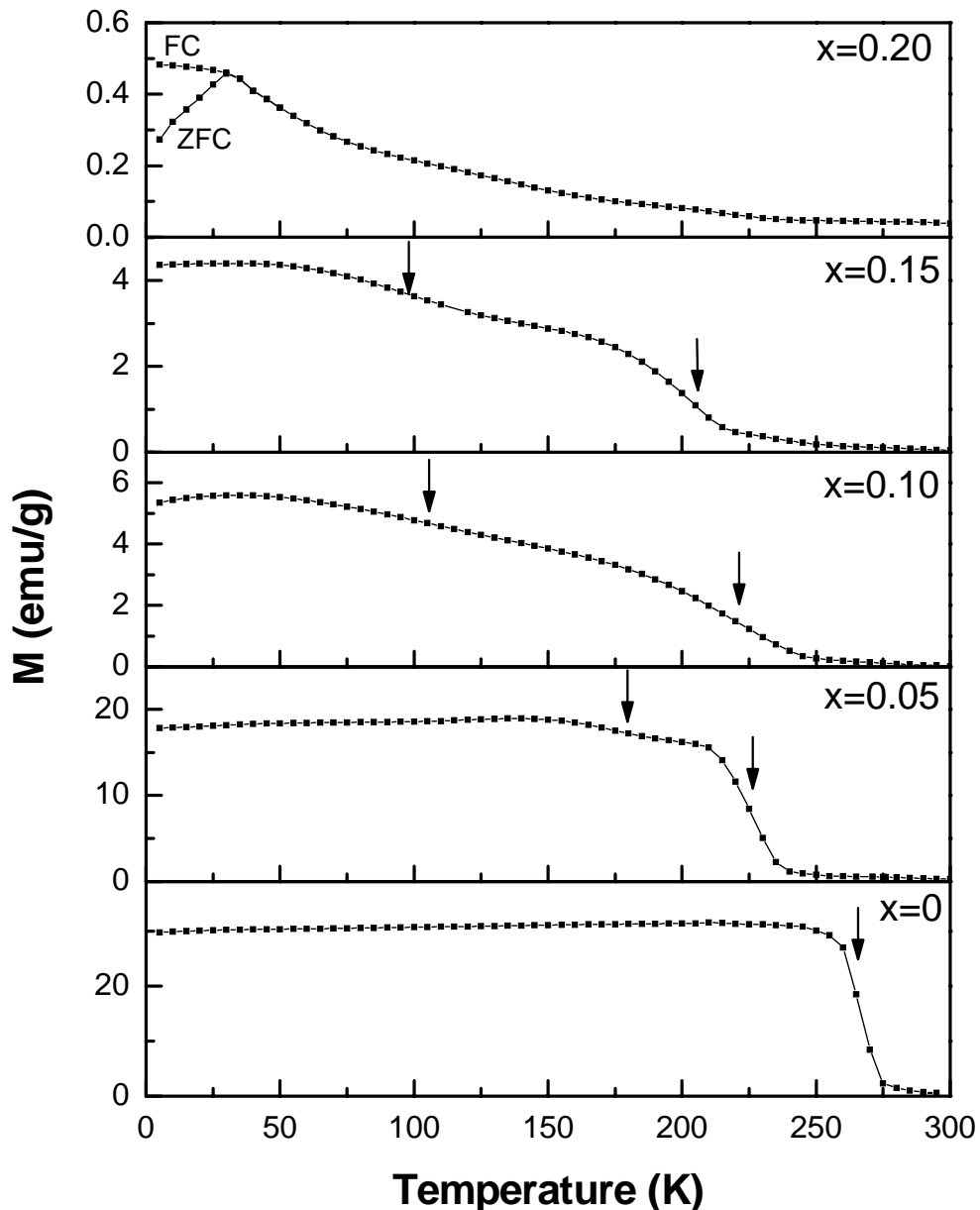
Fig.6.4. The temperature dependence of the dc magnetization, M, for the five La$_{0.7}$Ca$_{0.3}$Mn$_{1-x}$Cu$_x$O$_y$ samples. The magnetization was measured in the warming run with a field of 500 G after cooling down to 4.2 K in zero fields.

Fig.6.5 shows the temperature dependence of the resisivity at zero magnetic field and at 8 kG and the temperature dependence of the magnetoresistance (MR) ratio $\Delta\rho / \rho_H \times 100\% (\Delta\rho = \rho_0 - \rho_H)$ at 8 kG for the five samples of La$_{0.7}$Ca$_{0.3}$Mn$_{1-x}$Cu$_x$O$_y$ with x = 0, 0.05, 0.1, 0.15, 0.2, respectively. From the results, we can see that both the

resistivity and the MR of the sample are strongly dependent on its Cu-doping level, x. The maximum value of MR was obtained when x=0.10 for which it peaked at T=93 K. The resistivity curves at zero field and at 8 kG follow a similar trend, but with the zero-field resistivity always greater than that at 8 kG. At zero doping level, the resistivity exhibits a peak at a fairly high temperature. At x=0.05, two resistivity peaks were observed, which revert back to a single peak when x=0.10 or 0.15. As the doping level x increases from zero, the resistivity peak shifts towards lower temperatures until it disappears altogether when the sample doping level is raised to x=0.20. Compared with the magnetic results above, some more detailed features are established as follow:

1. For the sample with x=0 (La$_{0.7}$Ca$_{0.3}$MnO$_y$), the resistance increases as the temperature decreases from room temperature, and reaches a maximum at T$_P$=263 K which is close to the magnetic transition temperatures T$_C$. At T below T$_P$ the resistance decreases as the temperature further decreases.

2. At doping level x=0.05, the two resistivity peaks suggest the existence of two semiconductor-metal transitions at T$_{p1}$=226K and T$_{p2}$=180K respectively, which correspond to the two magnetic transitions from the PM phase to the FM phase at T$_{C1}$, and from the FM phase to the AFM at T$_{C2}$.

3. For the samples with x=0.10 and x=0.15, although there are two magnetic transitions, as shown in Fig.6.3, the temperature dependence of resistivity shows only one peak appearing at about 98 K and 99 K respectively, above which the samples display semiconductor behavior. A similar result was also found in La$_{0.5}$Ca$_{0.3}$MnO$_3$ [21]. In samples with high Cu contents, canted spin state exists, and the canting angle θ_{FM} is very large in zero field or in low magnetic field (8 kG) near T$_{C1}$. As a consequence, a charge transfer reaction

between neighboring sites is difficult, since, according to the double exchange model [22-24], charge transfer integral t is proportional to $\cos(\theta/2)$. At the temperature region near T$_{C1}$, charges are almost fully localized, which leads a thermally activated $\rho(T)$.

4. With the sample doping level increased to x=0.20, the antiferromagnetic super-exchange interaction prevails over the ferromagnetic double exchange interaction for the whole temperature range, so the sample shows the characteristics of an insulator.

5. With increasing doping level, the resistivity of the samples gradually increases. This is because the replacement of Mn^{3+} by Cu^{2+} causes a depletion of the Mn^{3+}/Mn^{4+} ratio, the population of the hopping electrons, and the number of available hopping sites. Thus double exchange is suppressed, resulting in the reduction of ferromagnetism and metallic conduction.

6. It is observed that Cu doping at x=0.10 causes a substantial enhancement in magnetoresistance, with a maximum MR at 1.823×10^4%. Compared with the undoped sample with x=0, the magnetoresistance of the x=0.10 sample was enhanced by about 230 times. Similar effects caused by doping at the Mn site were also previously observed in La$_{2/3}$Ca$_{1/3}$Mn$_{1-x}$Al$_x$O$_3$ [25] and La$_{2/3}$Ca$_{1/3}$Mn$_{1-y}$Fe$_y$O$_3$ [15], and were usually understood to be a result of the reduced DE interaction. When the Cu doping level increases to x=0.20, the magnetoresistance effect disappears completely.

The above experimental results should provide us a clear direction on how to enhance the magnetoresistance of the perovskite samples studied by adjusting their Cu doping levels.
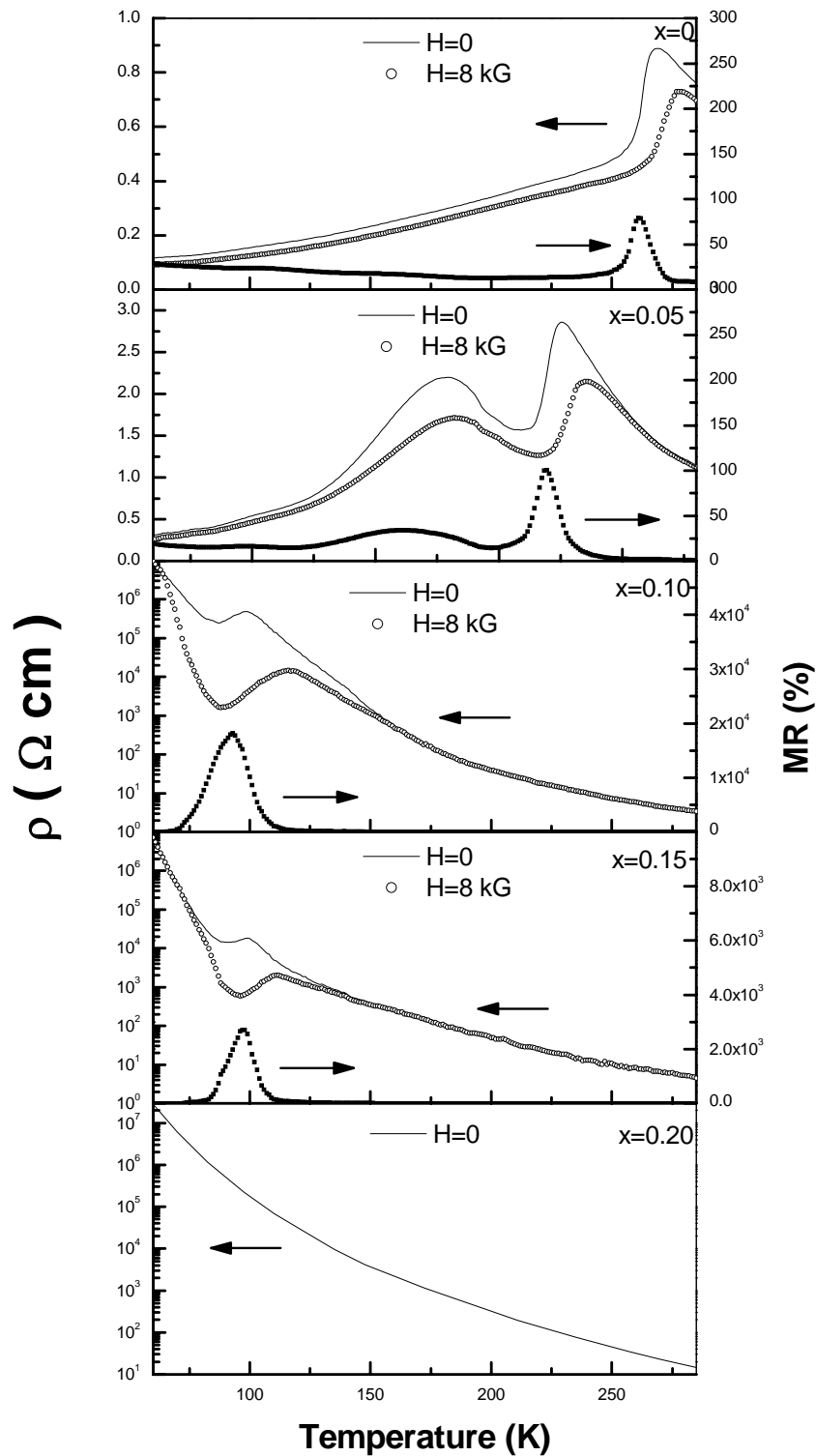
Fig.6.5. Temperature dependence of the resistivity for the five polycrystalline. La$_{0.7}$Ca$_{0.3}$Mn$_{1-x}$Cu$_x$O$_y$ samples in zero fields (solid line) and 8 kG (open circles), and of their magnetoresistance ratio $MR(\%) = (\rho_0 - \rho_H)/\rho_0 \times 100\%$ at 8 kG (solid squares).

6.4. Conclusions

In summary, we studied the electronic and magnetic properties of perovskite La$_{0.7}$Ca$_{0.3}$Mn$_{1-x}$Cu$_x$O$_y$ by doping with Cu on the Mn sites. An increase in Cu concentration in this material decreased its ferromagnetic ordering, increased its resistivity, and produced large values of MR near the resistivity peak. These results were explained as due to AF phase formation.

All of above discussion based on assumption that the Cu is in divalent state, which is the most common valence state observed for Cu ions, however, depending on the preparation condition, Cu ions could also be in trivalent state, this would also change the Mn^{3+}/Mn^{4+} ratio, thus our above conclusions still be applicable.

References:

[1]. V. A. Bokov, N. A. Grygoryan, M. F. Bryzhina, and V. V. Tikhonov, *Phys. Status Solidi* **28**, 835 (1968) and references therein.

[2]. Y. Shapira, S. Foner, N. F. Oliveira Jr., and T. B. Reed, *Phys. Rev. B* **10**, 4765 (1974).

[3]. R. M. Kusters, J. Singleton, D. A. Keen, R. McGreevy, and W. Hayes, *Physica B* **155**, 362 (1989).

[4]. G. H. Jonker and J. H. Van Santen, *Physica (Amsterdam)* **16**, 337 (1950).

[5]. C. Zener, *Phys. Rev.* **82**, 403 (1951).

[6]. J. B. Goodenough, *Phys. Rev.* **100**, 564 (1955).

[7]. K. Chahara, T. Ohno, M. Kasai, and Y. Kosono, *Appl. Phys. Lett.* **63**, 1990 (1993).

[8]. R. Von Helmolt, J. Weckerg, B. Holzapfel, L. Schultz, and K. Samwer, *Phys. Rev. Lett.* **71**, 2331 (1993).

[9]. S. Jin, T. H. Tiefel, M. McCromack, R. A. Fastnatch, R. Ramesh, and L. H. Chen, *Science* **264**, 413 (1994).

[10]. H. L. Ju, C. Kwon, Qi Li, R. L. Greene, and T. Venkatesan, *Appl. Phys. Lett.* **65**, 2108 (1994).

[11]. E. Banks and N. Tashima [*J. Appl. Phys.* **41**, 1186 (1970)] had studied Fe doping in LCMO in an entirely different context and had shown that the exchange between Fe^{3+} and Mn^{4+} ions is not strong

[12]. J. Blasco, J. Garcia, J. M. de Teresa, M. R. Ibarra, J. Perez, P. A. Algarabel, C. Marquina, and C. Ritter, *Phys. Rev. B* **55**, 8905 (1997).

[13]. L. Righi, P. Gorria, M. Insausti, J. Gutierrez, and J. M. Barandiaran, *J. Appl. Phys.* **81**, 5767 (1997).

[14]. M. Pissas, G. Kallias, E. Devlin, A. Simopolous, and D. Niarchos, *J. Appl. Phys.* **81**, 5770 (1997).

[15]. K. H. Ahn, X. W. Wu, K. Liu, and C. L. Chien, *Phys. Rev. B* **54**, 15299 (1996).

[16]. J. Cai, C. Wong, B. Shen, J. Zhao, and W. Zhan, *Appl. Phys. Lett.* **71**, 1727 (1997).

[17]. N. Gayathri, A. K. Raychaudhuri, S. K. Tiwary, R. Gundakaram, A. Arulraj, and C. N. R. Rao, *Phys. Rev. B* **56**, 1345 (1997). The differences between their data for the *x* = 0.05 Co doping case and ours can be attributed to the lower sintering temperature used by these authors (1100 °C) as compared to that used by us (1250 °C).

[18]. M. Rubinstein, D. J. Gillespie, J. E. Snyder, and T. M. Tritt, *Phys. Rev. B* **56**, 5412 (1997).

[19]. S. B. Ogale, R. Shreekala, Ravi Bathe, S. K. Date, S. I. Patil, B. Hannoyer, F. Petit, and G. Marest. *Phys. Rev. B* **57**, 7841 (1998)

[20]. P. N. Lisboa-Filho, A. W. Mombrú, H. Pardo, W. A. Ortiz, E. R. Leite, *J. Phys. and Chem. Solids.* **42**, 583 (2003)

[21]. G. Q. Gong, C. L. Canedy. Gang Xiao, J. Z. Sun, A. Gupta, W. J. Gallagher, *J. Appl. Phys.* **79**, 4538 (1996).

[22]. P. –G. de Gennes, *Phys. Ref.* **118**, 141 (1960).

[23]. C. Zener, *Phys. Rev.* **82**, 403 (1951).

[24]. P. W. Anderson and H. Haswgawa, *Phys. Rev.* **100**, 675 (1955).

[25]. G. Turilli, F. Licci, *Phys. Rev. B* **54**, 13052 (1996).

Chapter 7

Conclusions and suggestions for future work

7.1. Conclusions

This thesis has reported part of the contributions to the understanding of the MR effect in the double perovskites made at the Physics Department, National University of Singapore. These contributions are summarized below:

1. Grain boundary modification studies of Sr_2FeMoO_6 polycrystals are presented. The relationship between the magnetoresistance and the $SrMoO_4$ impurities are investigated, which improve the present understanding on the intergrain tunneling magnetoresistance of the double perovskite materials in physics and technology, especially at a relatively low magnetic field and room temperature. We studied the magnetic and electric properties of the Sr_2FeMoO_6 compound under different preparation conditions. Depending on preparation condition, we found a strong variation in nonmagnetic $SrMoO_4$ impurity, resulting in metallic or semiconducting behavior of resistivity of the sample. In particular, high-energy ball milling process suppresses the formation of the nonmagnetic $SrMoO_4$ impurity in the grain boundaries region. Also, the mixture ratio of the stream of gaseous H_2-Ar mixture strongly affects the eventual nonmagnetic $SrMoO_4$ impurity level in the annealed material. This $SrMoO_4$ impurity level, in turn, plays a crucial role in determining the low-magnetic-field intergrain

tunneling magnetoresistance. The presence of the impurity leads to an enhancement of the intergrain tunneling barrier, with a consequential increase in the resistivity and the low-field magnetoresistance. This property opens up the possibility of implementing refined control of the magnetotransport properties of high-temperature half-metallic ferromagnetic materials. Our works also provide a simple method to prepare the single phase Sr_2FeMoO_6 polycrystals.

2. A polycrystalline $Sr_2CoMoO_{6-\delta}$ film was fabricated on STO and the behavior of its resistivity at high temperatures, especially around T_C, has been investigated. The sample can be viewed as a typical mixed-phase system with ferromagnetic metallic clusters embedded in the AFM insulating matrix. With increasing temperature, its magnetoresistance decreases until the room temperature is reached. At higher temperatures, the sample resistivity exhibits a metal-insulator transition peak near T_C, which is attributed to the percolative transition between the FM metallic and AFM insulating phases. It provides the first experimental evidence that the phase separation scenario also exists in the transition-metal oxides with the ordered double-perovskite structure.

3. We have investigated carefully the electrical, magnetic, and transport properties of Cu-doped polycrystalline samples $Sr_2Fe_{1-x}Cu_xMoO_6$ with ordered double perovskite structure. Analysis of the X-ray powder diffraction

pattern in terms of the Rietveld analysis indicates that the substitution of Fe^{3+} ions by Cu^{2+} ions enhances the location order of Fe, Cu and Mo on the B-site for the high-doping-level samples (x=0.20, 0.25, 0.30). With increasing doping level, the transition from semiconductor to metal behavior occurs. Furthermore, the transition temperature can be decreased either by the application of a magnetic field or by increasing the doping level. It can be concluded that the existence of Cu^{2+} ions induces the occurrence of $Fe^{3+\delta}$ ions and the double exchange (DE) interaction in Fe^{3+} - O - Mo - O - $Fe^{3+\delta}$. On the basis of the percolation threshold model, the transport mechanism in these samples can be attributed to the competition between the metal phase and the semiconductor phase as the doping level of Cu^{2+} ions changes.

4. We studied the electronic and magnetic properties of perovskite $La_{0.7}Ca_{0.3}Mn_{1-x}Cu_xO_y$ by doping Cu on the Mn sites. The perovskite structure was found to remain intact up to the highest doping level of $x = 0.20$. At low Cu concentration (x=0.05) the temperature-dependence of resistivity of the material exhibited up to two peaks corresponding to the magnetic transitions from the PM to the FM phase, and from the FM to the AFM phase. In general, the doping level was found to suppress the ferromagnetic ordering of the material, increase its resistivity, and produce large values of MR (magnetoresistance) near the resistivity peak. These results were explained as due to the formation of the AF (antiferromagnetic) phase.

7.2. Suggestions for the future work

Future oxide materials development for spin-dependent transport will need to address a number of issues critical both for technological applications and for quantitative understanding of the physics of transport in half-metal junctions. First and foremost is the need to improve the temperature dependence of magnetoresistance for the different types of macroscopic interfaces. The large low-field MR values observed in magnetite oxide structures are very encouraging for practical applications. However, these large values are presently limited to low temperatures and the MR decreases rapidly with increasing temperature. Here, an investigation of Mo-based oxides with double-perovskite structure that has a T_C above 400 K and a seemingly robust interfacial magnetization might lead to a breakthrough. However, during the development of this thesis, many challenging problems remain because of the limitation of our facilities. Additional work with some enhancements of our facilities should lead to the discovery of more interesting physics.

1. In chapter 4, we investigated the temperature dependence of the resistivity and magnetoresistance of a polycrystalline $Sr_2CoMoO_{6-\delta}$ film deposited on (100)-$SrTiO_3$ substrate prepared by the pulsed laser deposition method. The temperature dependence of the resistivity of $Sr_2CoMoO_{6-\delta}$ was explained by the phase separation scenario. However, in order to make our evidence be more convincing, the magnetic characterization of our samples needs to be carried out at higher temperature, especially near Curie temperature.

2. In chapter 5, the electrical, magnetic, and transport properties of Cu-doped polycrystalline samples $Sr_2Fe_{1-x}Cu_xMoO_6$ with ordered double perovskite structure were investigated systematically. It can be concluded the existence of Cu^{2+} ions induces the occurrence of $Fe^{3+\delta}$ ions and the double exchange (DE) interaction in Fe^{3+} - O - Mo - O - $Fe^{3+\delta}$. On the basis of the percolation threshold model, the transport mechanism in these samples can be attributed to the competition between the metal phase and the semiconductor phase as the doping level of Cu^{2+} ions changes. However, there remain some problems yet to be explained. First of all, the occurrence of phase segregation must be clarified. The double exchange in the Fe^{3+} - O - Mo - O - $Fe^{3+\delta}$ and the possibility of $Fe^{3+\delta}$ in the system also need to be further clarified by experiment.